The impact of spatial subsurface heterogeneity on HT-ATES performance

A case study considering deltaic deposits

AESM7000: Master thesis

Robin Willingshofer 4952170

Delft University of T

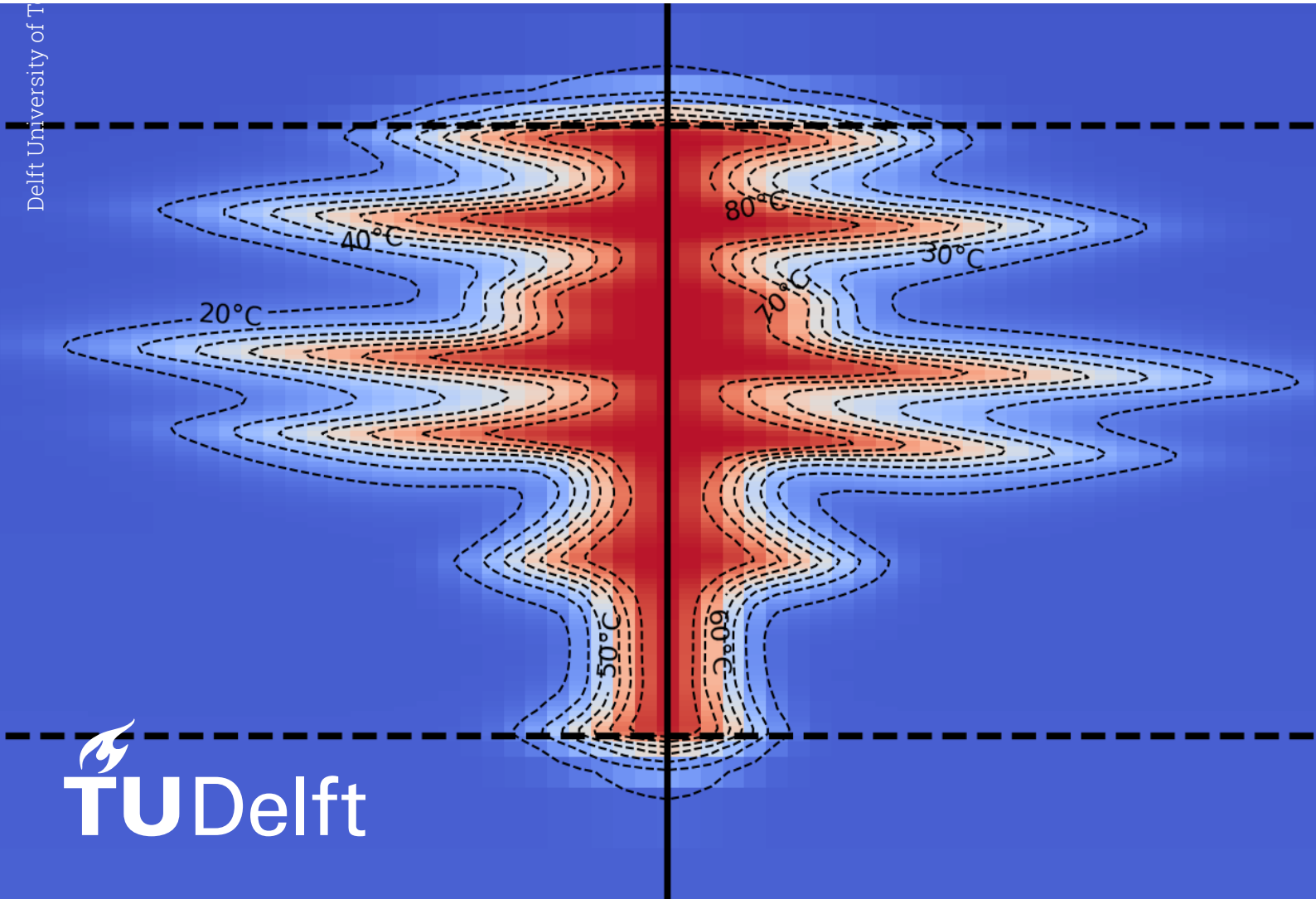

TU Delft

The impact of spatial subsurface heterogeneity on HT-ATES performance

A case study considering deltaic deposits

by

Robin Willingshofer 4952170

Supervisor:	Dr. Ir. Martin Bloemendal
Supervisor:	Dr. Alexandros Daniilidis
Committee member:	Dr. Hemmo Abels
Project Duration:	February, 2025 - September, 2025
Faculty:	Faculty of Civil Engineering and Geosciences

TU Delft

Abstract

High-Temperature Aquifer Thermal Energy Storage (HT-ATES) for short, is a technology that can help bridge the gap between energy supply and energy demand, which is particularly interesting to use in combination with renewable energy sources. The impact of subsurface heterogeneity on energy efficiency and thermal plume extent is not yet fully understood. In this paper, subsurface heterogeneity is linked to energy efficiency and thermal plume extent. A case study at the TU-Delft is considered, in which the Pleistocene deltaic deposits of the Maassluis formation have been characterized. Insights are gained from performing well correlations with high-resolution Gamma-Ray logs, which translates to an increase in understanding the possible architecture of the deposit and which adds a level of heterogeneity to current subsurface models that depict the Maassluis formation as a homogeneous medium. Stochastic and process-based geomodels have been constructed to represent the subsurface, using sequential indicator simulation with sequential Gaussian simulation and PyBarSimPseudo3D, respectively. Due to the difference in the underlying principles of the geomodeling techniques, the created geomodels show contrasting distributions in hydraulic properties. HT-ATES simulations have been performed with these heterogeneous geomodels using open-DARTS (Delft Advanced Research Terra Simulator). The results of the simulations show that heterogeneity has a negative impact on energy efficiency. The negative impact varies between 0.4 and 9.5 percent in the final cycle of simulation. The thermal plume distortion as a result of subsurface heterogeneity and potential for buoyancy flow to develop show to be the controlling mechanisms for the long term efficiency. The impact of heterogeneity also decreases over time as the thermal plume distortion is reduced as a result of conduction. The thermal plume extend, becomes highly unpredictable when aquifers have a low net-to-gross ratios. For stratified and high net-to-gross aquifers, the predictability is higher, as thermal plume is more circular.

Contents

Summary i

1 Introduction 1

2 Geologic features of the Maassluis Formation 4
2.1 Geological background . . . 4
2.2 Converting well data to lithology . . . 8
2.3 Lithology log correlations and interpretation . . . 10
2.3.1 Lithostratigraphic interpretation of well data . . . 10
2.3.2 Sequence stratigraphic interpretation . . . 11

3 Geomodeling 14
3.1 Stochastic geomodeling . . . 14
3.1.1 Sequential Inidicator Simulation . . . 14
3.1.2 Sequential Gaussian Simulation . . . 16
3.2 Forward Stratigraphic modeling . . . 19
3.2.1 Input data for PyBarSim . . . 19
3.2.2 PyBarSimPseudo3D output . . . 20
3.2.3 PyBarSim model postprocessing . . . 20
3.3 Thermal property modeling . . . 21
3.4 Geomodel analysis . . . 21
3.4.1 Quantative geomodel comparison . . . 22

4 HT-ATES simulation 25
4.1 DARTS . . . 25
4.2 Simulation set-up . . . 26
4.2.1 Operational parameters and System design . . . 26
4.2.2 Grid and spatial resolution . . . 27
4.2.3 Parameter space . . . 29
4.2.4 Homogeneous reference cases . . . 29

5 Interpretation of simulation data 31
5.1 Energy efficiency . . . 31
5.1.1 Homogeneous vs. heterogeneous simulations . . . 31
5.1.2 Parameter sensitivity . . . 39
5.2 Thermal plume analysis . . . 41
5.2.1 Controlling parameters on thermal plume spread . . . 43
5.2.2 Implication heterogeneity on HT-ATES spatial design . . . 43

6 Discussion 48
6.1 Geology . . . 48
6.2 Geomodeling . . . 49
6.2.1 Simulation set-up . . . 49
6.3 Simulation outcomes . . . 50

7 Conclusions 51

References 53

A Well data overview 56

B GR, SP and lithology logs 57

C Variography 81

D Derivation of operator form of mass and energy conservation equations 85

E Thermal plume density maps 87
E.1 Thermal plume maps for which T > 25 degrees Celsius 88
E.1.1 Stochastic geomodel plumes 88
E.1.2 RWK plumes 89
E.1.3 PBS plumes 90

1

Introduction

Currently, three-quarters of the energy consumed in the buildings sector is used for heating or cooling. This accounts for 22.5 percent of the total global energy demand (Bariloche, 2024). In 2021, 84 percent of this energy demand was met by non-renewable energy sources (Bariloche, 2024). Achieving net-zero goals requires significantly increasing the share of renewable energy in this sector. Aquifer Thermal Energy Storage (ATES) systems offer a promising solution to this aim. ATES systems store thermal energy for later use, by injecting relatively hot or cold water in underground aquifers. This allows renewable energy sources such as solar, wind, and geothermal to meet heating and cooling demands more effectively, as the temporal mismatch between the supply and demand of energy can be bridged via storage.

ATES systems are typically divided into low-temperature (LT) and high-temperature (HT) systems. LT-ATES systems use temperatures up to 25°Celsius, while HT-ATES operate at temperatures of 45°Celsius and higher (Bloemendal and Hartog, 2018).
The use of high temperatures in ATES systems has benefits, compared to low temperatures. First, low-temperature systems require a heat pump to be applied for (district) heating, where HT systems can be applied directly for heating purposes (Schout et al., 2014). By decreasing the contribution of heat pumps, the energy demand that is currently met by fossil fuels will decrease. In HT-ATES systems, excess renewable energy and industrial waste heat can be used, which increases overall energy efficiency (Sheldon, Wilkins, and Green, 2021). Lastly, the energy density is larger when higher temperatures are used. This reduces the amount of water necessary, to meet the energy demands of a location.
Despite the benefits mentioned, more than 3000 LT-ATES are operational, compared to the 1 HT-ATES system currently operating (Bloemendal and Hartog, 2018; Fleuchaus et al., 2020). The driver behind this difference is the range of complications that the higher storage temperature brings, which ranges from technical problems, economic uncertainty (Daniilidis et al., 2022), public perception issues, to difficulties in obtaining permits (Fleuchaus et al., 2020). For wide-scale deployment of HT-ATES systems, it is important that these complications are addressed appropriately.

A key metric used to determine the viability of (HT-) ATES projects is the energy efficiency, i.e. the thermal energy recovered relative to the total energy stored (Beernink et al., 2024; Gao et al., 2024). In addition to the scale and the temperature level of the HT-ATES systems, energy efficiency is influenced by the different ways that heat transfer mechanisms in the subsurface contribute to losses (Beernink et al., 2024).
Firstly, heat is transported through the aquitards by conduction, resulting in heat losses to the environment and reducing the amount of recoverable heat. Secondly, conduction within the aquifer transports heat away from the production well, making the thermal front less pronounced. Mechanical dispersion has a similar effect, smoothing the thermal front. Both processes lead to a reduction in the production temperature and consequently a reduction in energy efficiency. Lastly, free convection can cause thermal stratification (Sheldon, Wilkins, and Green, 2021), driven by the temperature dependence of the density of water. Warmer water expands, becomes less dense, and rises above cooler, denser water.

As a result, the ATES system produces colder water from the bottom of the aquifer sooner, influencing production temperatures.
The effect each mechanism has on energy efficiency depends on the thermal and hydrological properties of the subsurface (Beernink et al., 2024).

The relations between variations in HT-ATES model parameters (both subsurface and production parameters) on energy efficiency have been studied in the last decades for homogeneous cases (in e.g. (Heldt, B. Wang, et al., 2021; Collignon et al., 2020; Geerts et al., 2025)). This is done by performing numerical simulations. This led to a better understanding of how HT-ATES systems behave when the subsurface is homogeneous. Some of these studies went one step further by incorporating these relations into analytical expressions that estimate energy efficiency based on input parameters, without performing a full simulation (Schout et al., 2014; Sheldon, Wilkins, and Green, 2021; Gao et al., 2024; Geerts et al., 2025). That these analytical expressions exists only for homogeneous subsurface conditions highlights the limit of our current understanding of HT-ATES systems.

The subsurface is generally heterogeneous, which also applies to the aquifers targeted for HT-ATES systems. The heterogeneity is the result of the depositional processes in the environment in which the aquifer material is deposited. These processes control which facies will be deposited where, resulting in a spatial distribution of grain size, sorting, and layering of sediments. The spatial distribution of facies controls the distribution hydraulic properties, such as permeability and porosity. Paleoenvironments change over time as a result of geological and climatological processes. These changes may result in facies that occur laterally to be deposited on top of each other (Walther's Law of facies (Catuneanu, 2022)). This causes heterogeneity in the vertical direction (Catuneanu, 2022). The properties permeability and porosity can be altered by post-depositional processes, such as cementation, compaction, dissolution, karstification and fracturing (Possemiers, Leuven, et al., 2012; Chen, D. Voskov, and Daniilidis, 2025). Heterogeneity in hydraulic and thermal properties can enhance or obstruct groundwater flow and heat transport, affecting how much heat is lost (Y. Wang, D. Voskov, Daniilidis, et al., 2023). Therefore, the exact effect of heterogeneity on energy efficiency is difficult to estimate.

In most case studies for HT-ATES feasibility homogeneous subsurface properties are used in numerical simulations, which is an idealized representation of the subsurface. Here, key properties have been averaged over the modeled domain. By representing the subsurface in this way, the heat transfer mechanisms might not be modeled accurately, which can translate in predicted behavior that deviates from reality. Implementing heterogeneity in the simulations allows for conduction, dispersion and buoyancy flow to occur under more realistic conditions. By doing so, HT-ATES simulations will provide a more realistic view of the possible outcome of HT-ATES projects.

Besides, that the effect of a heterogeneous subsurface on heat transfer mechanisms is less understood, the distribution of subsurface parameters is uncertain and often have to be estimated based on limited data, being well data and seismic data. One of the main reasons why estimating is challenging and prone to errors, is the spatial variability in subsurface properties. This because the spatial variability in the subsurface can be highly heterogeneous, take as an example sandy channels and muddy floodplain deposits in a fluvial environment (Y. Wang, D. Voskov, Daniilidis, et al., 2023). A way of dealing with this uncertainty is by generating more realizations of the geomodels, that differ in permeability and porosity distribution, and using these realizations to obtain a range of plausible outcomes (Y. Wang, D. Voskov, Daniilidis, et al., 2023). Addressing the uncertainty in the subsurface helps quantify the uncertainty in recovery efficiency, which aids the decision-making process as well as design of implementing an HT-ATES design.

The inclusion of heterogeneity in HT-ATES systems has been limited to site-specific case studies so far. In many studies, the subsurface was simplified by approximating the reservoir structure by multiple vertically stacked homogeneous layers, which have different permissibilities. In doing so the lateral heterogeneity was disregarded (Winterleitner et al., 2018), (Heldt, Beyer, and Bauer, 2024) and (Tzoufka et al., 2024). However, in these studies, the aquifers considered were actually laterally heterogeneous, as indicated by well data or by knowledge of the existence of karst and fractures.
In the studies by Winterleitner et al. (2018) and Collignon et al. (2020), lateral heterogeneity was taken into account. Winterleitner et al. (2018) approached the heterogeneity due to the channels in the target reservoir by modeling them explicitly and using them in the simulation. It showed that the channels significantly influence the shape of the thermal plume and therefore the recovery efficiency. Collignon

et al. (2020) used spatially correlated noise in the porosity and permeability field in the geomodels, used in HT-ATES simulation. Here, it was observed that the inclusion of heterogeneity reduces the recovery efficiency.

Studies that systematically investigate the effect of subsurface heterogeneity on the performance of HT-ATES have not yet been conducted. However, the effect of lateral heterogeneity on LT-ATES systems was investigated in Sommer et al. (2013). Here, white noise and spatially correlated noise were considered. The results of Sommer et al. (2013) linked heterogeneity to an increase in the macrodispersion parameter. The study by Sommer et al. (2013) also showed that heterogeneity may reduce the energy efficiency by 6 to 15 percent. Although Sommer et al. (2013) used unrealistically large permeability values, namely in the range of 10 to the power of 3.2 m/day. Possemiers, Huysmans, and Batelaan (2015) incorporated clay drapes in deltaic deposits using multiple point statistics and performed LT-ATES simulations. This study found a reduction of 3.3 tot 3.6 percent in energy efficiency compared to the cases where clay drapes were absent. Because in both Sommer et al. (2013) and Possemiers, Huysmans, and Batelaan (2015) high temperatures are not considered, the exact effect of heterogeneity on HT-ATES performance remains unknown. Tang and Zee (2022) focused on the effect that a heterogeneous subsurface has on solute transport. As heat and solute transport share many similarities, the results can be translated to ATES systems. Tang and Zee (2022) found that correlated heterogeneity, created preferential fluid paths and reduced storage efficiency, compared to their predictions for homogeneous cases. Tang and Zee (2022) also related aquifer heterogeneity to the macrodisperion parameter.

In conclusion, studies on LT-ATES, solute transport and case studies show that heterogeneity may affect the efficiency. However, lateral heterogeneity has not been studied enough to provide qualitative nor quantitative statements about its effect on HT-ATES performance.

The aim of the thesis is to address this knowledge gap by answering the following central question:

What is the effect of subsurface heterogeneity on the performance of HT-ATES systems?

To answer this question, a case study of the TU-Delft is considered, as the results of this thesis might aid in estimating the behavior of the HT-ATES system that is planned for that location (Bloemendal, Phil Vardon, et al., 2020). This sets a scope to the research, and allows for local well data to be used. The main target for this system will be the Maassluis formation.

First, the characteristics of the Maassluis formation in the area of Delft are explored in chapter 2. In this part local well data and geological insight will be combined.

Based on the insights gained in chapter 2 geomodels will be constructed in chapter 3. Here, the goal is to implement the heterogeneous characteristics of the Maassluis formation the geomodels and to make multiple realizations of the subsurface.

In chapter 4 the simulation set-up and parameter ranges are discussed. With, the varied parameters being: the geomodel, the injection volume, injection temperature and the ratio of horizontal to vertical permeability. Based on this, simulations will be performed.

The simulation results of chapter 4 will be analyzed in chapter 5. Based on the analysis, differences between homogeneous and heterogeneous cases are illustrated. Furthermore, the parameter sensitivity in heterogeneous situations as well as the thermal plume extent are investigated.

2

Geologic features of the Maassluis Formation

This chapter is focused on characterizing the Maassluis formation in Delft. Here, the sedimentary characteristics of the deposits and the internal architecture of the reservoir are investigated. In doing so, the following subresearch question is answered: ”What are the characteristics of the Maassluis formation in the area of Delft?” The characteristics that are of particular interest are those that enable or block subsurface flow, since the results obtained in this chapter are translated into geomodels. Therefore, this chapter primarily focuses on finding the orientation and connectivity of low permeable clay layers in the domain of interest.

This chapter follows the work flow used to find the answers to the question above. First, a geological background is provided, based on the available literature on the Maassluis formation (section 2.1). Second, the data used and how they will be used will be elaborated on (section 2.2). Third, the geological background and local data are combined to interpret the Maassluis formation (section 2.3).

2.1. Geological background

The Maassluis formation (abbreviated as NUMS by the Dutch geological survey) is part of the Upper North Sea Group (abbreviated NU in Figure 2.1) (DINOloket, 2025). The Upper North Sea Group consists of a variety of deposits with various origins from the Miocene to the Holocene, as indicated in Figure 2.1 (DINOloket, 2025).

The Maassluis formation was deposited between 2.58 and 1.77 million years ago during the Early Pleistocene, more specifically during the Gelasian (a subdivision of the Early Pleistocene) (Jansen et al., 2004). During this time, the North Sea and the western part of the Netherlands were below sea level at the margin of the Southern North Sea basin (SNSB) (Kuhlmann et al., 2006).

Sediment is delivered from the Fenoscandinavian shield via the paleo Baltic river system, the Eridanos river, and deposited within a prograding delta in the SNSB (Jansen et al., 2004), (Veen et al., 2025) (Figure 2.2). During deposition, this delta prograded from east to north east to the west (Veen et al., 2025). Simultaneously, the Rhine-Meuse system delivered sediments from the south. However, during deposition of the Maassluis formation the role Rhine-Meuse system was small compared to that of the Baltic river system, as sedimentation rates from the Rhine-Meuse system to the Dutch sector of the SNS basin were relatively small (Veen et al., 2025). Subsidence could not keep up with the sedimentation rate, resulting in an infill of the SNSB and a shallowing upward trend in the Maassluis formation (Veen et al., 2025).

The exact onset of deposition of the Maassluis formation is uncertain, as the Maassluis formation represents a vertical an lateral continuation of the underlying and laterally existing Oosterhout formation (abbreviated as NUOO) (Jansen et al., 2004). The Oosterhout formation consists of similar deposits as the Maassluis formation, although the Oosterhout formation is deposited in deeper waters with open

marine conditions, which explains this gradual transition (Jansen et al., 2004). Due to this gradual transition, in Veen et al. (2025) the start is also denoted on the boundary of the Tiglean and Preatiglean at 2.42 Myr (Figure 2.1). In contrast to the deepening waters of the Oosterhout formation, the Maassluis formation is bounded by onshore fluvial deposits of the Peize and Waalre formation (abbreviated by NUPZ and NUWA, respectively) (Westerhoff, 2009). The Maassluis formation is eventually overlain by the laterally equivalent fluvial deposits of these formations, as the SNS became completely filled with sediment (Jansen et al., 2004).

The Oosterhout formation is distinguished from the Maassluis formation by glauconite content and the type of macrofossils (mollusks) present in the sediment (Jansen et al., 2004). Similarly to its separation from the Oosterhout formation, its upper boundary is determined by the upper most occurrence of marine shells Jansen et al., 2004.

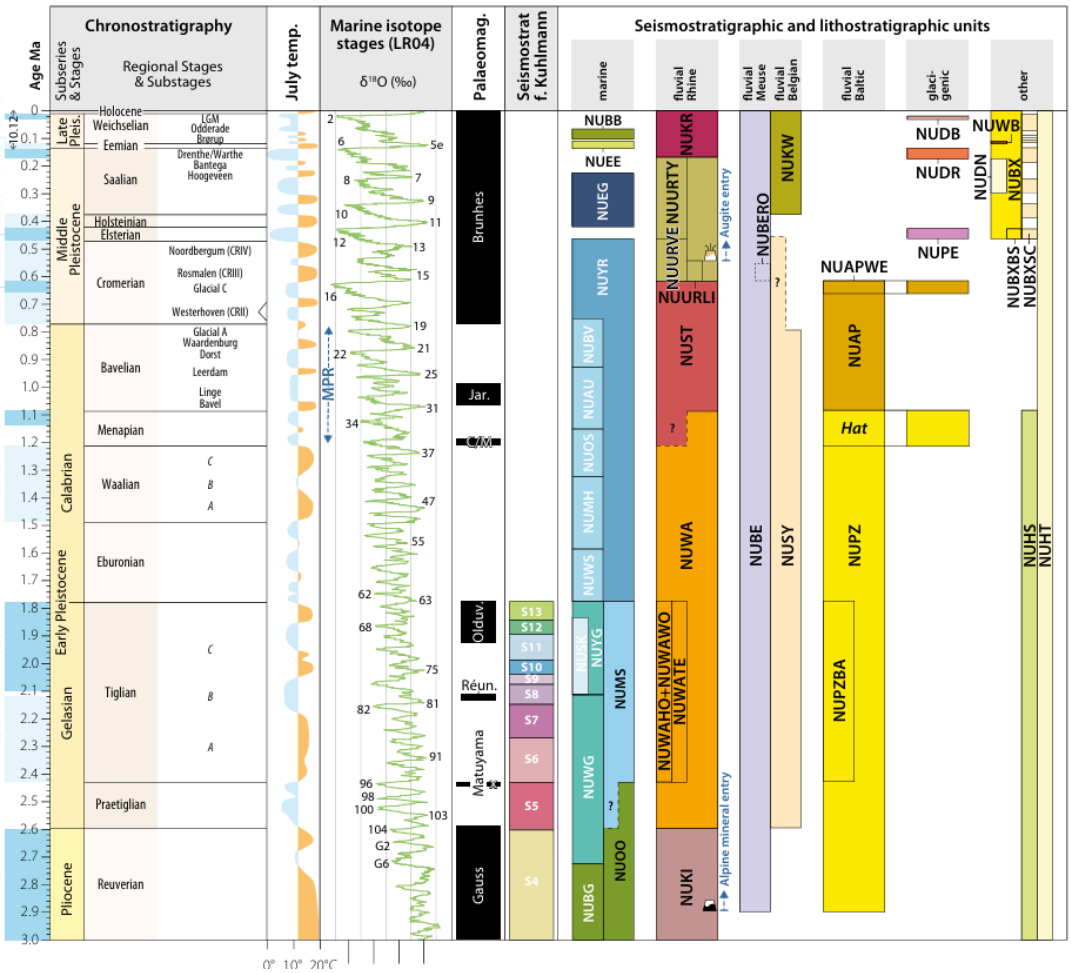

Figure 2.1: The timing and origin of formations in the Dutch subsurface. NUOO represents the Oosterhout formation, NUMS the Maassluis formation and NUPZ the Peize-Waalre formation. Source: (Veen et al., 2025).

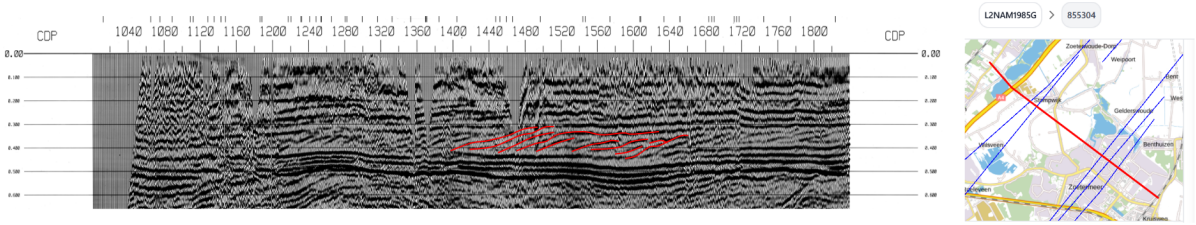

Figure 2.3: A seismic section, shot near Zoetermeer (South-Holland, the Netherlands). Some of the clinoforms have been interpreted in red, from (NLOG, 2025b).

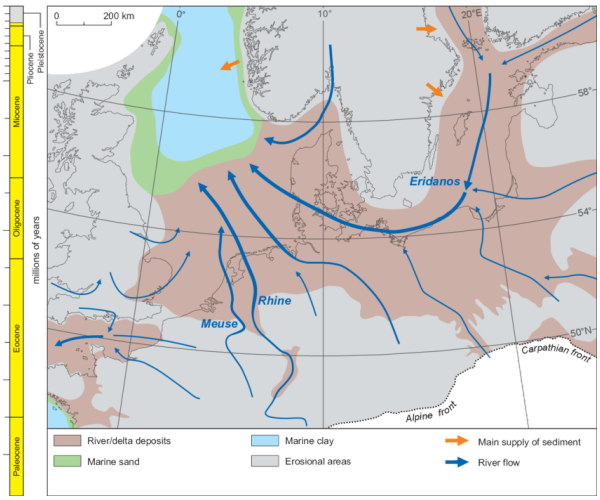

Figure 2.2: The reconstructed paleo-environment in the Early Pleistocene. The direction of major rivers that distribute sediment into the basin are depicted. The location of different deposit types are shown. Source: (Veen et al., 2025)

Deltaic deposits show variability in terms of grain size, based on the interplay of controlling mechanisms, such as sediment input, relative sea level rise and basinal process (wave, current and tidal) action (Patruno, Hampson, and Jackson, 2015). These processes affect the grain size distribution and, therefore, the morphology of deltas. Deltaic deposits have high variability perpendicular to the shoreline and low variability along the shoreline (Patruno, Hampson, and Jackson, 2015).

Clinoforms, associated with the progradation of a delta, are observed in seismic data of the subsurface (Figure 2.3) , which are further interpreted in (Jansen et al., 2004). In Jansen et al. (2004), two units within the Maassluis formation were distinguished. The lower unit consists of clay rich and sand rich intervals with a general coarsening-upward trend. The upper unit consists of coastal sand. This distinction is based on patterns in gamma ray and SP logs from the Noordwijk and Den Haag wells (Jansen et al., 2004).

The early Pleistocene is also the time period in which ice ages caused a fluctuating eustatic sea level, as glacial minima began to occur from roughly 2.6 to 2.4 Ma (Veen et al., 2025). In a recent study, the sea level of the past 3.6 Myr was reconstructed through 18-O isotopes records Berends, Boer, and Wal, 2021. Part of this reconstruction, containing the Early Pleistocene of this reconstruction is shown in (Figure 2.4). Note that the reconstruction is a plausible scenario, rather than a ground truth (Berends, Boer, and Wal, 2021). The figure indirectly shows the climate cyclicity with periods of 40 to 50 thousand years. A similar number of 41-kyr cyclicity is also discussed in Veen et al. (2025). This cyclicity is due to periodic changes in obliquity of the Earth (Catuneanu, 2022).

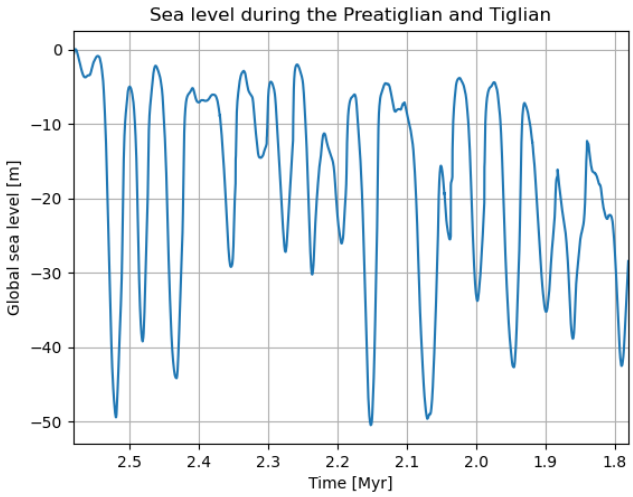

Figure 2.4: A reconstruction of the eustatic sea level as a function of time, modified from (Berends, Boer, and Wal, 2021).

The fluctuating sea level resulted in cyclic shifts of the paleo-shoreline and therefore deposited facies (Catuneanu, 2022). This effect as the water depth decreased due to sedimentary infill of the SNS basin. As a result, the internal architecture of the Maassluis formation is complicated, which will be discussed in section 2.3.

The spread and thickness of the Maassluis formation is governed by the location of the paleo-shoreline of the SNS basin and the initial topography of the Netherlands (Jansen et al., 2004). As the South North Sea basin covered a large part of the Netherlands, the Maassluis formation is present most of the country, although the thickness of the deposits decreases moving, landward (Houben et al., 2023), (Jansen et al., 2004) (Figure 2.5).

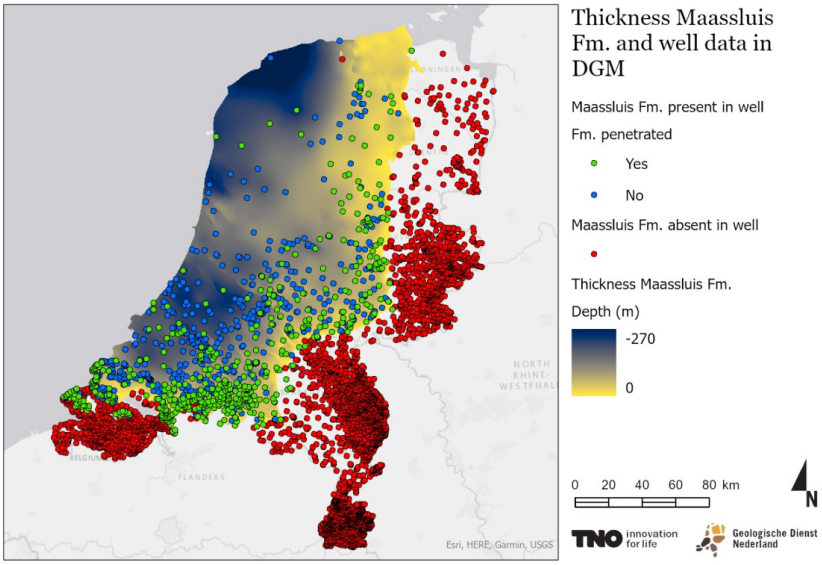

Figure 2.5: The occurrence and thickness of the Maassluis formation (from: (Houben et al., 2023)).

2.2. Converting well data to lithology

The integration of multiple data types is a key part in characterizing the subsurface. Geophysical data provide insight into the subsurface on various scales (Catuneanu, 2022). Well data provides high resolution data in the vertical direction, but has a poor spatial coverage. However, the high resolution is necessary to capture the heterogeneity. Therefore, this part of the research will focus primarily on well data.

One of the goals of the thesis is to create geomodels that are representative of the Maassluis formation in Delft, so it can be used in the case study. Therefore, well data will be used that are in the vicinity of the TU-Delft campus. An overview of the well data can be found in Appendix A. The well data are obtained from publicly accessible sources NLOG and DINOloket (NLOG, 2025a), (TNO Geologische Dienst Nederland, 2025). Here, the gamma ray (GR) logs are primarily used to characterize the subsurface. In case no GR log is available, the spontaneous potential (SP) log is used instead.

To construct GR-logs, a logging tool measures the natural radiation coming from radioactive materials in the earth along the borehole. The main contributors to the radioactivity of the subsurface are the isotopes of uranium (238U), thorium (232Th) and kalium (40K) (Pauw, Hernandez, and Doornenbal, 2022), which tend to concentrate in clay deposits, the GR-log can be used to distinguish clay from sand deposits (Pauw, Hernandez, and Doornenbal, 2022).

The SP log is obtained by passively measuring the potential difference in the subsurface between the 2 electrodes on the SP logging tool. As specific ions adhere to clay deposits, anomalies in the potential difference are observed when clay deposits are encountered (Pauw, Hernandez, and Doornenbal, 2022). Therefore, the SP tool can be used as an indicator for clay layers.

In combination with the lithological interpretations provided by DINOloket, the following lithologies are identified in the interval of interest: clay, fine sand, and medium to coarse sand sometimes shell bearing (TNO Geologische Dienst Nederland, 2025). In the perspective of subsurface flow, the heterogeneity with low permeability, the clay layers, is the most important to adequately model.

Based on a first visual inspection of the well logs, the following steps are carried out.

- If the logs are highly fluctuating (large fluctuations in GR or SP log signal that are smaller than 0.1m) in a way that relevant information is overshadowed, a moving average filter is applied. This smooths out these fluctuations, as the value of the GR or SP log at a given depth is averaged with n neighboring (in terms of depth) values. Here, n represents the window size, thus the number of data points over which the averaging takes place. The window size is manually determined, based on the quality of the log and the sample density.
- If the log shows an underlying change in signal that cannot be attributed to lithology, a correction is applied. The changes in signal are a sudden jump in the minimum logged value or a continuous increase of logged value over depth. These changes might be the result of different casings used, a change in well diameter from a specific depth, or the increase in formation water salinity. The correction is applied by subtracting a fitted polynomial from log.
- The log values are calibrated to lithologies based on the lithological interpretations available on DINOLoket. The goal is to correlate well-log signals with representative lithologies.
- Based on the calibration, the lithologies for all wells are interpreted and the resulting lithology logs are stored.

In total 24 well logs in the area of Delft, Rijswijk and Pijnacker have been analyzed and interpreted. The locations of these boreholes are shown in Figure 2.6. The resulting well logs after applying the steps above are shown in the appendix Appendix B.

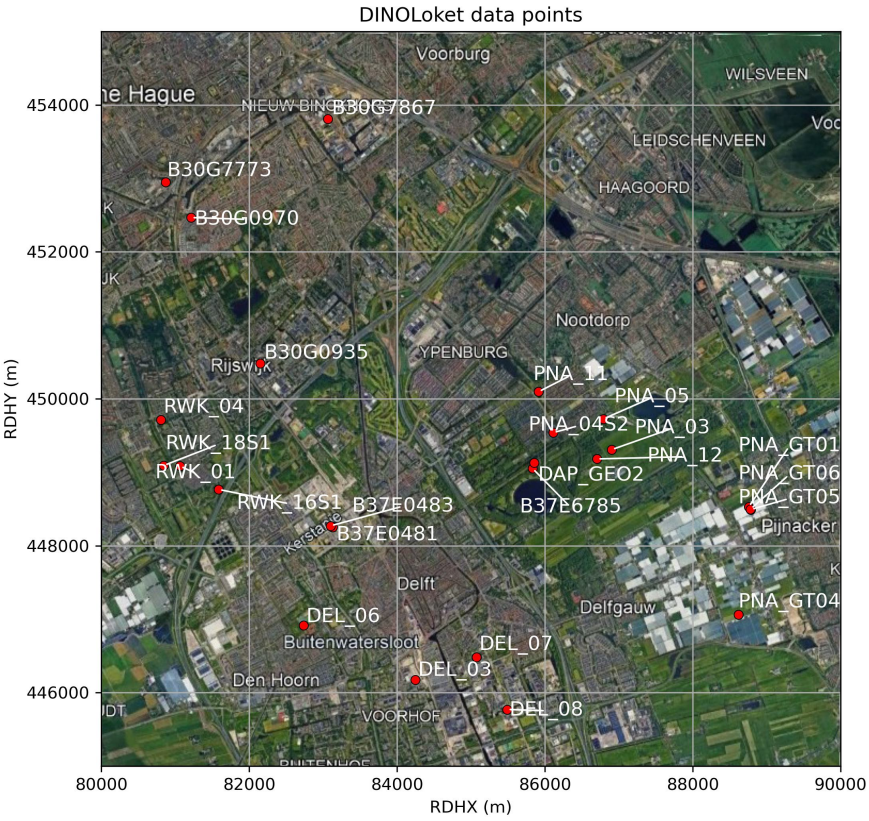

Figure 2.6: Location and names of the wells used in this study (dots in red). The well data can be found on (TNO Geologische Dienst Nederland, 2025) for wells that start with ”B”. All other well data can be found on (NLOG, 2025a). The back ground image is obtained from Google Earth.

2.3. Lithology log correlations and interpretation

In this section, insights from the literature are combined with the well data to create well log correlations. This because, although well logs provide high-resolution data, correlations must be performed to provide information about continuity of heterogeneity on the reservoir scale. This is especially true since well log signals can be ambiguous (Catuneanu, 2022). The ambiguity can be partially resolved by linking well data with inferences of depositional environments and associated processes. The way in which the well correlation will be performed depends on the type of depositional environment and may involve lithostratigraphic or sequence stratigraphic approaches, as outlined below.

The main reason why well correlations are performed in this study, is that the current geohydrological model of TNO has not enough complexity, as can be seen in Figure 2.7. From this model NUMsz3 can be interpreted as a homogeneous unit in terms of hydraulic properties. Though analysis in Jansen et al. (2004) and Slupik et al. (2007) indicate that these units are far less homogeneous than depicted here.

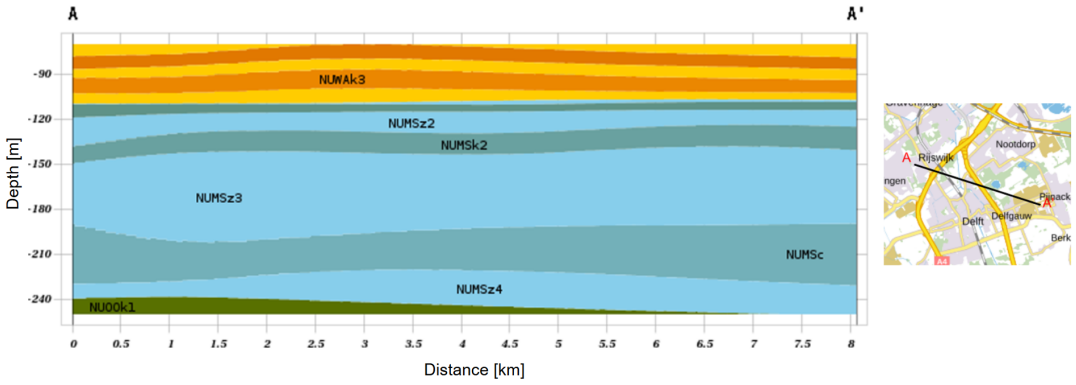

Figure 2.7: A cross section of the TNO BRO Regis II, the geohydrological model of the subsurface. Here, the blue interval is the Maassluis formation, the green interval (bottom left) the Oosterhout formation and the orange interval the Peize and Waalre formation.Main geohydrological units are identified within each formation, with z (ligth blue) indicating sandy units, k (dutch for clay, dark blue) the clayey units and c the complex units. The complex units are intercallations of smaller sand and clay units. From: (TNO – Geological Survey of the Netherlands, 2025)

In the following, two approaches to interpret the well data will be presented. First, a lithostratigraphic approach will be elaborated on. Second, a sequence stratigraphic approach is shown.

2.3.1. Lithostratigraphic interpretation of well data

To construct a lithostratigraphic correlation between wells, multiple wells that are roughly aligned in terms of X and Y coordinates are selected. This line runs from ENE to WSW. The interpreted lithologies per well are projected on this line, with appropriate distances. The lithology logs across the wells are correlated to each other. The NUMS-z3 unit will be the focus of this study. Therefore, the lithostratigraphic correlation will focus primarily on this interval.

The result of the correlation can be seen in Figure 2.8. When the clay intervals cannot be correlated, isolated wedges are drawn around these clay intervals. In Figure 2.8, clay intervals that span the entire 8 km are correlated.

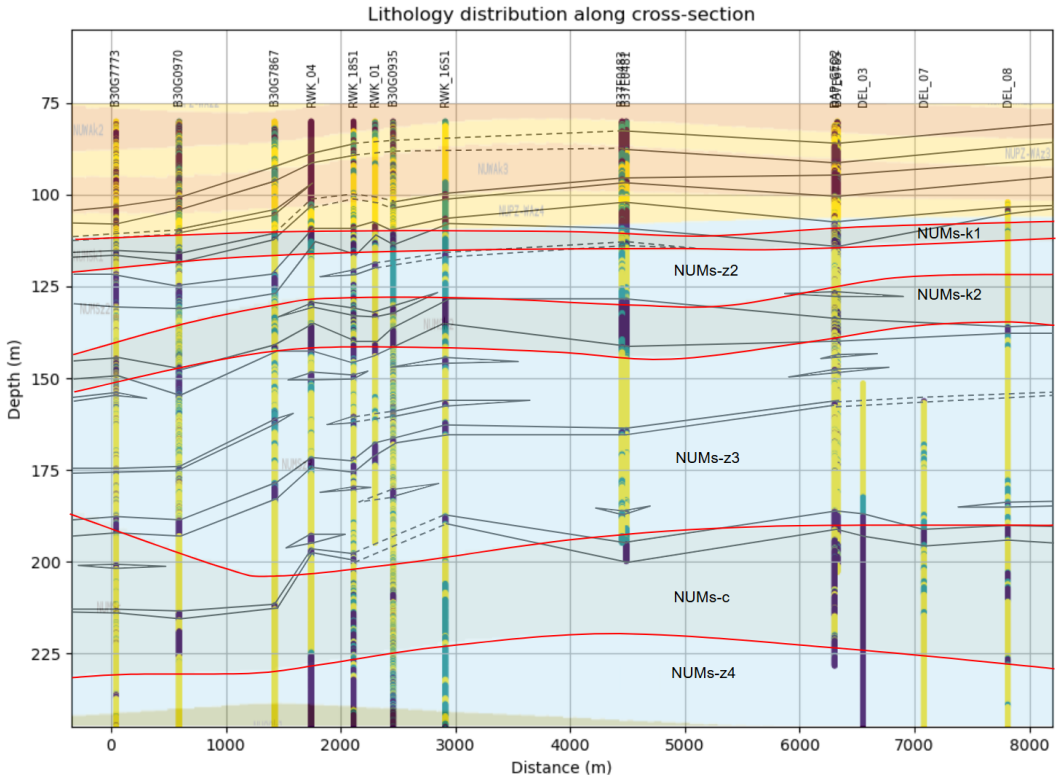

Figure 2.8: A lithostratigraphic correlation based on well data. The sand lithology, is shown in yellow, the mixed lithology in green, and the clay lithology in purple. The background of the figure shows the TNO geohydrologic model, depicted in Figure 2.7 from: (TNO – Geological Survey of the Netherlands, 2025). The Maassluis interval is the part of the model, that is shaded blue.

The lithostratigraphic correlation shows some similarities to the TNO subsurface model. Some of the major clay intervals (i.e. the intervals that span the entire domain) follow the model of TNO, reasonably. Take, for instance, the correlated clay interval at 135 meters depth, which follows the clay interval (NUMSk - 2 in Figure 2.7) depicted by TNO, though exact depth and thickness varies. Furthermore, the depths of the distinguishable units are within a considerable range to those of the TNO model. That the lithostratigraphic correlation and the TNO model share similarities is not completely unexpected. This because the BRO REGIS II model is constructed in a similar fashion, albeit with kriging between unit surfaces, obtained from borehole and seismic data (Veen et al., 2025).

However, differences can be observed between the height, thickness, and dip of the major intervals. A possible explanation for these differences could be:

- the manual interpretation of lithologies from the well data;
- how the clay layers are correlated in Figure 2.8;
- the 3D effect that comes into effect when transposing well data points to the correlation line.

In addition to differences in the large units, the interpretation shows many smaller clay intervals that are connected by only a few of the wells, which do not appear in the TNO model. This added level of detail illustrates the benefit of creating the lithostratigraphic correlation.

2.3.2. Sequence stratigraphic interpretation

Below, first a brief introduction to sequence stratigraphy is given. For a complete background on the matter, the book of Catuneanu (2022) can be reviewed.

In sequence stratigraphy bounding surfaces, surfaces that end a sequence, and their enclosing sequences are correlated across the well data. What is meant by sequence is a package of facies that is coherent and behaves in a predictable way (Catuneanu, 2022). To give an example, in a coarsening-

upward sequence the grain size within the sequence decreases with decreasing depth. When the coarsening-upward sequence transitions into a new, fining-upward sequence, the coarsening-upward sequence is ended. The depth at which the transition occurs, is in this case the bounding surface Catuneanu, 2022.

The correlation of sequences is done by interpreting the GR and SP log shapes. Usually, low GR and SP readings represent coarse grained material and vice versa (Catuneanu, 2022). This implies that GR and SP logs should be inverted to be representative for grain size.

The following rules have been identified for sequence stratigraphic correlations, which are adapted directly from (Catuneanu, 2022)

1. Prograding clinoforms slope seaward
2. Shallow marine regressive units tend to have continuity along the dip direction
3. Units tend to fine (in terms of grain size) and thin in the direction of the sea.
4. Thickness of units do not vary randomly
5. Strata may terminate landward by onlap, offlap, toplap or truncation
6. If there is no reasonable correlation possible, an unconformity might be inferred.

Four wells with clear GR signals in the domain of interest have been correlated following a sequence stratigraphic approach, with the above guidelines. The results, shown in Figure 2.9, illustrate west-dipping surfaces, consistent with the westward progradation of the Eridanos delta. The clay layers can be tracked along the surface boundaries, which show that they are continuous in the interpreted domain. The inclination of clay layers is in contrast to the TNO model (Figure 2.7), where clay intervals are drawn almost horizontally. Besides, the inclination of clay invervals, the amount of clay layers is higher in the sequence stratigraphic correlation. Similarly, to the lithostratigraphic approach, a level of complexity is added to the subsurface.

When compared to Figure 2.8 clear differences can be observed. For example, clay layers in Figure 2.8 compared to the inclined clay layers in Figure 2.9. This might introduce deviations in the expected flow behavior. Next to that, the lateral continuity of clay layers is much for most of the clay intervals than in the lithostraphic correlation. This continuity might affect vertical flow, significantly HT-ATES systems.

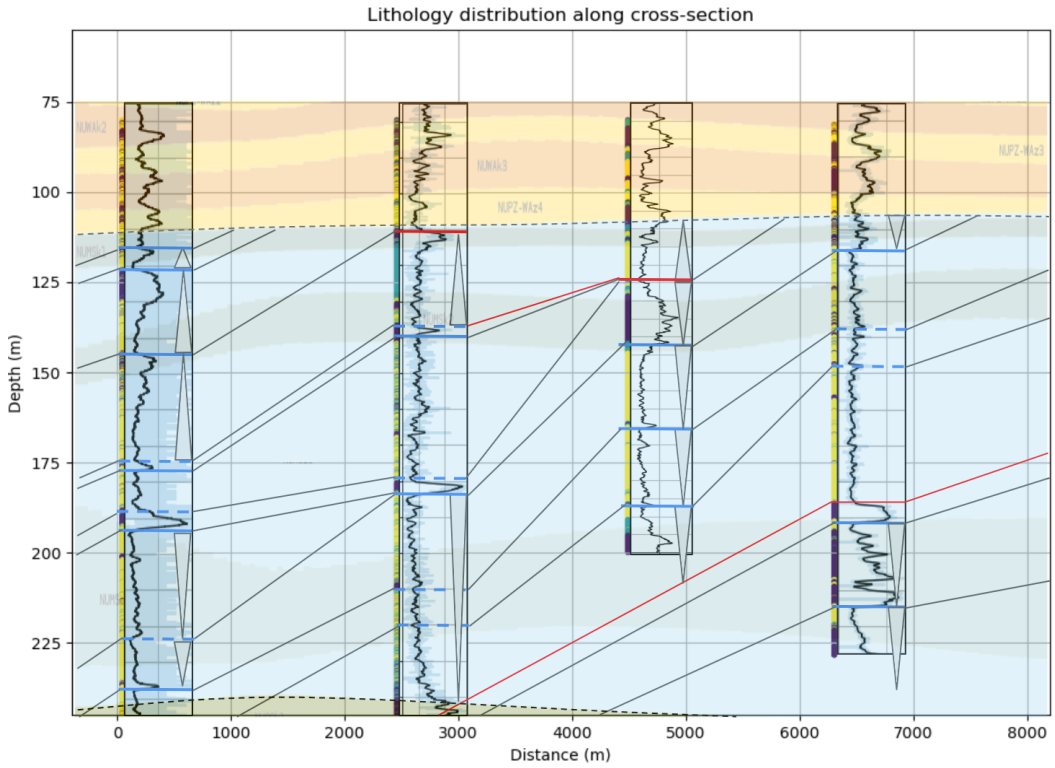

Figure 2.9: The sequence stratigraphic interpretation of 4 well logs. The triangles indicate either a fining upward sequence (triangle pointing up) or a coarsening upward sequence (triangle pointing down). sequence boundaries are denoted in blue. Inferred sequence boundaries and lower rank sequence boundaries are indicated by a dashed blue line. Erosive boundaries and erosive surfaces are drawn in with a red line. In the lithology logs, the sand lithology is shown in yellow, the mixed lithology in green, and the clay lithology in purple.

3

Geomodeling

The key question that will be addressed in this chapter is how to translate the observed heterogeneity, discussed in chapter 2, into geomodels that can be used for HT-ATES simulation. The obtained lithology logs and the lithological correlations created in chapter 2 serve as starting points for the creation of the geomodels. Numerous geomodeling techniques have been developed with distinct features. The tool that is most suitable depends on the type of deposit considered and its characteristics. Two geomodeling methods are selected to create the geomodels, namely stochastic and process-based geomodeling. This chapter will discuss both techniques and the associated workflows that are used to create the geomodels (section 3.1 and section 3.2). From the geomodels thermal properties are derived in section 3.3. Afterwards, the differences between the obtained model will be elaborated on in section 3.4.

3.1. Stochastic geomodeling

The first method considered, combines sequential indicator simulation (SIS) with sequential gaussian simulation (SGS) into one stochastic geomodel. The main procedure involves assigning categorized lithologies to all grid cells in the domain with SIS. Then, to each cell porosity and permeability values are assigned with SGS, depending on the lithology. The precise steps are elaborated on below. The GSLIB software is used for SIS and SGS Deutsch and Journel, 1997.

3.1.1. Sequential Inidicator Simulation

Sequential indicator simulation is used for discretized modeling of indicators, with indicators being distinct lithologies Deutsch and Journel, 1997. Here the lithologies from the well data, obtained in section 2.2, are assigned to categories. Category 1 is used for sand, category 2 for a mixture of fine sand and category 3 for clay. Categorical values are assigned for each grid cell based on Simple Kriging. For a complete description of the SIS algorithm, please review GSLIB (chapter V.3. page 143, Deutsch and Journel, 1997). SIS is executed with the sgsim module of the GSLIB software (Deutsch and Journel, 1997, chapter V.7.2 page 170).

Two well clusters are defined based on the X and Y coordinates of the well, with the goal of having as many wells as possible in a small area, to enhance the data density. The clusters are named the PNA (Pijnacker) and RWK (Rijswijk) cluster, with their names based on the name of the place the boreholes located at.

An initial grid with a cell spacing of 5 meters in the horizontal direction and 0.25 in the vertical direction is constructed around the wells. The horizontal extend of the grid is dependent on the X and Y coordinates of the wells. Then, the well lithology data is upscaled to this grid by the mode of the facies in the respective grid cell.

An experimental semivariogram is constructed, one for each lithology. The gamv tool of the GSLIB software is used to compute the experimental semivariogram ((Deutsch and Journel, 1997) III.2, page 47).

A variogram model is fitted to this data. The experimental semivariogram and the fitted model can be found in Appendix C for the PNA and RWK model.

From the wells in the cluster lithology proportions are computed. These serve as a reference distribution for the GSLIB sisism tool, which assigns lithologies to all grid cells (Deutsch and Journel, 1997).

The models obtained show the typical patch-like behavior in the lithology distribution, which is expected by the SIS algorithm (Figure 3.1a and Figure 3.1b). The localized patches of clay in a dominantly sandy body show some agreement with the lithostragraphic well correlation presented in chapter 2, Figure 2.8.

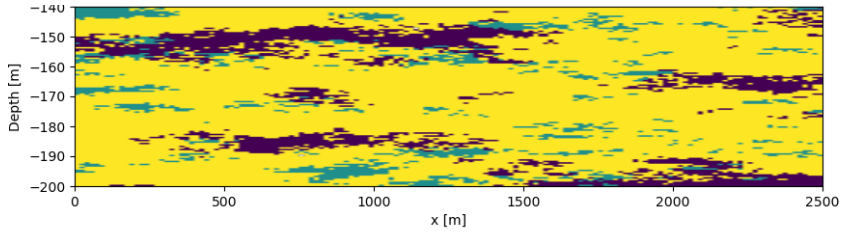

(a) A cross section of the lithology distribution for the PNA model, created with sisim. In the cross section, the sand lithology is shown in yellow, the mixed lithology in green, and the clay lithology in purple.

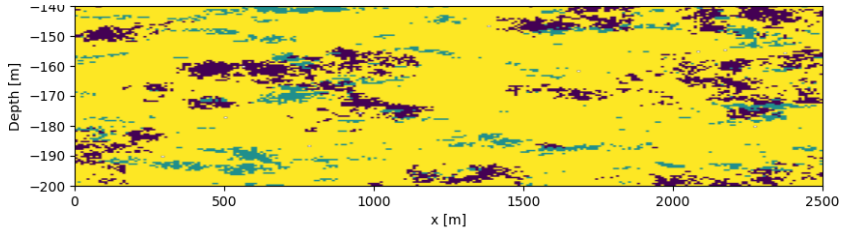

(b) A cross section of the lithology distribution for the RWK model, created with sisim. In the cross section, the sand lithology is shown in yellow, the mixed lithology in green, and the clay lithology in purple.

Figure 3.1: Comparison of lithology distributions in the PNA and RWK models.

As both the PNA and the RWK model have a unique set of input data, the output models have some differences. First, the proportions of each lithology vary, as can be seen in Table 3.1. It can be seen that the proportion of sand is higher in the RWK model, meaning that it is a more clean reservoir, compared to the PNA model. Note that these values contain the global proportions of the entire domain, which might cause local deviations when the model is cropped.

Second, the variogram models for all lithologies have different input parameters as can be seen in Table 3.2. In this table, Range max and Min represent the correlation length. From this table, it can be observed that PNA 3 and RWK 3, have a large difference in azimuth. That is, lithologies are not oriented in the same direction. Some differences in correlation lengths and azimuth can be explained by looking at the variograms in Appendix C. Especially for the Rijswijk model, the fitting of a variogram model to the data became more challenging.

From Table 3.1 it can be seen that the input data proportions (well proportions) and the output model proportions have a slight mismatch. In Deutsch and Journel (1997) this is discussed and is attributed mainly to the correlation length and the model length being in the same order of size. The proportions of the output model could be altered by selecting an alternative seed.

	Sand	Mixed	Clay
Wells PNA	0.69	0.11	0.20
Model PNA	0.71	0.10	0.19
Wells RWK	0.75	0.11	0.14
Model RWK	0.83	0.07	0.10

Table 3.1: The lithology proportions of the wells used for SIS and the respective lithology proportions of the entire modeled domain.

	PNA 1	RWK 1	PNA 2	RWK 2	PNA 3	RWK 3
Partial sill	0.9	0.7	1.0	0.9	0.9	0.9
Nugget	0.1	0.3	0.0	0.1	0.1	0.1
Range max (m)	750	350	500	2100	690	600
Range min (m)	550	250	180	700	520	320
Azimuth (deg)	20	-10	-20	160	67	0
Range vertical (m)	15	9	3	3	10	7

Table 3.2: The parameters for the semi-variogram model, obtained from fitting the experimental variogram. Note that azimuth represents the direction of range max in degrees deviating from the North. Range min is perpendicular to range max.

3.1.2. Sequential Gaussian Simulation

In Deutsch and Journel (1997) (chapter V.7.2, page 170) a detailed explanation of the Sequential Gaussian Simulation (SGS) procedure can be found. The most important difference between SIS and SGS is that SGS is used for continuous property modeling, such as porosity and permeability in this case (Deutsch and Journel, 1997).

Artificial porosity and permeability data need to be created, as that is a required input for SGS. To do so, artificial porosity data are created for each well. The porosity data is created first as it is assumed that porosity and permeability are correlated, meaning that the permeability values depend on porosity. The data is created by drawing five samples at evenly spaced depth intervals from the normal distribution shown in Figure 3.2. The data are obtained from core measurements on the Maassluis Formation in the North Sea, provided by NLOG (NLOG, 2025a). The vertical variogram, obtained in subsection 3.1.1, is used to obtain a continuous porosity distribution along each well, using the SGS algorithm in one dimension.

Second, artificial horizontal permeability data is created by assuming that a correlation exists between porosity and permeability. A bivariate normal distribution is used to create permeability data directly from the continuous porosity data. A correlation coefficient of 0.8 is assumed. The mean and standard deviations of the permeability data are obtained from the bimodal distribution of the NLOG core measurement data (Figure 3.3). Here, distribution 1, with its mean and standard deviation, is used to model the permeability of the sand lithology and distribution 2 is used to model the permeability of the mixed lithology. The clay lithology is assumed to be impermeable, with a permeability of 0.01 mD.

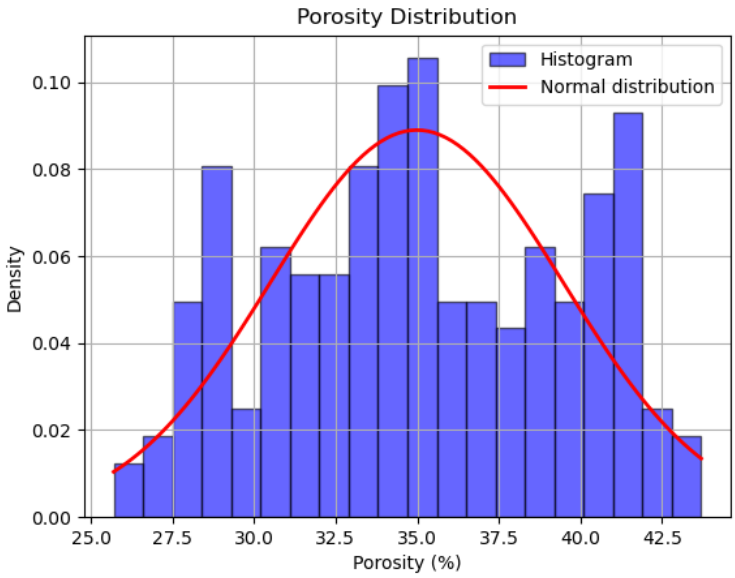

Figure 3.2: The porosity data on the Maassluis formation of NLOG. The histogram indicates that the data can be approximated by a normal distribution (red line) with a mean of 34 and a standard deviation of 5.

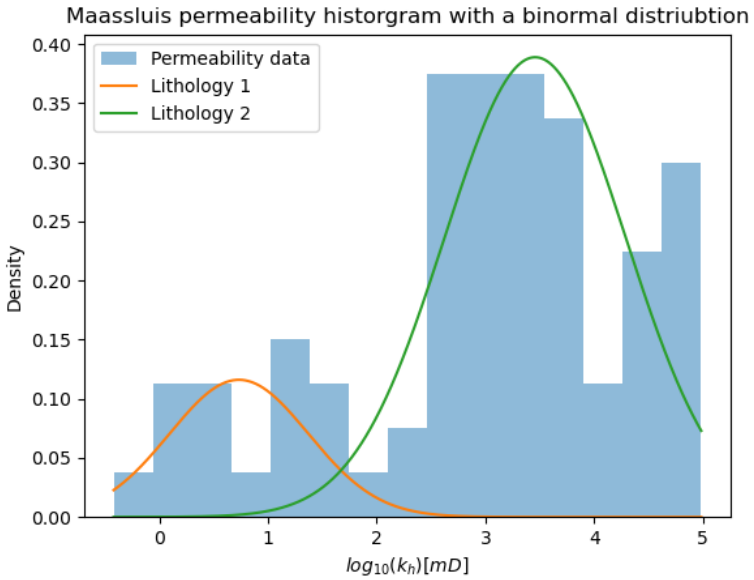

Figure 3.3: Horizontal permeability data measurements from NLOG (histogram), showing two peaks. To these peaks two normal distributions are fitted, that represent the permeability of the sand lithology for the highest permeability values and the lower permeability values for the mixed lithology

With the artificial well data, the porosity can be modeled using the SGS algorithm. Three porosity models are made, each for every type of lithology, where the same variograms are used as for the lithology modeling (Appendix C). The final porosity model is obtained by merging the three models into one, based on the lithology of the individual grid cell. The porosity grids of the PNA and RWK models are shown in Figure 3.4a and Figure 3.4b.

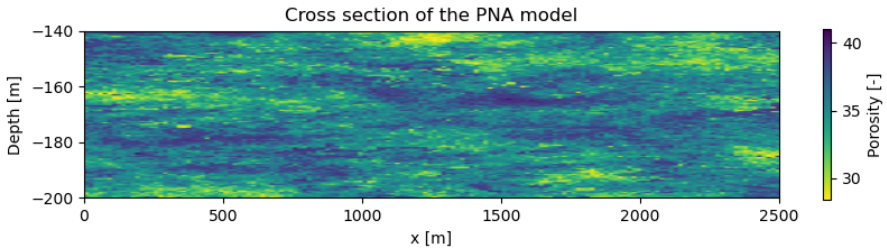

(a) A cross section of the porosity distribution for the PNA model, created with sgsim.

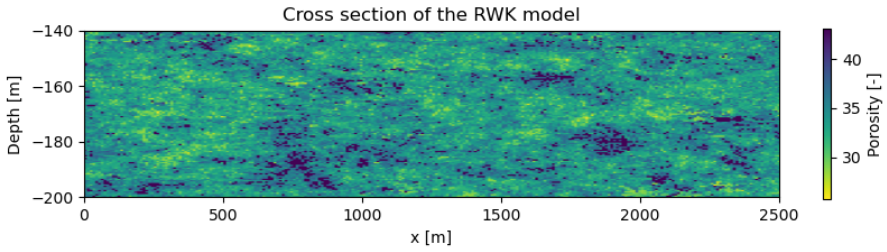

(b) A cross section of the porosity distribution for the RWK model, created with sgsim.

Figure 3.4: The porosity distribution for both stochastic geomodels.

The permeability is modeled similarly to the porosity. Here, two permeability grids will be simulated for lithology 1 and 2. In the procedure co-kriging with the porosity grid as secondary data is performed.

Again, the final permeability grid is obtained by merging the permeability of lithology 1 and 2 based on the lithology of the grid cell. All cells containing clay, will be assigned a permeability of 0.01 mD. The result of the procedure is shown in Figure 3.5a for the PNA model and Figure 3.5b for the RWK model.

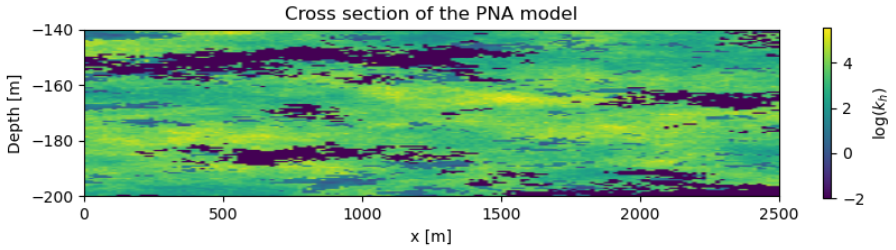

(a) A cross section of the log10 of horizontal permeability for the PNA model, created with sgsim with the cokriging function.

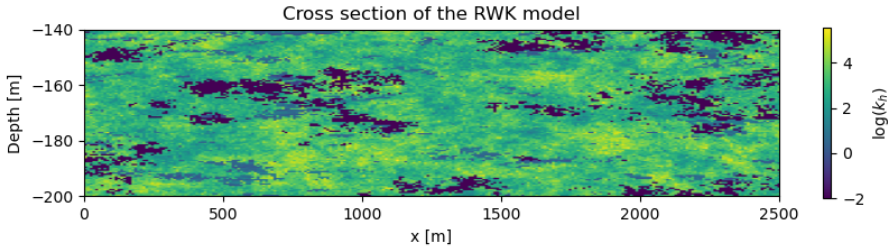

(b) A cross section of the log10 of horizontal permeability for the PNA model, created with sgsim with the cokriging function.

Figure 3.5: The permeability distribution for both stochastic geomodels.

Stochastic model cropping

In the HT-ATES simulations only a portion of the 2.5 x 2.5 km model is used. Therefore the large model needs to be cropped. As the properties, porosity and permeability, are stochastically distributed, the models have spatial variability. Because of that it matters where the section is taken. To deal with this 4 models are cropped at 4 unique locations within per stochastic model. Besides, cropping the model at unique locations, two of the models are rotated by 90 degrees. This is done so that the wells have a different orientation with respect to the correlation directions, used for variography. The effect, cropping the stochastic models has on average porosity and permeability can be seen in Table 3.4.

3.2. Forward Stratigraphic modeling

In Forward Stratigraphic Modeling (FMS), sediments are deposited following (simplified) physical laws, with the goal of simulating a grain size distributions that could represent the subsurface condition (Cano et al., 2023). To perform the Forward Stratigraphic Modeling (FSM) the PyBarSimPseudo3D software is used to model grain size distributions when sea level is varied. The code was developed by Joep Storms in 2003 and is later translated to Python by Guillaume Rongier (both TU-Delft). The code is open-source. PyBarSimPseudo3D can be used for wave-dominated shallow marine deposits, which is adequate for the Maassluis formation (Cano et al., 2023). Parameterization for the physical equation that governs the distribution of sediment is necessary (Cano et al., 2023). The physical equations that are at the basis of this method can be reviewed in (Storms et al., 2002).

3.2.1. Input data for PyBarSim

For the PyBarSim model, the following parameters need to be defined:

- An initial topography is defined. This resulted in a gradient of approximately 1 degree.
- Sea level as a function of time. Here, the sea-level reconstruction of the Early Pleistocene by Berends, Boer, and Wal (2021) is used in combination with an assumed subsidence rate of 0.1 m per thousand years. This value seems to be acceptable as in Veen et al. (2025) a ‘fairly strong subsidence’ is mentioned during the Pleistocene. The subsidence is added to the sea level to obtain a function of relative sea-level change over time, which is visualized in Figure 3.6. To avoid overflowing the PyBarSimPseudo3D code with sea-level inflection points, the sea-level curve is obtained by sampling the reconstruction data every 10.000 years. As the fluctuations are with periods of 41.000 years, sampling with this frequency should preserve the most important features, according to sampling theory.
- Sediment supply as a function of time and along the shore coordinate (y-coordinate). PyBarSimPseudo3D is a sensitive program to the balance between accommodation space and sediment supply. A mismatch between the two leads to an unrealistic distribution of sediments, where kilometer-high ’mountains’ are allowed to form over the simulated time. Therefore, the sediment supply is iteratively calibrated to the model.

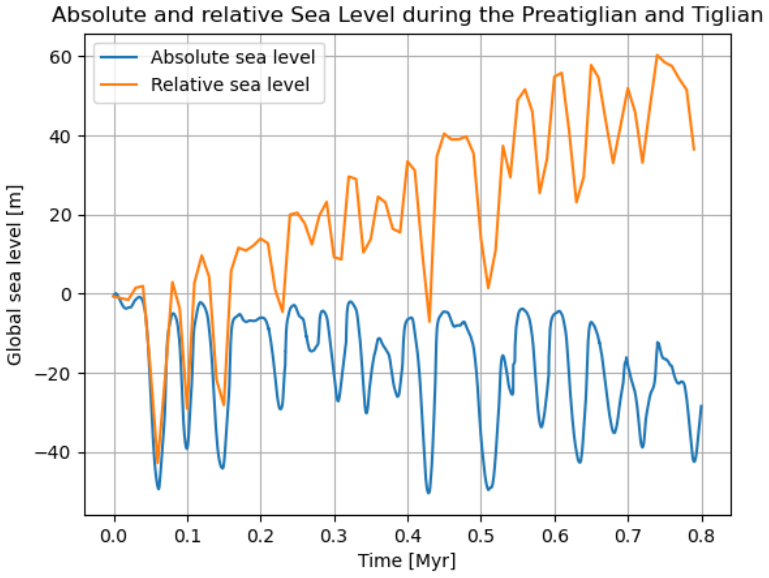

Figure 3.6: The absolute and relative sea level, plotted as a function of time (blue) and the sampled relative sea level (orange). The relative sea level curve combines the absolute sea level curve with a constant subsidence rate. Hence, the deviation grows over time.

3.2.2. PyBarSimPseudo3D output

The output of PyBarSimPseudo3D is a 3D size model on a regular grid (nx, ny, nz), which contains the mean grain size in every grid cell. In addition to the mean grain size, a sorting coefficient is assigned to each grid cell. The resolution is 75 m in the x-direction, 150 m in the y-direction and 0.5 m in the z-direction. The resulting model is shown in figure Figure 3.7. In this figure, the intercalated fine- and coarse-grained sediment layering can be seen. From the figure, the trend of decreasing grain size as one moves seaward can be observed as well. Both observations are in line of what we expect from wave-dominated deltaic deposits under fluctuating sea-level.

From the large PyBarSim model 4 domains have been cropped that show distinguishable grain size distributions. For instance, PyBarSim 1 consists primarily of delta top sediments, where PyBarSim 3 consists of delta top and delta front sediments, based on their grain size. These cropped geomodels will be the input in the HT-ATES simulation. In contrast to the stochastic models, none of the PyBarSim models have been rotated.

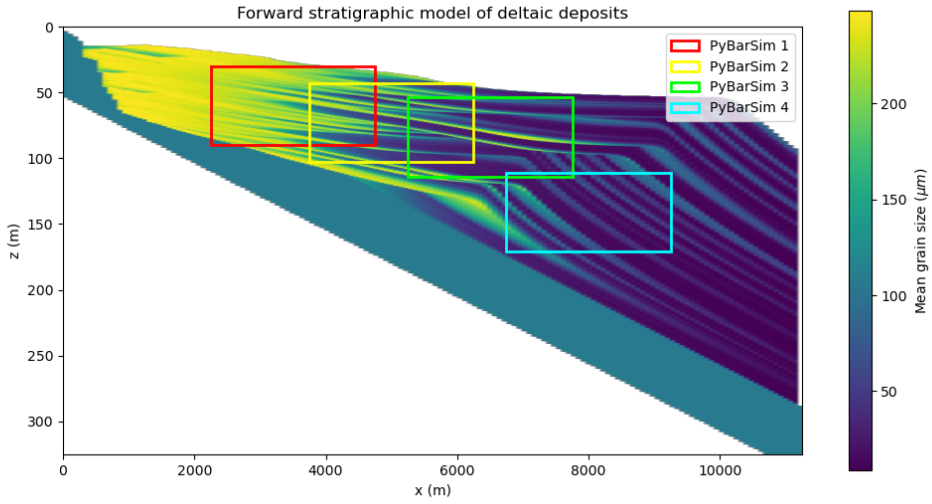

Figure 3.7: The grain size model, created with the PyBarSimPseudo3D code. The four rectangles indicate what parts of the model are going to be used in the HT-ATES simulation.

3.2.3. PyBarSim model postprocessing

A necessary step in unifying the PyBarSim and stochastic models (PNA and RWK) is to convert the coarse resolution of PyBarSim to the 10 x 10 x 0.5 m resolution of PNA and RWK. This is done by linearly interpolating between PyBarSim grain size values.

The remaining challenge is to translate the grain size model into a porosity and permeability model, which can be used for the simulation in chapter 4. In Díaz-Curiel et al. (2024) a relation between grain size, sorting coefficient en porosity is presented:

$$\phi = \frac{(d^{0.5} + 0.5)}{(C_{sc} d^{0.5} + 1)} \tag{3.1}$$

where, d is the mean grain size diameter in cm and C_{sc} is defined by the following relations:

$$C_{sc} = 2.5 + 2.7ln(\sqrt{\frac{d_{75}}{d_{25}}}) \tag{3.2}$$

The resulting porosity model is scaled so that it better represents the porosity data from the cores, presented in Figure 3.2.

	Sand	Water
Heat conduction, $\lambda(Wm^{-1}K^{-1})$	7.7	0.56
Heat capacity $C_p(Jg^{-1}K^{-1})$	830	4200

Table 3.3: The thermal properties of sand and water, derived from Barlet (2025), used in Equation 3.4 and Equation 3.5.

Shepherd (1989) derived the following relation for intrinsic permeability and grain size from experimental data:

$$k = c(d^{1.85}) \tag{3.3}$$

The difference with the well-known Kozeny-Carman equation that relates porosity and grain size squared to permeability is that the Kozeny-Carman equation assumed homometric grains, where the equation by Shepherd is based on experimental data (Díaz-Curiel et al., 2024).

The value of the c parameter in equation Equation 3.3 still has to be determined. To do this a relation between the minimum grain size in the domain and the minimum permeability, assumed to be 0.01 mD (in agreement with section 3.1) and with the maximum grain size of the domain and maximum permeability provided by NLOG (Figure 3.3). The resulting porosity and permeability distributions are shown as an example for PyBarSim2 in Figure 3.8a and Figure 3.8a, respectively.

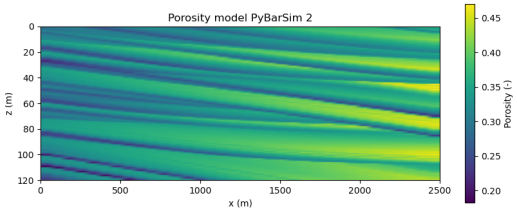

(a) The porosity of PyBarsim2.

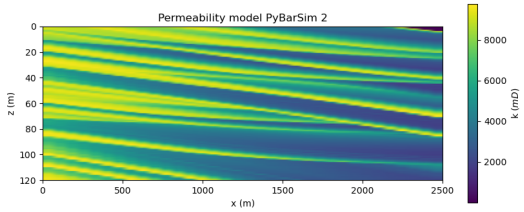

(b) The permeability of PyBarsim2.

3.3. Thermal property modeling

In the HT-ATES simulation properties in addition to porosity and horizontal permeability, namely, vertical permeability, thermal conduction, and heat capacity need to be defined. How these properties will be defined is explained below.

The vertical permeability will be based on an anisotropy ratio. In case studies like ((Bloemendal, Phil Vardon, et al., 2020)) anisotropy ratios of 2 to 5 are mentioned for the Maassluis formation. These values will be used for lithology 1 and 2. For clay, the permeability is already near 0 mD. There, an anisotropy ratio of 1 is assumed.

The bulk thermal conductivity, λ_b and the bulk volumetric heat capacity, $C_{V,b}$ of the grid cells are calculated using the porosity-based equations Equation 3.4 and Equation 3.5, respectively (adapted from (Zhang and Michalowski, 2015)).

$$\lambda_b = \lambda_s^{1-\phi} \cdot \lambda_f^{\phi} \tag{3.4}$$

$$C_{V,b} = \phi\rho_f C_{p,f} + (1-\phi)\rho_s C_{p,s} \tag{3.5}$$

3.4. Geomodel analysis

In this section, the geomodels are analyzed based on the values of the properties of permeability and porosity, as well as their spatial distribution. First, the geomodeling results are related to the findings in section 2.3. Then, the differences between the geomodels need to be assessed so that the HT-ATES simulation outcomes can be linked to the geomodel characteristics. The comparison will start by distinguishing geomodels in a qualitative matter. The geomodels are then described quantitatively.

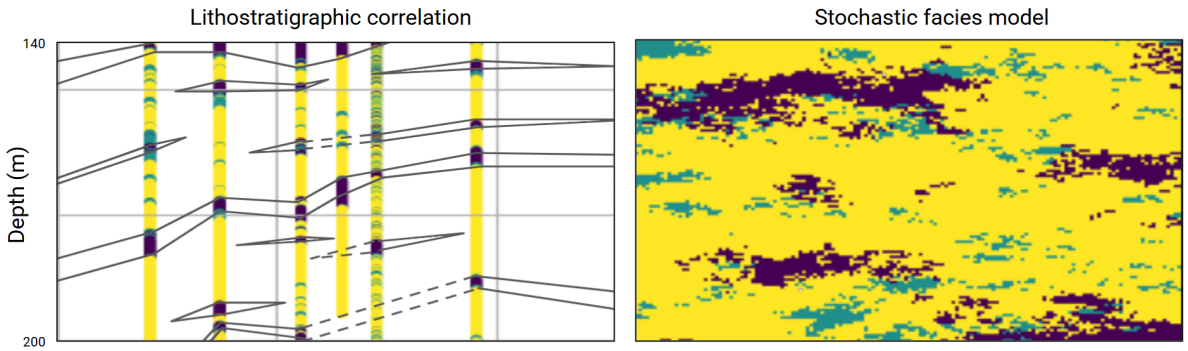

Figure 3.9: a snipped of the lithostragraphic correlation next to the stochastic facies model

Reflection on the goal of Chapter 3
The primary goal in this chapter is to capture characteristic features of the Maassluis formation.

Stochastic geomodels

From Figure 3.9 it can be concluded that stochastic modeling of facies captures the findings of the lithostratigraphic interpretation of section 2.3, moderately. It can be seen that in both images elongated clay wedges can be found. As the stochastic models use the well data proportions, a decent estimate of the amount of clay is made.

The exact position of the clay intervals does not match entirely. Furthermore, a clay layer that spans the entire domain, as shown in the lithostragraphic correlation is absent. Many small clay patches are generated compared by stochastic modeling that are not present in the lithostratigraphic correlation. As the resolution at which this correlation is performed is relatively coarse in the horizontal direction, it is possible that the clay patches would be present.

Process based geomodels

When comparing figure Figure 3.7 with the sequence stratigraphic correlation in Figure 2.9, differences can be observed as well. In Figure 3.7, many more sequences are generated in the 60-meter interval than are indicated in the stratigraphic correlation of the interpreted sequence and in the sequence stratigraphic interpretation of (Slupik et al., 2007). These generated sequences are also much thinner than observed in the well data. The input parameters of PyBarSimPseudo3D could be calibrated so that output grain size distribution corresponds better to the well data.

The PyBarSimPseudo3D has a grain size range of 5 to 250 micrometers, which is in line with what Slupik et al. (2007) found.

Qualitative geomodel comparison
Clear differences can be seen between the Pybarsim model (PBSM, Figure 3.11b), which has large, flat dipping clusters that extend over the entire domain compared to the randomly organized clusters of the Pijnacker model (PNA, Figure 3.11a). This is an indicator of the importance of how geomodels are constructed in representing accurate preferential flow paths.

3.4.1. Quantative geomodel comparison

Net to gross
The net to gross ratio (NG) is difficult to estimate for PyBarSim models, as the discontinuities in the permeability field are not as sharp as in the stochastic models. However, an estimation of the NG can be made on the basis of a horizontal permeability threshold.

The chosen threshold is the permeability of an average-sized silt, calculated by Equation 3.3. The average diameter of the silt particles is 32.5 micrometers. The calculated permeability threshold is then 353 mD.

The NG is calculated for all geomodels, with the results summarized in table Table 3.4.

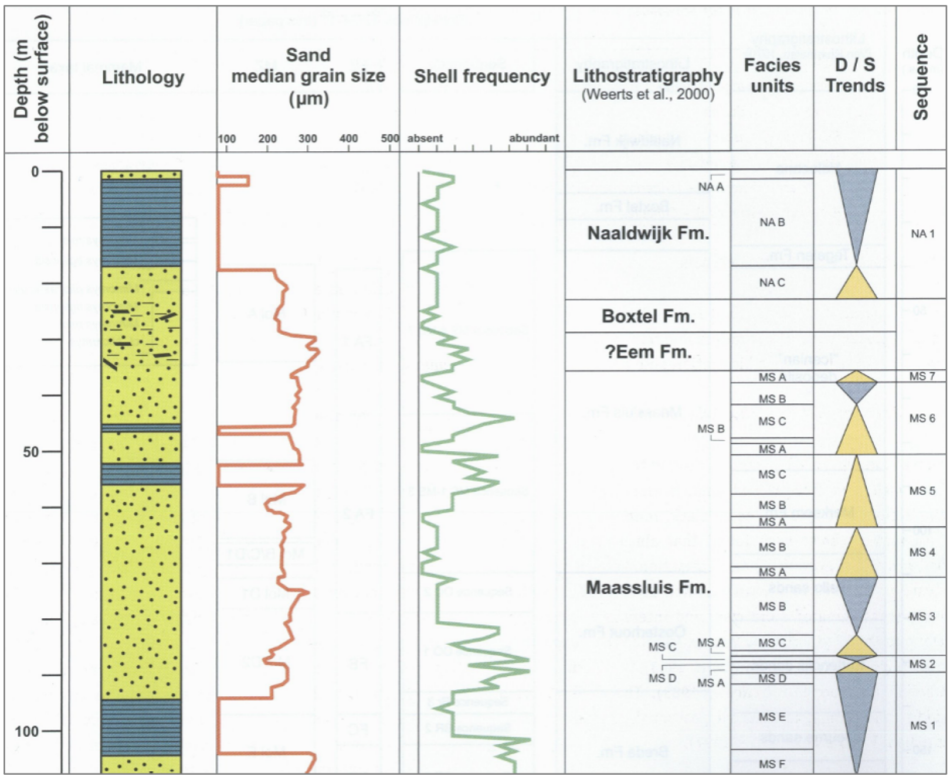

Figure 3.10: A snipped of the results of Slupik et al. (2007), where lithology and grain size are shown for the Maasslius formation. Besides this sequences are intepreted based on grain size data.

Name	ID	$\mu(\phi)$	$\sigma(\phi)$	$\mu(k_h)[mD]$	$\sigma(\log(k_h))$	$NG[-]$	C_V
PNA	1	0.35	0.02	5895.94	2.18	0.49	4.71
PNA	2	0.35	0.02	4401.1	2.1	0.57	3.27
PNA	3	0.36	0.02	6467.14	2.12	0.62	2.42
PNA	4	0.35	0.02	3978.17	2.18	0.48	3.44
RWK	1	0.34	0.03	5036.62	1.51	0.70	2.68
RWK	2	0.34	0.03	4195.94	1.61	0.68	2.68
RWK	3	0.35	0.03	4510.13	1.65	0.68	2.58
RWK	4	0.34	0.03	4330.89	1.58	0.69	2.68
PBSM	1	0.33	0.04	10967.87	0.12	1.0	0.21
PBSM	2	0.33	0.04	5093.91	0.44	1.0	0.79
PBSM	3	0.34	0.04	1881.62	0.56	0.60	1.55
PBSM	4	0.34	0.04	816.17	0.5	0.54	1.23

Table 3.4: The comparison of all geomodels for: porosity, standard deviation of porosity, permeability, standard deviation of permeability, net to gross ratio and coeffcient of variation.

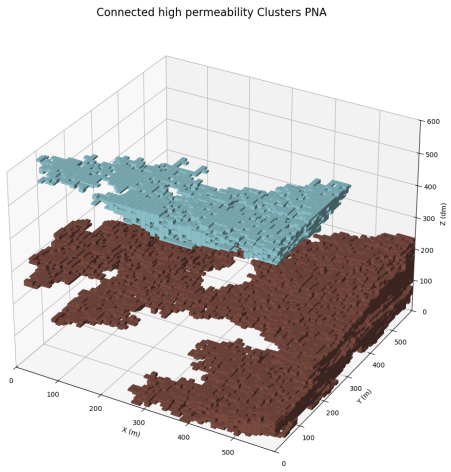

(a) Connectivity clusters near the PNA well.

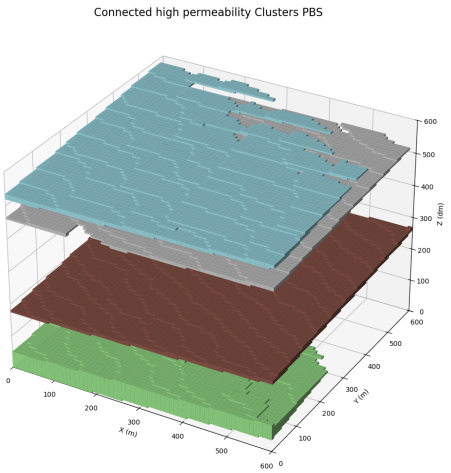

(b) Connectivity clusters near the PBS well.

Coefficient of variation

Static heterogeneity analyzes have been performed on all geomodels. The mean and variance of porosity and the log of permeability are calculated. From these, the coefficient of variation, C_v (Equation 3.6), is calculated (Lake and Jensen, 1991).

$$C_V = \frac{\sqrt{Var[k]}}{E[k]} \tag{3.6}$$

The heterogeneity metrics that is presented come with limitations, as it reflects a statistic on the permeability distribution, not how the permeability is distributed within the geomodel. To illustrate this, consider a permeability model created with SGS and a permeability model created by implementing white noise (meaning an uncorrelated permeability distribution). Both models can have the same mean and variance, resulting in the same coefficient of variation. However, flow will behave differently in the stochastic geomodels, as high-permeable grid cells are connected, which allows for preferential flow paths. In the white noise example, no preferential flow paths exist. This indicates that the statistic metrics only how heterogeneous the aquifer is, not how well the permeability is connected.

Table 3.4 show that the PNA geomodels, generally have the highest coefficient of variation. This is followed by the RWK model and, lastly, the Pybarsim model 1 to 4 (in that order). The difference between the PNA and RWK heterogeneity coefficients can be attributed to the general lithology proportions. The PNA model contains more of the clay lithology approximately 20 percent compared to the 10 percent in the RWK model. This translates directly into all the coefficients computed.

The difference between the PNA and RWK heterogeneity coefficients can be attributed to the general lithology proportions. The PNA model contains more of the clay lithology approximately 20 percent compared to the 10 percent in the RWK model. This translates directly into all the coefficients computed.

4

HT-ATES simulation

This chapter provides an overview of the numerical simulation set-up. First, some background information on the simulation software is provided. Afterwards, the numerical set-up is discussed. Lastly, the input parameters and the number of simulations in this study is presented.

4.1. DARTS

For the simulation of the HT-ATES system, open-DARTS (Delft Advanced Research Terra Simulator) will be used. DARTS uses the finite-volume approximation for spatial discretization (D. Voskov et al., 2024). DARTS is a fully implicit solver, which uses the Back-Ward Euler method for time integration (D. Voskov et al., 2024).

The reason DARTS will be used is the efficient solving method, the possibility to perform multiple simulations in parallel, and its reliability in reservoir simulation, which will be discussed later in this section (D. Voskov et al., 2024). Hence, it is a practical tool for handling a large number of simulations.

DARTS is capable of efficiently simulating geothermal, HT-ATES and CCS systems, using operator-based linearization (OBL) (D. Voskov et al., 2024). Here, a distinction is made between space dependent variables (porosity, permeability, heat capacity, and thermal conductivity) and state variables (name of: pressure, temperature and composition) (Khait and D. V. Voskov, 2017). The governing partial differential equations, conservation of mass and energy (Equation 4.1 and Equation 4.2, respectively, (Chen, D. Voskov, and Daniilidis, 2025)), are rewritten in operator form. The operator form of the equations can be found in Appendix D. Here, the operator form is a function of the space and state variable (Khait and D. V. Voskov, 2017). To keep this section brief, the derivation and definitions of the operators can be found in Appendix D, which is based on the works of Chen, D. Voskov, and Daniilidis (2025).

Operator values are calculated beforehand, based on a predefined plausible range of pressures and enthalpy, in case of geothermal or (HT-)ATES simulations. This is done by calculating the values of the operators at specific values of the state variables, i.e. at discrete nodes. When solving the equations in the simulation, multilinear interpolation is performed to obtain operator values at all plausible values of the state variables (Khait and D. V. Voskov, 2017). The resolution of the discretization of the physics is determined by the pressure and enthalpy ranges considered, and by the number of OBL-points that are used to discretize it. This number has to be specified before the start of the simulation. A high number of points indicates a high resolution in the discretized physics and a higher solver accuracy (Chen, D. Voskov, and Daniilidis, 2025).

The main benefit in discretizing the operators and linearly interpolating between node values is gained in fast Jacobian matrix computation. This because the need for computationally expensive numerical derivatives of nonlinear functions is hereby omitted, as the nonlinear physics is linearized between the nodes (Khait and D. V. Voskov, 2017). Because of this, the derivatives are provided directly by the gradient between the interpolation nodes (Khait and D. V. Voskov, 2017).

$$\frac{\partial}{\partial t}(\phi \sum_{p=1}^{n_p} x_{cp}\rho_p s_p) + div \sum_{p=1}^{n_p} x_{cp}\rho_p s_p \vec{u}_p + \sum_{p=1}^{n_p} x_{cp}\rho_p \tilde{q}_p = 0, c = 1, ..., n_c \tag{4.1}$$

$$\frac{\partial}{\partial t}(\phi \sum_{p=1}^{n_p} \rho_p s_p U_p + (1-\phi)U_r) + div \sum_{p=1}^{n_p} h_p \rho_p \vec{u}_p + div(\kappa \nabla T) + \sum_{p=1}^{n_p} h_p \rho_p \tilde{q}_p = 0 \tag{4.2}$$

$$\vec{u}_p = -\mathbf{K}\frac{k_{rp}}{\mu_p}(\nabla p_p + \gamma_p \nabla D) \tag{4.3}$$

DARTS has been proven to be a reliable software for geothermal simulations, as it is validated against other reservoir simulation software in Y. Wang, D. Voskov, Khait, et al. (2020). Here, 1D, 2D and 3D geothermal simulations are performed under identical conditions with different solver software, namely DARTS, AD-GRPS and THOUGH2 (Y. Wang, D. Voskov, Khait, et al., 2020). The results of the tests compared well to each other, as in the 2D simulation the relative difference in the temperature distribution in the aquifer was maximally 1.6 percent point between DARTS and THOUGH2 and a maximum of 3.0 percent point between AD-GRPS and DARTS (Y. Wang, D. Voskov, Khait, et al., 2020). As geothermal and HT-ATES involve similar physical processes, it is assumed that DARTS is able to reliably simulate HT-ATES systems. In the 3D case, the normalized difference in temperature per layer between ADGPRS and DARTS stayed below 1.0 percent (Y. Wang, D. Voskov, Khait, et al., 2020).

4.2. Simulation set-up

4.2.1. Operational parameters and System design

An HT-ATES system with one hot well and one warm well is considered. In this study, it is chosen to focus on the thermal behavior around the hot well. In doing so, the behavior around the warm well will not be considered. This way allows geometrical aspects of the thermal plume to be studied with a high resolution.

3 Volumes are considered, which are thought to be in a plausible range for HT-ATES systems, namely 200, 600 and 1000 $\cdot 10^3\ m^3 year^{-1}$.

To avoid interference effects from the warm well, the warm well is placed further apart. In this study, a distance of 10 thermal radii is used between the hot and warm well, with the thermal radius defined as (Beernink et al., 2024):

$$R_{th} = \sqrt{\frac{c_w V}{c_{aq}\pi H}} \tag{4.4}$$

Based on annual volumes, the aquifer height (60 m) and heat capacity (2860 kJ m3 K) the thermal radii are calculated. The results can be found in Table 4.1.

Scenario	Small	Medium	Large
Injected volume $[m^3 year^{-1}]$	200.000	600.000	100.000
Estimated thermal radius $[m]$	47	82	106
Distance hot and warm well $[m]$	500	800	1100
Extent of fine mesh $[m]$	400	450	500
Total number of grid cells	1,243,840	1,684,020	2,169,440

Table 4.1: Specifications of the simulation per scenario.

A block pattern injection scheme is considered for all simulations. It is chosen to divide an injection cycle into 4 parts that constitute one year in time. First, for a period of 120 days the hot well is charged by injecting hot water, then there is a 60 day rest period, followed by 120 days of discharge from the hot well, and lastly a rest period of 65 days (Figure 4.1).

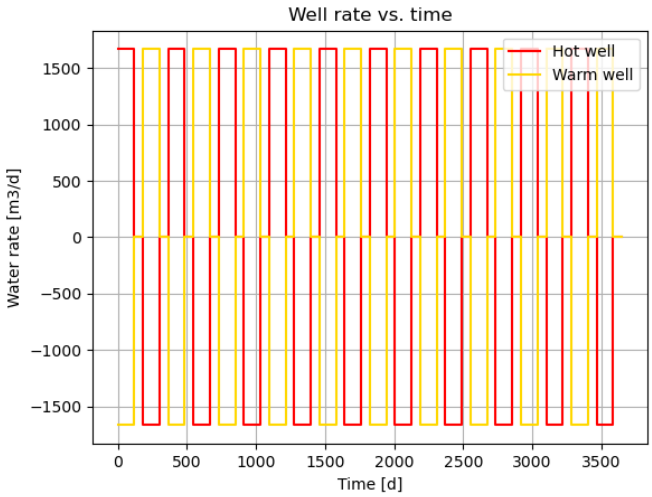

Figure 4.1: The injection scheme, shown as an example for the 200.000 $m^3 year^{-1}$ storage volume.

A sine-like injection pattern might better resemble realistic energy demands and availability. However, with a block pattern, DARTS is able to upscale the time steps rapidly, resulting in faster simulation results. Akın, Bruhn, and Daniilidis (2025) showed for a HT-ATES case study under homogeneous aquifer conditions that the injection scheme used (that is, the block pattern or the sinusoid with a similar annual injection volume) translated into a roughly 2 percent point difference in energy efficiency. Therefore, the results obtained in the block pattern injection scheme are considered adequate.

4.2.2. Grid and spatial resolution

To enhance the accuracy of the solution without overflowing the simulator with a large amount of grid cells, it is chosen to use a variable grid size in the x- and y-direction. The grid cell size is unchanged in de z-direction, with a constant dz of 0.5 m. In the domain surrounding the hot well, a fine mesh with cell sizes of 10 by 10 by 0.5 m (x, y, z-direction, respectively) is implemented. This extent of the fine mesh increases when the injection volume increases to a maximum dx and dy of 100 m. The extent of the fine mesh and the total number of cells in the simulation can be found in Table 4.1. A map view of the grid is shown in Figure 4.2.

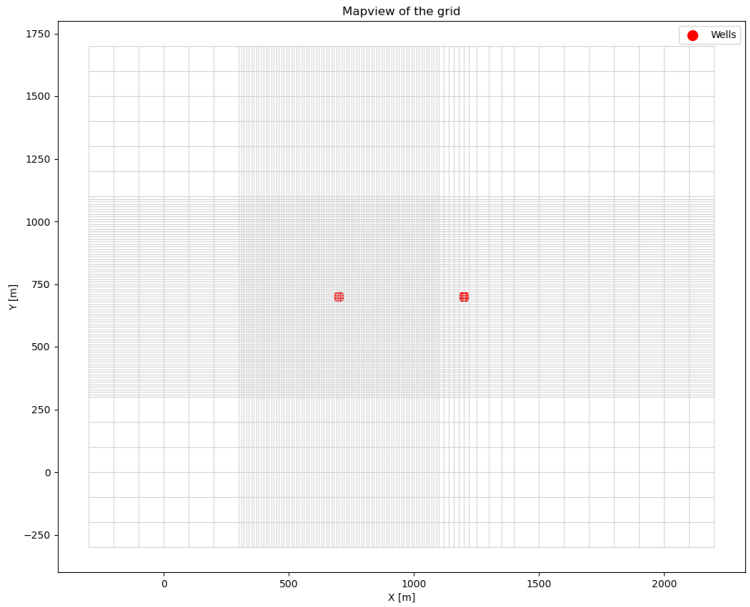

Figure 4.2: Mapview of the grid for the 200.000 m3 per year injection scenario.

The porosity, permeability, volumetric heat capacity, and thermal conductivity in the fine mesh are directly copied from the geomodels constructed in chapter 3, as the resolution between the simulation grid and the geomodel matches exactly. The cells outside the fine mesh obtain the arithmetic average property of the cells within the fine mesh. The main purpose of these cells is to add space between the hot well and the boundaries. Therefore, the addition of heterogeneity to them is omitted. Figure 4.3 illustrates this concept. Here, the fine mesh is the area inside the red rectangle. All other cells have a constant average property, as is clearly visible by the homogeneous color those cells have. Note, that the warm well is positioned in the homogeneous grid.

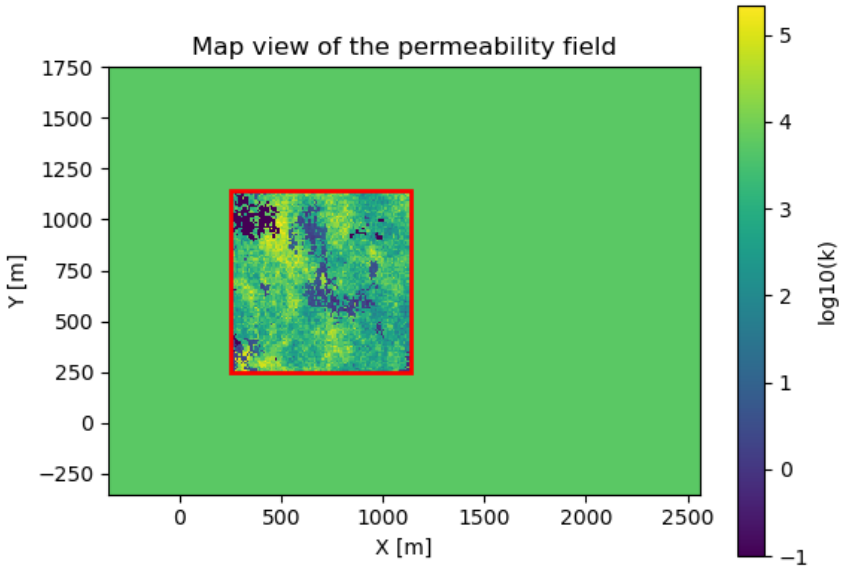

Figure 4.3: Mapview permeability taken at z = 145 m for the RWK geomodel.

4.2.3. Parameter space

To thoroughly test the impact of subsurface heterogeneity parameters that strongly influence the performance of HT-ATES systems are varied. These parameters are obtained from sensitivity analyzes in the literature. From Heldt, Beyer, and Bauer (2024), Beernink et al. (2024) and Gao et al. (2024), the following parameters are derived: injection volume, injection temperature, and horizontal and vertical permeability.

First, the three injection volumes mentioned above are considered, namely 200.000, 600.000 and 1.000.000 cubic meters per year.

Second, two injection temperatures are considered 90 and 73 degrees Celsius. The temperature of 73 degrees Celsius was obtained from the feasibility study for HT-ATES on the campus of TU-Delft Bloemendal, Phil Vardon, et al. (2020).

Third, the horizontal variation of permeability is a direct result of geomodeling, since the models show distinguishable permeability distributions. To show the effect that vertical permeability has, anisotropy ratios of 2 and 5 are considered for the RWK and PNA models (Equation 4.5). These ratios are common for the Maassluis formation in several case studies (Bloemendal, Phil Vardon, et al., 2020), (Bloemendal and Beernink, 2023), (*Inpassing HTO Rotterdam Nesselande door Uitvoeringsteam WarmingUP (Deltares, Eneco)* n.d.).

$$a = \frac{k_h}{k_v} \tag{4.5}$$

In summary, in this study 12 geomodels, 3 injection volumes, 2 injection temperatures, and 2 anisotropy ratios are considered. All parameter combinations are tested against each other, resulting in a total of 144 heterogeneous simulations that are performed.

4.2.4. Homogeneous reference cases

To assess the differences between homogeneous and heterogeneous HT-ATES systems, simulations with homogeneous geomodels have been performed.

Of the PNA and RWK geomodel, a homogeneous model is created such, where the arithmetic average is taken of the porosity, permeability, heat capacity and thermal conductivity over the entire 2.5 x 2.5 km domain for the aquifer. The aquitard permeability is kept similar to the heterogeneous simulations. In the Pybarsim case, 3 separate homogeneous models are created, as the individual Pybarsim geomodels show large contrasts in permeability. In Table 4.2 the properties of each homogeneous geomodel are shown.

Geomodel 600k	PNA	RWK	PyBarsim 1	PyBarsim2	PyBarsim3
Porosity $[-]$	0.352	0.344	0.328	0.332	0.341
Horizontal permeability $[mD]$	5209	4487	11010	5082	1855
Heat capacity $[kJm^{-3}K^{-1}]$	2904	2887	2885	2864	2881
Thermal conductivity $[kJm^{-1}day^{-1}K^{-1}]$	215	219	227	225	221

Table 4.2: Specifications of the homogeneous comparisons.

For homogeneous simulations, an injection volume of 600.000 cubic meters per year is considered. The rest of the tested parameters are kept the same. This results in 5 models being tested for: one volume, two injection temperatures (73 and 90 degrees Celsius), and 2 anisotropy ratios (2 and 5). This results in 20 homogeneous simulations. When added to the number of heterogeneous simulations, the total number of simulations is 164.

5

Interpretation of simulation data

In this chapter the data gained from performing HT-ATES simulations with DARTS is analyzed. The simulations in DARTS returns the production data, which is the well temperature in K, well pressure in bar and the well rate in cubic meters per day. Besides the well data, the temperature and pressure in the geomodel cells is obtained for multiple time steps. These data allow for a spatial analysis of the temperature distribution.

This chapter is organized in the following way. First, the energy efficiency is obtained from the well temperature and rate. Here, heterogeneous simulations and their homogeneous counterparts are compared, to gain an insight in what the effect is of incorporating geomodel heterogeneity on HT-ATES simulations. Then, the parameter sensitivity between heterogeneous simulations is investigated. Second, the thermal plume spread, in relation to geomodel characteristics is explored.

5.1. Energy efficiency

The energy efficiency of HT-ATES systems tells us how much of the energy that is stored can be retrieved. If more energy is retrieved a project will be more viable.

The energy efficiency is defined as the energy that is extracted from the subsurface over the energy injected into the subsurface. The energy efficiency is calculated per storage cycle, in this case thus per year. The calculation is perfomed via Equation 5.1, as is done in numerous studies, for instance in Geerts et al. (2025). Here, V_i and V_e represent the volumes injected and extracted per year in $m^3 year^{-1}$). $\overline{T_e}$ and T_{gw} are the extraction temperature, averaged at the well screen, and the average initial groundwater temperature in K, respectively. In the cases considered in this study, the injection and extraction volumes are balanced per year. Therefore, V_e is equal to V_i. that can both be omitted from equation Equation 5.1.

$$\eta = \frac{V_e \cdot (\overline{T_e} - T_{gw})}{V_i \cdot (T_i - T_{gw})} \tag{5.1}$$

5.1.1. Homogeneous vs. heterogeneous simulations

Homogeneous and heterogeneous simulations behave differently. In Figure 5.1 the energy efficiency is plotted for all 10 cycles. In this plot the injection volume is 600,000 cubic meters per year for all cases. Figure 5.1 shows the average evolution of the energy efficiency between different geomodels, being: PNA, RWK, PBS1, PBS2 and PBS3. η is averaged for the cases that are constructed with the same geomodel. As an example: the values in Figure 5.1 for PBS1 are the result of averaging the energy efficiency per year for the four simulations with, T_{inj} = 90 and kh/kv = 2, T_{inj} = 90 and kh/kv = 5, T_{inj} = 73 and kh/kv = 2 and T_{inj} = 73 and kh/kv = 5. The key characteristics of Figure 5.1 are summarized in Table 5.1.

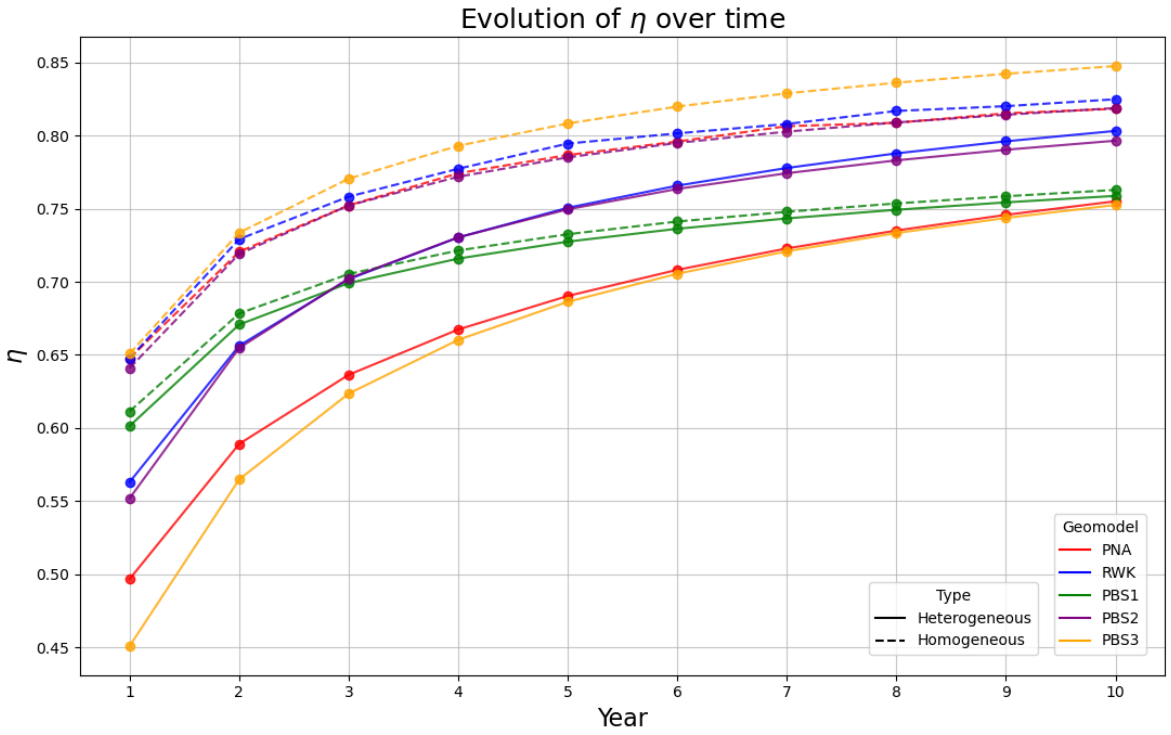

Figure 5.1: Caption

Geomodel	$\Delta\eta_{1,homo,hetero}$ [%]	$\Delta\eta_{10,homo,hetero}$ [%]	$\eta_{1,hetero}$ [%]	$\eta_{10,hetero}$ [%]	$\Delta\eta_{9,10,homo}$ [% y^{-1}]	$\Delta\eta_{9,10,hetero}$ [% y^{-1}]
PNA	15.1	6.3	49.7	75.6	0.31	0.93
RWK	8.5	2.2	56.3	80.3	0.47	0.71
PBS1	1.0	0.4	60.1	75.9	0.43	0.44
PBS2	8.9	2.2	55.2	79.6	0.46	0.62
PBS3	20.0	9.5	45.1	75.3	0.53	0.89

Table 5.1: The characteristics that highlight how homogeneous and heterogeneous simulations behave. From left to right, the collumns indicate: the difference in energy efficiency for the first year, the difference in energy efficiency for the tenth year, the energy efficiency of the heterogeneous simulation in the first year, the energy efficiency of the heterogeneous simulation in the tenth year, the increase in energy efficiency between the ninth and tenth year for the homogeneous simulations and the increase in energy efficiency between the ninth and thenth year for the heterogeneous simulation.

From Figure 5.1 and Table 5.1 the following points can be noted:

1. The overall energy efficiency is lower for heterogeneous simulations than for homogeneous simulations over the simulated 10-year time period.

2. The energy efficiency for heterogeneous cases starts of relatively poor compared to the homogeneous cases. However, the energy efficiency of heterogeneous cases improves greatly over the first cycles. Over 10 years, the homogeneous and heterogeneous efficiencies seem to converge, which is supported by comparing the increase in energy efficiency in Table 5.1 from the ninth to the tenth cycle between the homogeneous and heterogeneous simulations. From Table 5.1 it can be seen that the rate of convergence is geomodel dependent.

3. The energy efficiency of homogeneous simulations of PNA, RWK and PBS2 behave similar, as their horizontal and vertical permeability are similar. Their heterogeneous counterparts show a larger spread in energy efficiencies over time. In this situation, the PNA model shows the largest decrease in energy efficiency over the simulated time period, compared to its heterogeneous counterpart.

4. The energy efficiency of the heterogeneous PBSM1 in the first year is the highest compared to all other heterogeneous simulations. However, the tenth year efficiency of PBSM1 ranks third of all heterogeneous models.

The main driver behind all observations is that the thermal plume in heterogeneous simulations is distorted compared to the homogeneous case. Next, per observation explanations will be given, that will dive deeper in this matter.

1. The distortion of the thermal plume is caused by heterogeneity in the permeability of the geomodel, as permeability heterogeneities create preferential fluid pathways. Figure 5.2a and Figure 5.2b show the difference in thermal plume shape between the homogeneous and heterogeneous simulations. The distortion of the thermal plume leads to an increase in plume surface area, whilst the injected volume is constant. Therefore, the ratio area over volume (A/V) increases, resulting in a favorable condition for thermal conduction losses to increase. In (HT-) ATES simulations it is desired to minimize A/V, to maximize the energy efficiency (Bloemendal and Hartog, 2017). From figures Figure 5.2a and Figure 5.2b, it can be seen that after the seventh cycle, the A/V of the heterogeneous is still larger than the ideal case.

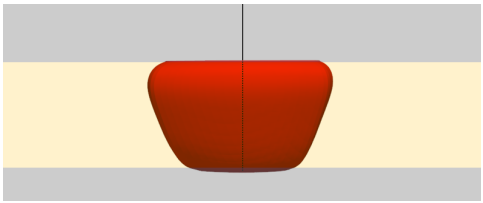

(a) The surface for the PBS3 homogeneous case.

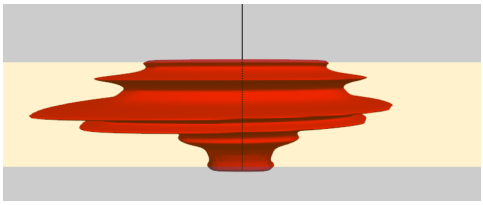

(b) The surface for the PBS3 heterogeneous case.

Figure 5.2: The surface for which $T = (T_{in} - T_{am})/2 =$ of simulations in the seventh cycle.

2. The higher increase in energy efficiency for heterogeneous simulations than for homogeneous simulations can be explained by looking at the surface area of the thermal plume over time. From Figure 5.3a and Figure 5.2b it can be seen that the surface area of the plume is reduced when more simulation cycles have passed. This, because low-permeable parts of the aquifer are heated up by the surrounding permeable parts through thermal conduction. Once these parts are heated, the heat loss to them will be reduced, resulting in an increase in energy efficiency.

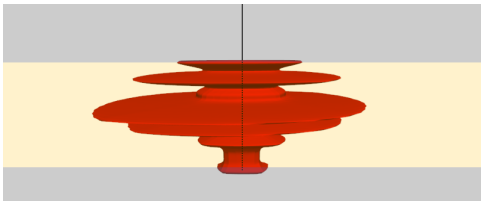

(a) The surface for the PBS3 heterogeneous case in the first year.

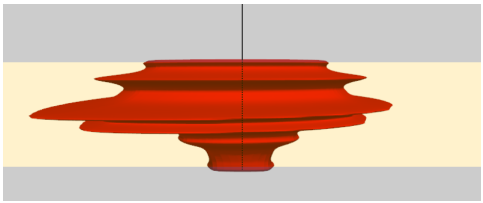

(b) The surface for the PBS3 heterogeneous case in the seventh year.

Figure 5.3: The surface for which $T = (T_{in} - T_{am})/2 =$ of simulations.

From Figure 5.1 and Table 5.1 it can be observed that the increase in η between year 1 and year 10 varies between the heterogeneous simulations. When comparing Table 5.1 with the quantification of the geomodels in Table 3.4, a trend can be observed. A low NG results in a large difference between the first- and tenth-year efficiency. Furthermore, a low NG results in a slower convergence to the homogeneous energy efficiencies. PNA and PBS3, have the lowest NG, of 0.48 to 0.62 and 0.60, respectively. Both simulations have the largest difference in η_1 and η_{10} and the largest increase in efficiency between the ninth and tenth cycle. Why PBS3 has a larger difference between η_1 and η_{10} than the PNA model, is explained in the next paragraph.

3. The reason for the difference in energy efficiencies between the heterogneous PNA and RWK simulations be explained by comparing the NG. The change in NG translates to the average size of the clustered impermeable material for PNA and RWK. In Figure 5.4a and Figure 5.4b this becomes clear. The RWK clusters are smaller than the PNA clusters. If the clay clusters are larger they, take longer to heat up through conduction than when they are smaller. Furthermore, the more impermeable material is present, the more the injected water is forced through selective paths, which distorts the thermal plume shape more, resulting in an increased A/V and a lower energy efficiency.

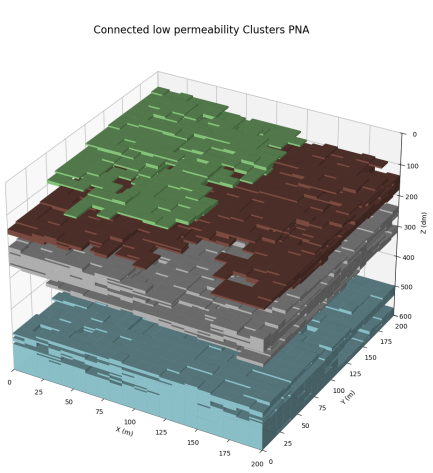

(a) Map of impermeable clusters, PNA.

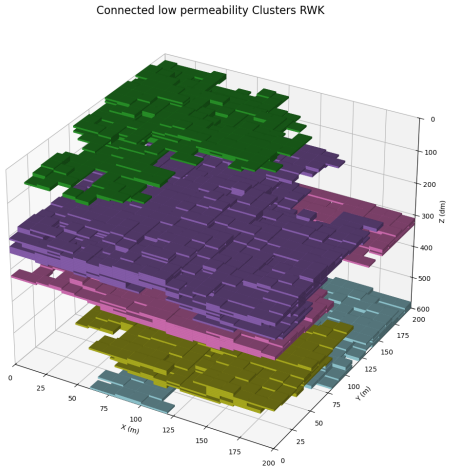

(b) Map of impermeable clusters, RWK.

Figure 5.4: The clay clusters of the stochastic geomodels. Different colors represent different connected clusters.

The reason why PBSM3 under performs to cannot be explained by looking at the NG, as the NG

of PBSM3 is higher than PNA for instance. To explain this, the geomodel architecture needs to be examined. If Figure 5.5a and Figure 5.5b are compared, it can be seen that the high-permeability zones are concentrated in thin layers for PBS3. That the permeability is concentrated to narrow intervals, results in the severe distortion of the thermal plume shape, increasing A/V.

4. PBSM1 is the model with the highest overall horizontal and vertical permeability. I also has the lowest coefficient of variation and NG of all heterogeneous models (Table 3.4). As the PPBSM1 model is relatively homogeneous, the shape of the thermal plume at the start of the simulation is closest to the ideal shape that minimizes A/V, compared to all other heterogeneous cases. This explains the high observed first year energy efficiency. The reason for the poor efficiency over longer time is the high overall vertical permeability. This, allows for free convection, which is strong enough to displace warm water to the top, therefore reducing energy efficiency. As there are not enough low permeable layers in this heterogeneous model, buoyancy driven flow is not limited. This leads to large heat losses. This is supported by observing the cross section of the thermal plume for PBS1 (Figure 5.6).

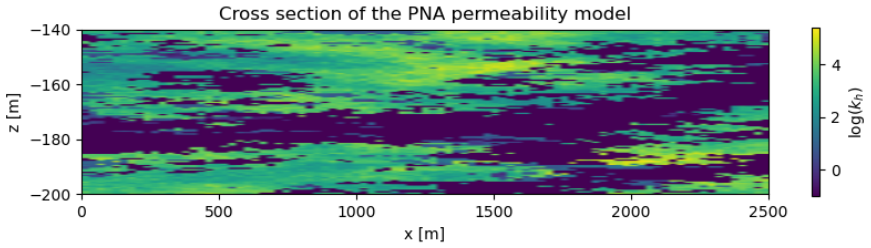

(a) The permeability distribution of the PNA geomodel.

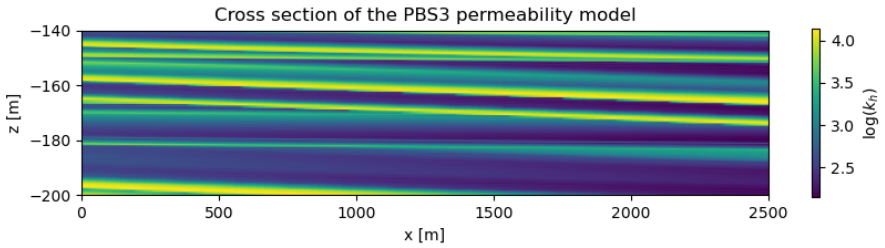

(b) The permeability distribution of the PBS3 geomodel.

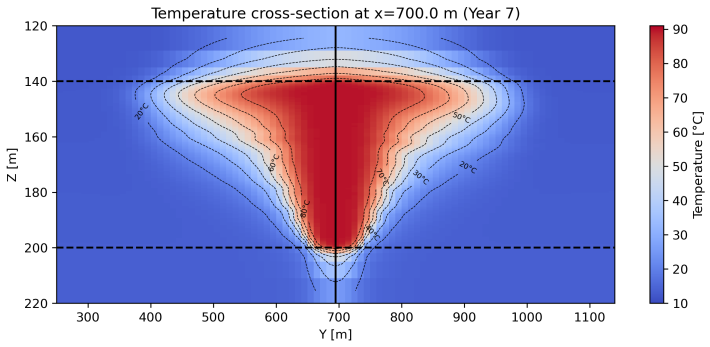

Figure 5.6: A cross section of the thermal plume for the PBS1 simulation.

From the explanations above, it can be concluded that the distortion of the thermal plume is a key component that influences how homogeneous and heterogeneous simulations behave compared to each other, especially in the first years of simulation. The long-term behavior of HT-ATES simulations is dependent on heterogeneity and the potential of developing buoyancy-driven flow.

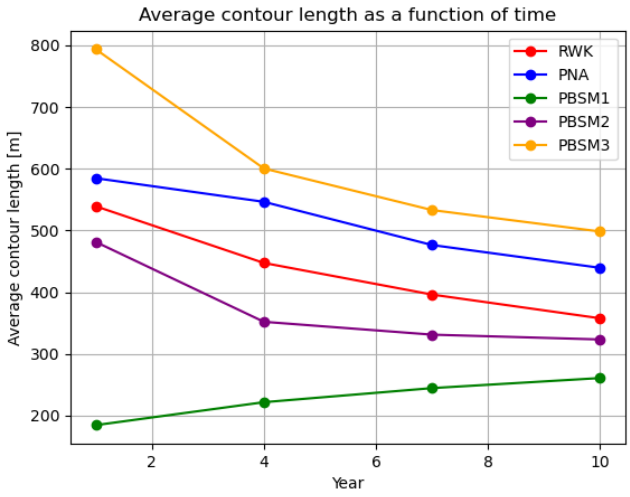

Figure 5.7: The evolution of contour length over time

Thermal plume contour length

To dive into the thermal plume distortion, the outer contour of the plume is extracted from the 3D temperature data with PyVista, generated in the simulation. For analyzing purposes, the contour is extracted for the temperature equals the dimensionless temperature defined in Equation 5.2 is 0.5. This is done to eliminate the temperature dependence of the contour. As the models created with the SGS algorithm, have a large spatial variability in permeability, and therefore contour length, the average is taken for the 16 directions in which the contour length is calculated. Figure 5.3a and Figure 5.2b are examples of surfaces created that are created with the same temperature threshold. Instead of taking the entire surface now a line segment along this surface is used.

$$T^* = \frac{T - T_{amb}}{T_{in} - T_{amb}} \tag{5.2}$$

Figure 5.8, the average contour length is plotted as a function of time. Note that the simulation contour lengths are averaged in a similar way as for the comparison between energy efficiency of homogeneous and heterogeneous simulations (Figure 5.1).

Figure 5.8 shows that the contour length decreases over the simulations, as the affected volume of the aquifer heats up through thermal conduction. In contrast, the contour length of PyBarSim1 increases over time, which is attributed to a buoyancy-driven flow distortion of the thermal plume. The largest changes in contour length are observed in the first years of simulation. When comparing Figure 5.8 and Figure 5.1, it can be found that if the contour length is long, the difference in energy efficiency is large for the first few cycles, which is in agreement with the findings of the previous section. This relation is further illustrated by Figure 5.8, where it can be seen that the longer the contour length, the greater the difference between the homogeneous simulation and the heterogeneous simulation. These figures also illustrate that the longer the contour length, the longer it takes for the energy efficiency of homogeneous and heterogeneous simulations to converge.

In Figure 3.4, the heterogeneity of the aquifer is characterized by calculating the coefficient of variation for the horizontal permeability. As discussed, the coefficient of variation describes how uneven the permeability is distributed, however it does not how the permeability is organized. In the previous section, it is found that the internal organisation of permeability matters for energy efficiency outcomes. That is the reason why the Coefficient of Variation is not able to describe the difference between homogeneous and heterogeneous simulations. In Figure 5.9 this is illustrated. Here, it becomes clear that the coefficient of variation can describe trends in models that are created via the same algorithm. Take, for example, the PyBarSim models (1, 2 and 3) that are similar in the sense that they are all more or less stratified, with a varying degree of permeability contrast between layers. Here, we see that the

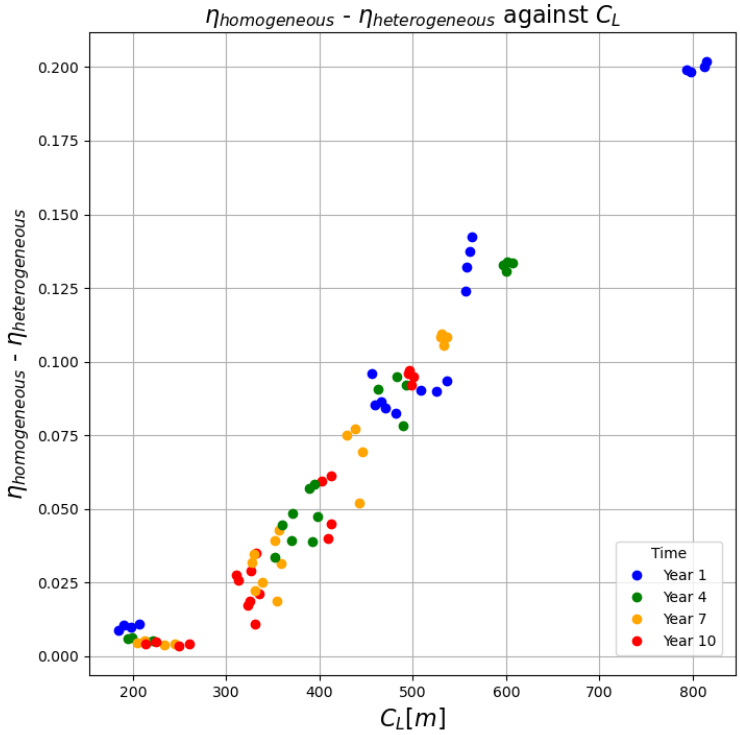

Figure 5.8: The difference in energy efficiency between a homogeneous simulation and its heterogeneous counterpart is plotted against the heterogeneous simulation's contour length. The colors used in the plot represents which year is used in subtracting the energy efficiency of the heterogeneous simulation from the homogeneous simulation.

sharper the contrasts, the higher the coefficient of variation. It can also be observed that the difference between homogeneous and heterogeneous simulations becomes larger as the coefficient of variation increases. The same can be concluded for the SGS models. Thus, for individual model types, the coefficient of variation is not a bad metric to assess heterogeneity. However, the coefficient of variation fails to provide a link between the heterogeneity of the aquifer and the energy efficiency.

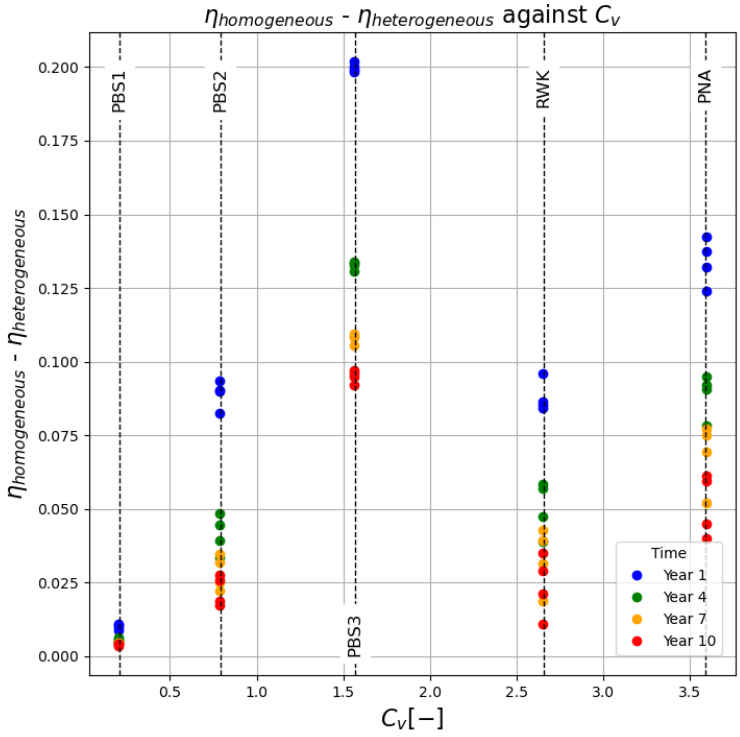

Figure 5.9: The difference in energy efficiency is plotted against the coefficient of variation of the heterogeneous geomodel. The colors used in the plot represents which year is used in subtracting the energy efficiency of the heterogeneous simulation from the homogeneous simulation.

5.1.2. Parameter sensitivity

The direct effect of variation of injection volume, injection temperature, and anisotropy ratio is examined for heterogeneous simulations. This is done by computing the difference between the average energy efficiency between identical pairs of simulations. Between the identical pairs only one parameter from, volume, injection temperature or anistropy ratio varies. As an example, to test the effect of anisotropy, the average energy efficiency PBS1, with an injection volume of 600.000 cubic meter per year, an injection temperature of 73 degrees Celsius and an anisotropy ratio of 2 is compared to the average energy efficiency PBS1, with an injection volume of 600.000 cubic meter per year, an injection temperature of 73 degrees Celsius and an anisotropy ratio of 5. Per variable, the influence is plotted against the statistical heterogeneity metrics.

Injection volume

First, the injection volumes are compared. This is done pairwise over the three injection volumes considered. For a change in injection volume from 200,000 to 600,000 cubic meters per year, the following statistics are obtained: the maximum difference is 12.99 percent, which is observed for PBS1, with an injection temperature of 90 degrees Celsius and an anisotropy ratio of 2. The minimum difference is 0.26 percent observed for PNA4 with an injection temperature of 73 degrees Celsius and an anisotropy ratio of 5. The average difference is 3.92 percent.

It can be seen from Figure 5.10 that the effect of volume change is reduced when geomodels have a higher coefficient of variation. This is because the models with the lower coefficient of variation (PBS1 for instance) are also the models that allow buoyancy flow to develop more, with the exception of PBS3. The driving force behind buoyancy flow, the density gradient between the injected and initial groundwater temperature in this pairwise comparison for both volumes. For larger volumes, the tilt of the thermal front occurs farther away from the well. Therefore, the cold water is further away from the well, which positively affects production temperatures. Thus smaller volumes are more effected by the buoyancy flow potential (Beernink et al., 2024). If buoyancy flow can be developed less due to heterogeneities, less tilting of the thermal front occurs, for which the impact is thus the largest on smaller volumes.

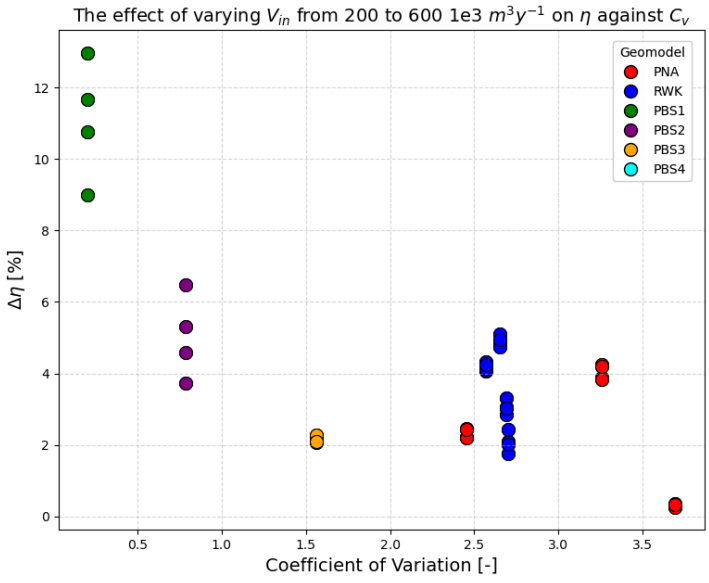

Figure 5.10: The effect of changing the injection volume from 200,000 to 600,000 cubic meters per year on mean energy efficiency.

Similar statistics are obtained for a change in injection volume from 600,000 to 1,000,000 cubic meters per year, namely a maximum difference in mean energy efficiency of 4.64 percent, minimum difference of 0.17 percent and an average difference of 1.72 percent. For this change in volume, the relation to the

coefficient of variation is not that obvious for the stochastic models (PNA and RWK), as can be seen in Figure 5.11. A possible explanation for this is that the larger volume spreads through the aquifer further. As these aquifers are based on correlated permeability values, through the SGS algorithm, the thermal plume might be more distorted. This distortion increases A/V and results in the observed differences in energy efficiency.

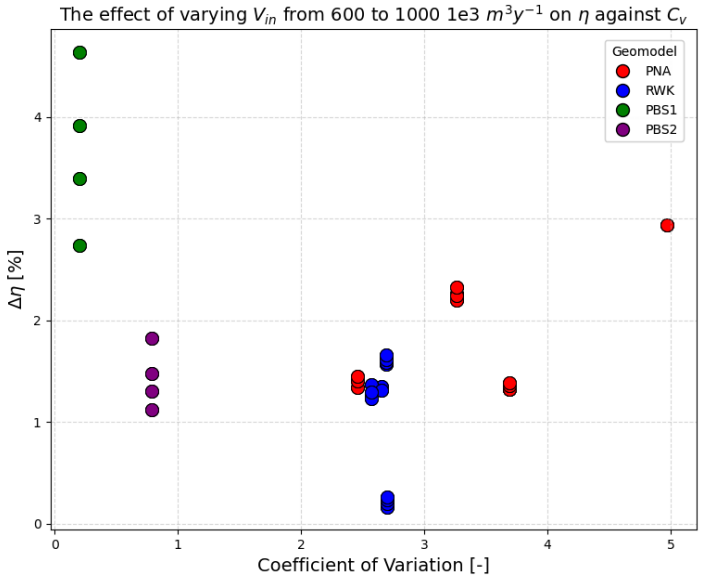

Figure 5.11: The effect of changing the injection volume from 600,000 to 1,000,000 cubic meters per year on mean energy efficiency.

Injection temperature

The difference in energy efficiency is computed between identical simulations with varying injection temperature. For all simulations, reducing the injection temperature resulted in a higher average energy efficiency. This is largely attributed to the fraction buoyancy-driven heat losses. An increase in injection temperature increases the density difference between the injected and extracted water, which drives the vertical motion. Where buoyancy flow is obstructed, this effect is reduced. The obstructions are caused by heterogeneity in the vertical permeability model. From that it seems quite logical that more energy efficiencies from simulations with more heterogeneous models are less sensitive to changes in injection temperature. A clear example of this is the PBS3 simulation. In Figure 3.4, it is discussed that the high permeable zones in this model are concentrated in thin part of the aquifer, which makes it highly unsuitable for buoyancy-driven flow to develop. The maximum observed difference when varying the injection temperature from 73 to 90 degrees Celsius in mean energy efficiency is 6.86 percent for PBS1 with the smallest injected volume and the lowest anisotropy ratio. The minimal observed difference is 0.41 percent and the mean difference is 1.14 percent.

Anisotropy ratio

The effect of varying the anistropy ratio between 2 and 5 on average energy efficiency can only be explained by a change in buoyancy flow potential. Its relation to the coefficient of variation is again quite clear for a similar reason as for the influence of injection temperature on average energy efficiency. The influence of the anisotropy ratio is maximally 3.20 for the PBS1 model with the smallest volume and the highest injection temperature. The smallest difference is observed for the PBS3 model with an injection volume of 600.000 and injection temperature of 73 degrees Celsius. The mean influence for all cases is 1.14 percent. Again, the influence of anisotropy decreases with increasing volumes and subsurface heterogeneity Figure 5.13.

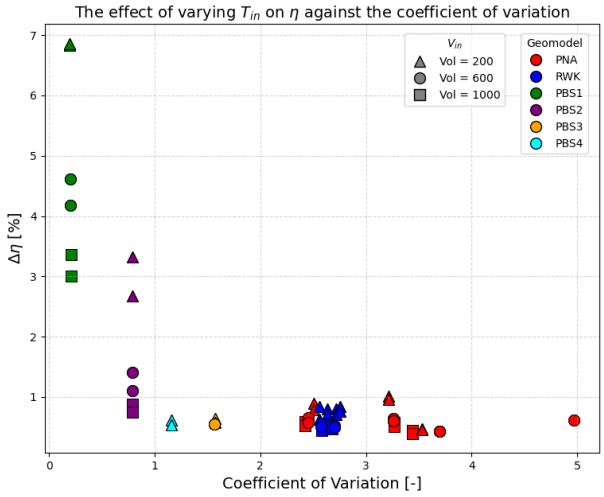

Figure 5.12: The effect of changing the injection temperature from 73 to 90 degrees Celsius on mean energy efficiency.

5.2. Thermal plume analysis

Knowing how far and in which direction the thermal plume will spread due to subsurface heterogeneity could improve overall (HT-)ATES well design and use of subsurface space. This is because (HT-)ATES can only be applied in a limited set of aquifers, since the viability of (HT-)ATES systems depends on depth and hydraulic conductivity (Bloemendal, 2018). Therefore, in areas with high energy demand, different (HT-)ATES systems could target the same aquifer. To give an example: in figure Figure 5.14 the theral plumes of LT-ATES systems present in the TU-Delft area are shown. Especially for LT-ATES systems, cold water is injected and extracted in a similar way to hot water for HT-ATES systems. The hot plume of an HT-ATES could interfere with the cold plume, reducing its yield. Because of this, subsurface spatial planning is required when multiple (HT-)ATES systems are targeting the same aquifer.

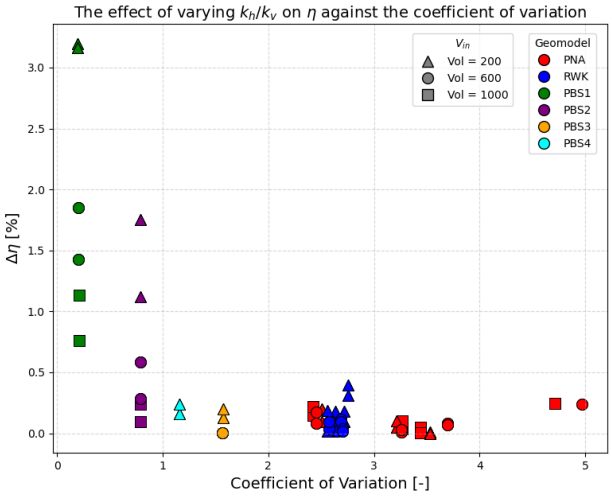

Figure 5.13: The effect of changing the anisotropy ratio from 2 to 5 on mean energy efficiency

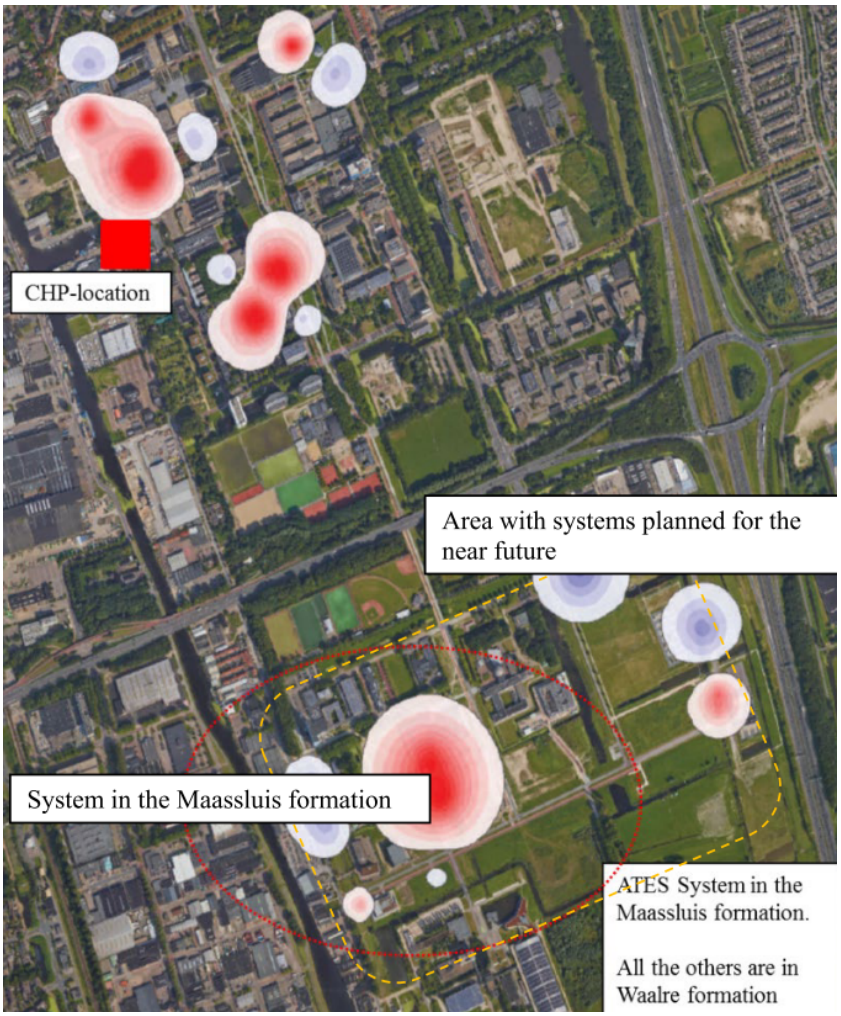

Figure 5.14: A map showing the area of Delft, on the thermal plume of exising LT-ATES systems are depicted, from Bloemendal, Phil Vardon, et al., 2020

In this section, the thermal plume is mapped on the basis of two temperature contours. The first threshold indicates where the water temperature reaches 25 degrees Celsius or more. The reason why this limit is chosen is that this is an important matter for HT-ATES permits in the Netherlands. This means knowing the extent is important for legislation purposes. In section E.1 all plume maps for the 25 degrees thresholds are shown. The maps are presented as density plots. The value of the density plot (between 0 and 1) indicates what vertical portion of the aquifer has a temperature above the threshold.

5.2.1. Controlling parameters on thermal plume spread

Geomodel type

Figure 5.15 shows the thermal plume spread of the PNA and RWK model. The RWK thermal plume appears to be much more circular than that of the PNA model. This applies to all situations depicted in subsection E.1.1. The variability of permeability plays an important role in this. In section 3.3, it is shown that all PNA models have a NG that is much lower than that of the RWK models. This results in a higher standard deviation in the permeability values than in the RWK models. For Figure 5.15a and Figure 5.15b, the logarithm of the standard deviation of the horizontal permeability is 2.2 and 1.5, respectively. The increased variability results in flow being focused through high permeable corridors, which elongates the thermal plume. The PNA mapview plots illustrate that with increasing variability the estimation of the thermal plume extent and direction is not possible.

The density plots for the PyBarSim model (Figure 5.16) show results that contrast with the SGS models. The randomness of the spread of the thermal plume has been eliminated due to the stratified organization of permeability the PBS geomodels. This holds for all PyBarSim results, as can seen in subsection E.1.3.

Correlation directions

In the construction of the stochastic geomodels maximum correlation angles for all lithologies, and therefore permeability, are derived. The maximum correlation angle is the direction for which the lithologies and hydraulic properties show the longest spatial continuation. It could be argued that it can be expected that the thermal plume would be elongated in the direction of maximum permeability, in other words, that the direction of maximum plume spread would alligned with the direction of the most permeable lithology.

Figure 5.15a and Figure 5.17 show, that this not is the case. In both figures the correlation angles are in the same direction, though the thermal plume spreads out in very different directions. In subsection E.1.1, the spread of the thermal plume is not aligned with any of the correlation directions for PNA and RWK. This indicates that with permeability variability this high, no reliable prediction on thermal plume spread can be made. However, it can be argued that the Figure 5.17 plume is more circular than in Figure 5.15a. The RWK models, with a high NG compared to the PNA illustrate this further, as the thermal plume spread becomes more circular.

For the PBSM models, no correlation directions are gained in the process of making the geomodel. Here, the strike and dip directions are used as indicative directions. This as wave-influenced deltaic deposits show the largest correlation parallel to the shore line, and the most variability perpendicular to that (Nichols, 2007). This is not well reflected in the thermal plume density plot. The plot shows a circular shape that points out towards the cold well, which is located on the center right, outside of the figure.

5.2.2. Implication heterogeneity on HT-ATES spatial design

Instead of focusing on the overall thermal radius of an HT-ATES system, calculated in Equation 4.4, it can be beneficial for estimating required distances between wells to calculate the maximum thermal radius. The method of calculation the maximal thermal radius is presented below.

In advance, volume coefficients V_c per reservoir layer are calculated from the 1D porosity and permeability data Equation 5.3. What part of the total injected water flows through a specific layer is proportional to the relative permeability (the permeability of a layer over the mean permeability of the aquifer) of the layer, as indicated in Equation 5.4 (modified from: (Fitts, 2013)). This is multiplied by the relative porosity, as more layers with more porosity can accommodate a larger water volume.

$$V_c(z) = \frac{k_h(z)}{\overline{k}_h} \cdot \frac{\phi(z)}{\overline{\phi}} \tag{5.3}$$

$$q_r = \frac{k_h}{\mu} \frac{\partial P}{\partial r} \tag{5.4}$$

The volume coefficients are normalized to volume fractions, V_f, so that the sum of all volume fractions is 1 (Equation 5.5). This ensures that the sum of a multiplication between the volume fractions and an injected volume returns this injected volume.

$$V_f(z) = \frac{V_c(z)}{\Sigma V_c(z)} \tag{5.5}$$

To calculate the change in water volume a layer has received for a given point in time, the injected water volume, named $V_{w,t}$ is multiplied with V_f. However, the water volume does not represent the thermal volume. To convert the water volume to thermal volume, $V_{Th,t}$, equation Equation 5.6 is used. Here, the volumetric heat capacity of the layer $C_{v,aq}$ is divided over the volumetric heat capacity C_w.

$$V_{Th,t}(z) = V_{w,t} \cdot V_f(z) \cdot \frac{C_{v,w}}{C_{v,aq}(z)} \tag{5.6}$$

Lastly, the rock volume is transformed to a thermal radius per layer with Equation 5.7. Note, that this approach represents calculating the thermal radius (Equation 4.4) per aquifer layer.

$$R_{Th}(z) = \sqrt{\frac{V_{Th}(z)}{\pi dh}} \tag{5.7}$$

From the density plots, it can be seen that the thermal plume spreads out much further than the thermal radius. Therefore, the maximum thermal radius might be useful to consider in subsurface spatial planning.

The results of the computation are shown in Figure 5.18. From each profile, the maximum R_{Th} can be derived. This approach does not take into account thermal conduction into the aquifer, the actual influence radius will be larger than the maximum thermal radius. It is proposed that the design criterion based, on thermal radius, should be multiplied with the maximum thermal radius divided by the overall thermal radius, to ensure that interference between wells is reduced as much as possible.

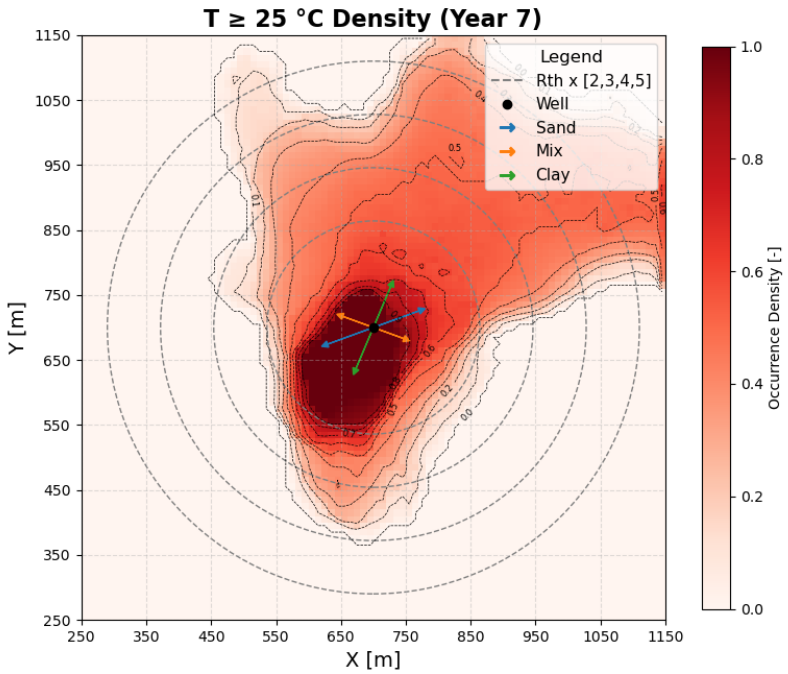

(a) The thermal density plot for PNA1, with an injection volume of 600,000 cubic meters per year in the seventh year.

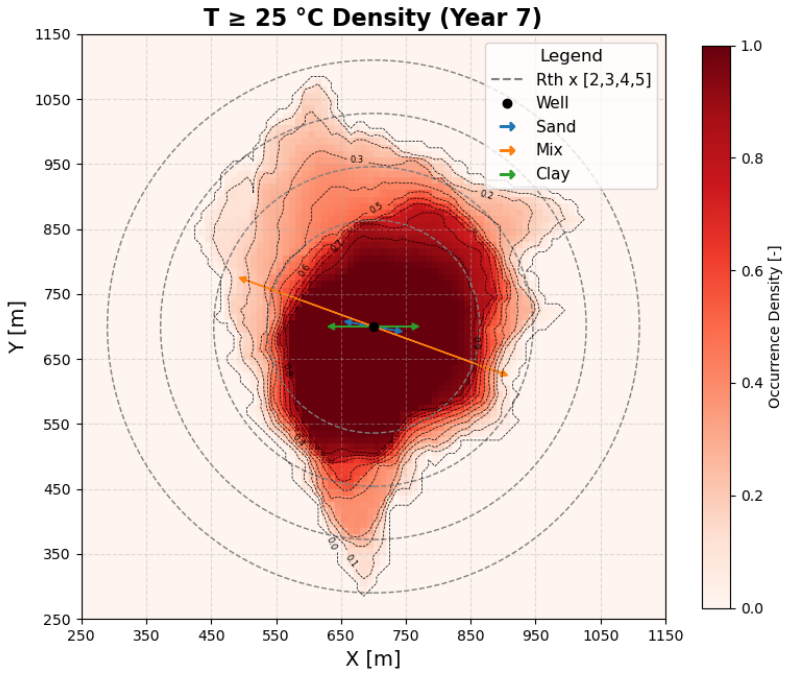

(b) The thermal density plot for RWK1, with an injection volume of 600,000 cubic meters per year in the seventh year.

Figure 5.15: The energy approximated efficiencies of the first year.

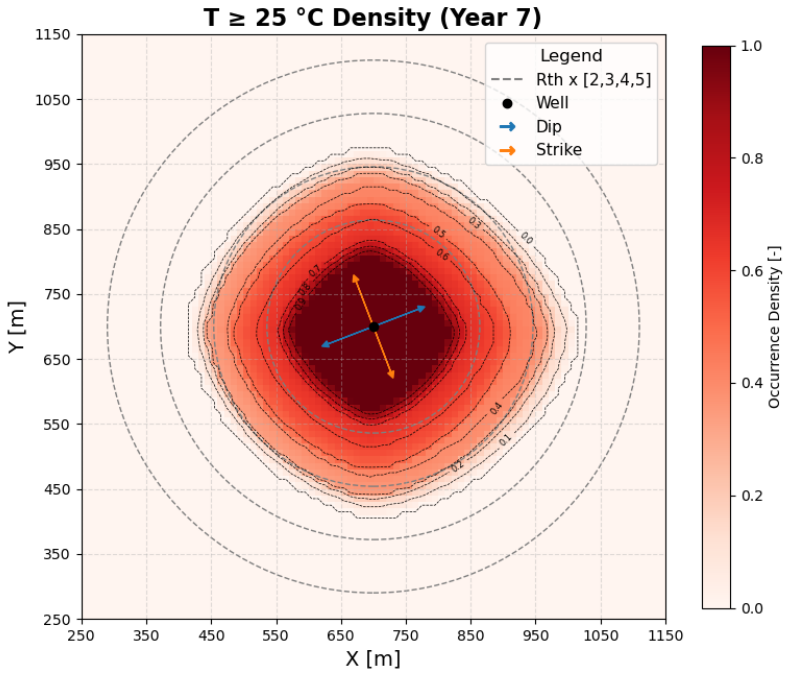

Figure 5.16: The thermal density plot for PBS2, with an injection volume of 600,000 cubic meters per year in the seventh year.

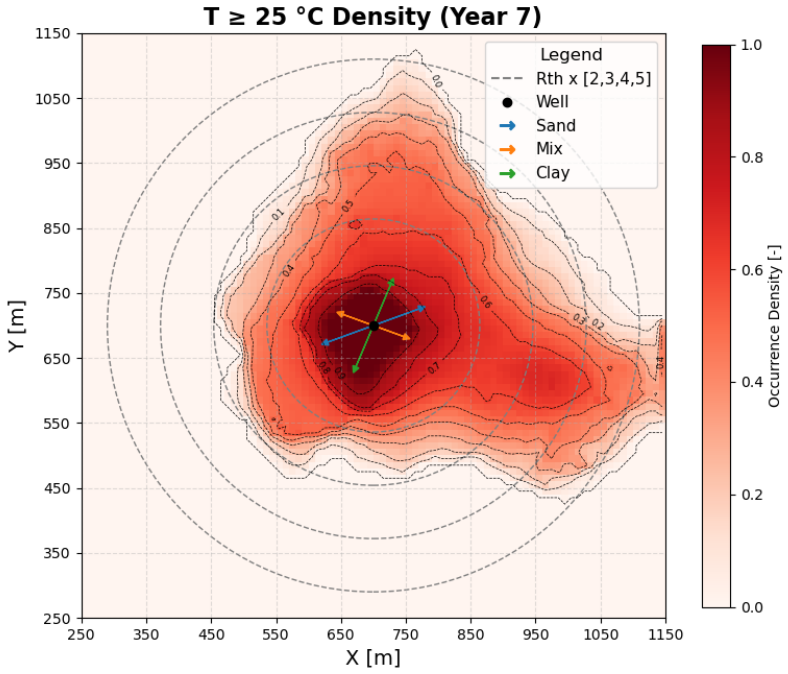

Figure 5.17: The thermal density plot for PNA3, with an injection volume of 600,000 cubic meters per year in the seventh year.

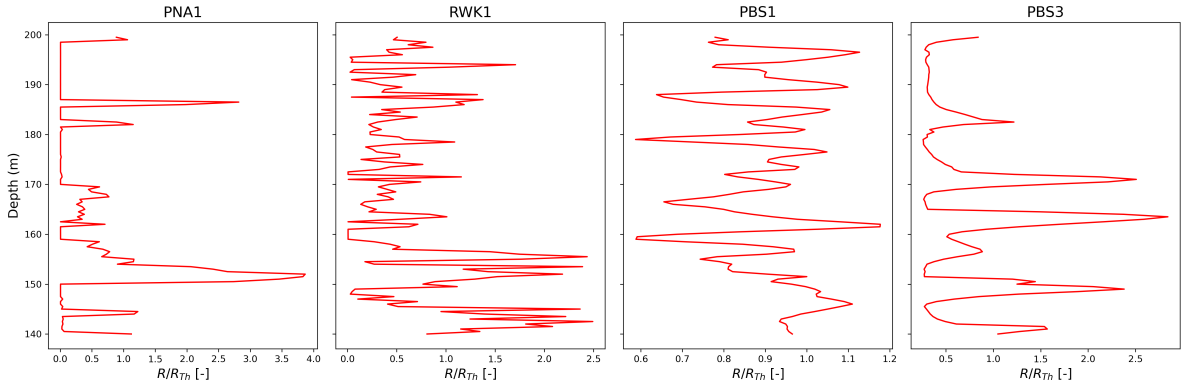

Figure 5.18: The results of calculating the thermal radius per segment. The radius is divided over the thermal raidus, to high light the difference between the maximum thermal radius and the overall thermal radius.

6

Discussion

In this thesis, the impact of subsurface heterogeneity on HT-ATES performance is addressed, in which the scope of the implementation of an HT-ATES system in the Maassluis formation for the TU-Delft is considered. The chapters in this work build onto each other. Decisions made in one part of the research often affected outcomes in subsequent chapters. Therefore, the discussion will start by evaluating the results of each chapter and putting them in perspective.

6.1. Geology

The goal of chapter 2 is to characterize the Maassluis formation and to identify key characteristics that have an effect on subsurface flow. The well correlations show an additional information compared to the existing geohydrological model of TNO. Though, new information is added, the findings in chapter 2 could be improved. Below, some reasons for mismatches between the interpretation of the architecture of the Maassluis and the actual subsurface are presented.

First, it is assumed that the entire Maassluis formation consists of marine sediments. In the study by Slupik et al. (2007) in which sediments from a well in Sea-Land (The Netherlands) are analyzed, the basal parts of the sequences within the Maassluis formation are interpreted as aeolian deposits. This interpretation is based on the presence of matted grain surfaces and a good sorting as a result of sediment transport by wind (Slupik et al., 2007). It should be noted that this well is located approximately 50 kilometers south-west of Delft. Reconstructions of the paleoshoreline, presented in Funnell (1996), show that Delft is located basin-inward with respect to the well in Sea-Land. This is supported by the Dutch shallow subsurface TNO model, which shows that the Maassluis formation is thicker and located deeper in Delft, than in Sealand (TNO – Geological Survey of the Netherlands, 2025). This could mean that the Delft area remained submerged through the Preatiglian and Tiglian, which does not allow the deposition of aeiolean sediments. In Funnell (1996) it is mentioned that this reconstruction is an approximation, so firm conclusions cannot be drawn solely on this basis. The sediments recovered from the DAP-GEO2 well could provide additional insights that rule out the presence of terrestrial sediment intervals.

Second, directly interpreting lithologies based on Gamma-Ray signals can be misleading, as was briefly mentioned in section 2.2. Organic material can be a source of radiation, which leads to a higher GR signal. Separation of GR signals in their radioactive components, K, Th, U, can differentiate between clay and organic matter (Pauw, Hernandez, and Doornenbal, 2022). However, gamma ray tool capable of this differentiation was only present for the DAP-GEO2 log. In addition to that, some minerals, such as glauconite, can also amplify GR signals by additional radiation (Pauw, Hernandez, and Doornenbal, 2022). These, amplifications of GR signals could lead to misinterpretation of clay content. While misinterpretation is possible, in the specific case of the Maassluis formation, the risk is limited, as the glauconite content is expected found to be low in Jansen et al. (2004).

Third, the conversion of GR to lithologies is for most of the wells based on interpretation by manually setting thresholds for the log signal. This could lead to a misinterpretation of lithology, affecting the

lithology proportions in the stochastic geomodels. However, since these geomodels already span a range of lithology proportions, the overall uncertainty is likely captured.

Lastly, features that are smaller than approximately 0.5 meter in thickness are not incorporated in the lithostratigraphic interpretation. With a possible feature being clay drapes that could be the result of tidal influences in the SNSB (Nichols, 2007). The sub meter scale features have been incorporated for an LT-ATES system simulation by Possemiers, Huysmans, and Batelaan (2015), where they showed to reduce the energy efficiency of the system by 3.3 to 3.6 percent. Such features, if present in the Maassluis formation, could reduce vertical permeability and thus decrease the sensitivity of HT-ATES performance operational parameters.

6.2. Geomodeling

Two ways of representing subsurface heterogeneity have been presented, namely stochastic modeling and process-based modeling. Process-based geomodels have not been used for HT-ATES simulations to this authors knowlegdge. Therefore insights from this study are novel, and lead to an overall better understanding of HT-ATES systems.

Process-based models are likely to produce more realistic subsurface structures than stochastic models. In the stochastic models sharp transitions between contrasting lithologies are present, which may artificially enhance preferential flow pathways. These sharp transitions are not supported by well-log evidence, as the changes in the well log singals of the Maassluis formation are often gradual.

That the process-based model is likely to be more accurate, makes up for the fact that the process-based model does not honor the well data, as is achieved in stochastic geomodeling. Due to the more accurate subsurface structures of the process-based model, the simulation results that used the process-based model will likely represent how an actual HT-ATES system in deltaic deposits would behave. When carrying out feasibility studies, it is recommended to implement a modeling strategy that represents geology in the best way possible.

Although it is argued that the forward stratigraphic models likely represent the subsurface better than stochastic models, the results of simulation with stochastic geomodels provide valuable insights. Relationships between energy efficiency and heterogeneity, observed in both model types can be considered model-independent, which suggests that these findings may apply beyond deltaic aquifers, if hydraulic properties and operational parameters are in a similar range.

A major cause of uncertainty in the simulation results is the permeability used. First, an empirical relationship is used for forward stratigraphic models to translate grain size into permeability. Actual permeability values of the Maassluis formation might deviate from the values used in this study. However, the resulting permeability of the PBSM1, PBSM2, and PBSM3 geomodels falls within the range of measurements on the Maassluis formation of NLOG and in the study by Barlet ((NLOG, n.d.) and (Barlet, 2025)). By using multiple forward stratigraphic models, all with different permeabilities, a range of simulated outcomes is obtained. By doing so the uncertainty in permeability is translated to a range of possible energy efficiencies. Second, in both geomodel types, a homogeneous anisotropy ratio across the entire domain is used. The anisotropy might be lithology dependent. This could cause discrepancies between the simulation and actual behavior of HT-ATES systems, as for instance, buyoancy flow might be limited or enhanced. Barlet (2025) found a range of anistorpy ratios for the Maassluis formation, hinting that a uniform anisotropy ratio might not be accurate. Though the two observed anisotropy ratios where in a close range, namely 1.44 and 3.26. As this range is small and the influence of anisotropy on energy efficiency is limited, the assumption of a uniform anisotropy ratio might is valid.

6.2.1. Simulation set-up

To save computation time a spatial grid with varying grid cells is created, where the fine grid cells are in a domain around the hot well. Only in this region are the aquifer properties heterogeneous, outside of this region the aquifer is homogeneous. The choice of filling the distal cells with homogeneous properties, affects simulation outcomes. Though from the map-view plots of the thermal plume spread in chapter 5, it is observed that especially in the first years of simulation, This simplification likely had limited impact for most scenarios, since the thermal plumes remained within the fine-gridded domain

during the early years. However, in low NG aquifers (PNA models), the plume extended beyond the heterogeneous zone. In these cases, the transition from a homogeneous to heterogeneous grid may have affected preferential flow paths, reducing the accuracy of energy efficiency predictions and thermal plume spread. Potential blocks in fluid path ways could have resulted in a better thermal plume containment.

The temperature range tested in this study is relatively narrow. In HT-ATES systems injection temperatures are considered in a range between 45 and 90 degrees Celsius. The tested 90 and 73 degrees are both in the upper region of this interval. In future research, it could be meaning full to test lower temperatures, because buoyancy-driven flow would be substantially reduced. Comparing the differences between simulation outcomes with low temperatures and high temperatures would allow for the quantification of buoyancy-related heat losses and separately conduction losses under heterogeneous conditions.

The only one injection volume is used for the homogeneous reference cases limits the comparison between heterogeneous and homogeneous reservoirs. Since injection volume is of great influence on the energy efficiency, the use of one injection volume limits the ability to extend the observed relationships between homogeneous and heterogeneous to a broader range of scenarios. This educes the strength of generalizable design recommendations for HT-ATES implementation. The reason for choosing the 600.000 as reference volume, was that his volume is closest to what is considered for the desired HT-ATES system at the TU-Delft.

6.3. Simulation outcomes

From the simulation results, it is clear that homogeneous cases outperform heterogeneous cases. It is observed that the difference between homogeneous and heterogeneous cases becomes smaller when the heterogeneous medium becomes more homogeneous, which was explained by looking into the contour length. Instead of comparing energy efficiency with contour length, it could be more informative to compare energy efficiency with the surface area over volume ratio. In this way, the average of the contour lengths does not need to be taken over multiple directions. As the permeability distribution of the stochastic models varied along these directions, taking the average of the length might not be representative for the entire thermal plume.

The simulation time in this study is 10 years in which the energy efficiencies of homogeneous and heterogeneous simulations converge. It is also found that the difference in long term energy between homogeneous and heterogeneous simulations depends on the surface area to volume ratio, but mostly on the potential to develop buoyancy flow. By extending the simulations, it is possible that a simulation that has low permeable horizontal intervals, like the PBSM model, combined with a high net-to-gross ratio, could outperform its homogeneous counterpart. However, this would apply to a very limited range of aquifers as the combination of heterogeneity orientation and vertical permeability needs to be alligned.

Heldt, Beyer, and Bauer (2024), which performed a parameter sensitivity analysis of HT-ATES systems under homogeneous subsurface conditions, stated that vertical permeability is a major parameter in controlling energy efficiency. In this study, it is found that vertical conductivity is ranked as having the lowest influence on recovery efficiency compared to injection volume and temperature. This result is not unexpected, as heterogeneity already reduces vertical permeability. This observation is supported by looking at the relation between heterogeneity metrics and the difference in energy efficiency of identical simulations with varying vertical permeability.

Based on the preceding paragraph, it is not surprising that the influence of injection is larger than the influence of vertical permeability. This is because a higher injection temperature reduces the energy efficiency in two ways: by increasing conduction losses and by increasing buoyancy flow. As determined above, buoyancy flow is already limited by heterogeneity, which reduces this effect. In contrast, heterogeneity increases conductive losses by enlarging the surface area of the plume. Having the anisotropy ratio as least important parameter, is in contrast to findings in (Heldt, Beyer, and Bauer, 2024) and (Barlet, 2025).

7

Conclusions

This thesis presents an integrated workflow for assessing HT-ATES performance under heterogeneous conditions, where insigths from geology formed the basis for constructing multiple geomodels that are then used in numerical HT-ATES simulations.

In this study, the Maassluis formation in the Netherlands is considered for the implementation of an HT-ATES system. The Maassluis formation is a deltaic deposit that was deposited in an era with fluctuating sea levels due to glaciations. This leads to the intercalation of fine- and coarse-grained deposits. The correlations of the well data in the region of interest show that the continuity of the clay layers is strongly dependent on the correlation strategy. A sequence stratigraphic correlation highlighted multiple dipping, continuous clay layers, whereas the lithostratigrahic correlation showed a horizontal clay layer combined with isolated patches of clay in the aquifer of interest. The use of well high-resolution well data adds levels of detail to existing models, homogeneous models, which is encouraged to implement when trying to predict realistic results for HT-ATES performance.

Based on well-data correlations, two geomodeling techniques have been implemented, namely stochastic modeling and process-based modeling. Stochastic modeling honors the well data and proportions, though it disregards the geological processes that shape the deposits. Process-based incorporates the process behind deposition and is therefore likely a better representation of the subsurface. Both geomodeling strategies result in a distinct organization of preferential flow patterns. By implementing multiple geomodeling strategies, a wider range of outcomes is observed, and the trends with respect to the relation between subsurface heterogeneity and HT-ATES performance are identified.

The heterogeneity in the geomodels has a negative impact on the simulated energy efficiency, which is most pronounced in the first years of simulation, where differences of 1 to 20 percent are observed. Here, distribution of permeability, which causes the distortion of the thermal plume is identified as the main reason behind this. The more distorted the thermal plume is, the larger the heat losses through thermal conduction in the first years, compared to homogeneous cases.

The role of heterogeneity reduces over time, as energy efficiencies of homogeneous and heterogeneous simulations converge. The resulting differences in energy efficiency in the last year are 0.4 to 9.5 percent, depending on the geomodel used for simulation. Furthermore, heterogeneous simulations show steeper increase in energy efficiency for all simulated years, which causes these differences to become even smaller. For simulation time periods longer, than the 10 years considered in this study, the role of heterogeneity is likely to reduce even further.

However, heterogeneity in the permeability model cause vertical flow barriers. These barriers are effective in control the long-term energy efficiency, as buoyancy-driven heat losses have a major influence on. Simulations where buoyancy flow is allowed to develop strongly show the projected long term energy efficiency. Therefore estimating how effective the heterogeneity is on limiting buoyancy-driven flow key in estimating long term energy efficiency.

Models with stratified heterogeneity and models where the proportions of impermeable material are

low show a predictable thermal plume spread. For heterogeneous media with a high proportion of impermeable material, the thermal plume spread becomes unpredictable. As subsurface flow is concentrated through, high permeable layers, the maximum thermal radius per layer should be considered in subsurface spatial planning.

To conclude, the effect of heterogeneity on HT-ATES performance, remains challenging to predict on beforehand and depends on an interplay between buoyancy driven flow and surface area to volume ratio.

References

Akın, Taylan, David Bruhn, and Alexandros Daniilidis (2025). *Predictive Modeling of Heat Storage in TU DELFT Campus*.

Bariloche, Fundación (2024). *SCIENCE AND ACADEMIA AEE-Institute for Sustainable Technologies (AEE-INTEC) Council on Energy, Environment and Water (CEEW)*. Tech. rep.

Barlet, Luis (2025). *The Impact of varying thermal and hydraulic properties on HT-ATES systems A Study Based on Sediments of the Maassluis Formation with a focus on thermal properties AESM7000: Master Thesis*. Tech. rep. URL: http://repository.tudelft.nl/..

Beernink, Stijn et al. (Feb. 2024). "Heat losses in ATES systems: The impact of processes, storage geometry and temperature". In: *Geothermics* 117. ISSN: 03756505. DOI: 10.1016/j.geothermics.2023.102889.

Berends, Constantijn J., Bas De Boer, and Roderik S.W. Van De Wal (Feb. 2021). "Reconstructing the evolution of ice sheets, sea level, and atmospheric CO2during the past 3.6 million years". In: *Climate of the Past* 17 (1), pp. 361–377. ISSN: 18149332. DOI: 10.5194/cp-17-361-2021.

Bloemendal, Martin (May 2018). "The hidden side of cities". PhD thesis.

Bloemendal, Martin and Stijn Beernink (Jan. 2023). *HT-ATES feasibility for TRIAS Westland case study*. Tech. rep. KWR.

Bloemendal, Martin and Niels Hartog (Oct. 2017). "Analysis of the impact of storage conditions on the thermal recovery efficiency of low-temperature ATES systems". In: *Geothermics* 71, pp. 306–3019. DOI: 10.1016/j.geothermics.2017.10.009.

— (Jan. 2018). "Analysis of the impact of storage conditions on the thermal recovery efficiency of low-temperature ATES systems". In: *Geothermics* 71, pp. 306–319. ISSN: 03756505. DOI: 10.1016/j.geothermics.2017.10.009.

Bloemendal, Martin, Phil Vardon, et al. (2020). *HT-ATES at the TU Delft campus*. Tech. rep. TU-Delft and ENGIE.

Cano, A. Cuesta et al. (2023). "Use of forward stratigraphic modelling for the detection of sub-seismic scale heterogeneities in shallow marine environments". In: *84th EAGE Annual Conference and Exhibition*. Vol. 2. European Association of Geoscientists and Engineers, EAGE, pp. 1504–1508. ISBN: 9781713884156. DOI: 10.3997/2214-4609.202310486.

Catuneanu, Octavian (2022). "Principles of Sequence Stratigraphy". In: Elsevier. DOI: 10.1016/b978-0-444-53353-1.00010-9.

Chen, Yuan, Denis Voskov, and Alexandros Daniilidis (Apr. 2025). "Rigorous Numerical Methodology and Heat Recovery Analysis for Modeling of Direct Use Geothermal Systems". In: *Geoenergy Science and Engineering* 247. ISSN: 29498910. DOI: 10.1016/j.geoen.2025.213661.

Collignon, Marine et al. (2020). "Evaluating thermal losses and storage capacity in high-temperature aquifer thermal energy storage (HT-ATES) systems with well operating limits: insights from a study-case in the Greater Geneva Basin, Switzerland". In: 85. DOI: 10.1016/j.geothermics.2019.101773ï. URL: https://insu.hal.science/insu-03227510v1.

Daniilidis, Alexandros et al. (June 2022). "Techno-economic assessment and operational CO2 emissions of High-Temperature Aquifer Thermal Energy Storage (HT-ATES) using demand-driven and subsurface-constrained dimensioning". In: *Energy* 249. ISSN: 03605442. DOI: 10.1016/j.energy.2022.123682.

Deutsch, C V and A G Journel (1997). *GSLIB: Geostatistical Software Library and User's Guide Second Edition*. Tech. rep.

Díaz-Curiel, Jesús et al. (2024). "On the Influence of Grain Size Compared with Other Internal Factors Affecting the Permeability of Granular Porous Media: Redefining the Permeability Units". In: *Lithosphere* 2024 (1). ISSN: 19474253. DOI: 10.2113/2024/LITHOSPHERE_2023_231.

DINOloket (2025). *Upper North Sea Group – Stratigraphic Nomenclature*. https://www.dinoloket.nl/en/stratigraphic-nomenclature/upper-north-sea-group. Accessed: 2025-05-01.

Fitts, Charles R. (2013). “3 - Principles of Flow”. In: *Groundwater Science (Second Edition)*. Ed. by Charles R. Fitts. Second Edition. Boston: Academic Press, pp. 47–96. ISBN: 978-0-12-384705-8. DOI: https://doi.org/10.1016/B978-0-12-384705-8.00003-0. URL: https://www.sciencedirect.com/science/article/pii/B9780123847058000030.

Fleuchaus, Paul et al. (Nov. 2020). “Risk analysis of High-Temperature Aquifer Thermal Energy Storage (HT-ATES)”. In: *Renewable and Sustainable Energy Reviews* 133. ISSN: 18790690. DOI: 10.1016/j.rser.2020.110153.

Funnell, Brian M (1996). *PLIO-PLEISTOCENE PALAEOGEOGRAPHY OF THE SOUTHERN NORTH SEA BASIN (3.75-0.60 Ma)*. Tech. rep., pp. 391–405.

Gao, H. et al. (Nov. 2024). “Estimation of Recovery Efficiency in High-Temperature Aquifer Thermal Energy Storage Considering Buoyancy Flow”. In: *Water Resources Research* 60 (11). ISSN: 19447973. DOI: 10.1029/2024WR037491.

Geerts, David et al. (Dec. 2025). “Analytically estimating the efficiency of high temperature aquifer thermal energy storage”. In: *Geothermal Energy* 13 (1). ISSN: 21959706. DOI: 10.1186/s40517-025-00343-8.

Heldt, Stefan, Christof Beyer, and Sebastian Bauer (Sept. 2024). “Uncertainty assessment of thermal recovery and subsurface temperature changes induced by high-temperature aquifer thermal energy storage (HT-ATES): A case study”. In: *Geothermics* 122. ISSN: 03756505. DOI: 10.1016/j.geothermics.2024.103086.

Heldt, Stefan, Bo Wang, et al. (June 2021). “Numerical investigation of a high temperature heat injection test”. In: *Journal of Hydrology* 597. ISSN: 00221694. DOI: 10.1016/j.jhydrol.2021.126229.

Houben, A et al. (2023). *Data inventory for the improvement of Upper North Sea group geological models*. Tech. rep.

Inpassing HTO Rotterdam Nesselande door Uitvoeringsteam WarmingUP (Deltares, Eneco) (n.d.). Tech. rep.

Jansen, H. S.M. et al. (2004). “The geometry and stratigraphic position of the Maassluis Formation (western Netherlands and southeastern North Sea)”. In: *Geologie en Mijnbouw/Netherlands Journal of Geosciences* 83 (2), pp. 93–100. ISSN: 00167746. DOI: 10.1017/s0016774600020060.

Khait, Mark and Denis V. Voskov (Aug. 2017). “Operator-based linearization for general purpose reservoir simulation”. In: *Journal of Petroleum Science and Engineering* 157, pp. 990–998. ISSN: 09204105. DOI: 10.1016/j.petrol.2017.08.009.

Kuhlmann, G. et al. (2006). “Integrated chronostratigraphy of the Pliocene-Pleistocene interval and its relation to the regional stratigraphical stages in the southern North Sea region”. In: *Geologie en Mijnbouw/Netherlands Journal of Geosciences* 85 (1), pp. 19–35. ISSN: 00167746. DOI: 10.1017/S0016774600021405.

Lake, Larry and Jerry Jensen (Jan. 1991). “A Review of Heterogeneity Measures Used in Reservoir Characterization”. In: *In Situ* 15, pp. 409–439.

Nichols, Gary (2007). *Sedimentology and Stratigraphy*. 2nd. Oxford, UK: Wiley-Blackwell. ISBN: 978-1-4051-3592-4.

NLOG (2025a). *Datacenter – Borehole Overview*. https://www.nlog.nl/datacenter/brh-overview. Accessed: 2025-05-01.

— (2025b). *Datacenter – Seismiek*. https://www.nlog.nl/datacenter/smc-lines. Accessed: 2025-05-01.

— (n.d.). *Boringen*. https://www.nlog.nl/boringen.

Patruno, Stefano, Gary J. Hampson, and Christopher A.L. Jackson (Mar. 2015). *Quantitative characterisation of deltaic and subaqueous clinoforms*. DOI: 10.1016/j.earscirev.2015.01.004.

Pauw, Pieter, Edwin Obando Hernandez, and Pieter Doornenbal (Oct. 2022). *Geophysical logging DAPGEO-02-500m, Delftse Hout*. Tech. rep. Deltaris.

Possemiers, Mathias, Marijke Huysmans, and Okke Batelaan (Aug. 2015). “Application of multiple-point geostatistics to simulate the effect of small-scale aquifer heterogeneity on the efficiency of aquifer thermal energy storage”. In: *Hydrogeology Journal* 23 (5), pp. 971–981. ISSN: 14350157. DOI: 10.1007/s10040-015-1244-3.

Possemiers, Mathias, K U Leuven, et al. (Jan. 2012). “Relationship between sedimentary features and permeability at different scales in the Brussels Sands”. In: *Geologica Belgica*. URL: https://www.researchgate.net/publication/259369343.

Schout, Gilian et al. (2014). “Analysis of recovery efficiency in high-temperature aquifer thermal energy storage: A Rayleigh-based method”. In: *Hydrogeology Journal* 22 (1), pp. 281–291. ISSN: 14350157. DOI: 10.1007/s10040-013-1050-8.

Sheldon, Heather A., Andy Wilkins, and Christopher P. Green (Nov. 2021). “Recovery efficiency in high-temperature aquifer thermal energy storage systems”. In: *Geothermics* 96. ISSN: 03756505. DOI: 10.1016/j.geothermics.2021.102173.

Shepherd, Russell G. (1989). “Correlations of Permeability and Grain Size”. In: *Groundwater* 27 (5), pp. 633–638. ISSN: 17456584. DOI: 10.1111/j.1745-6584.1989.tb00476.x.

Slupik, A. A. et al. (2007). “The stratigraphy of the Neogene-Quaternary succession in the southwest Netherlands from the Schelphoek borehole (42G4-11/42G0022) - A sequence-stratigraphic approach”. In: *Geologie en Mijnbouw/Netherlands Journal of Geosciences* 86 (4), pp. 317–332. ISSN: 00167746. DOI: 10.1017/S0016774600023556.

Sommer, Wijb et al. (Dec. 2013). “The impact of aquifer heterogeneity on the performance of aquifer thermal energy storage”. In: *Water Resources Research* 49 (12), pp. 8128–8138. ISSN: 00431397. DOI: 10.1002/2013WR013677.

Storms, Joep E.A. et al. (2002). “Process-response modeling of wave-dominated coastal systems: Simulating evolution and stratigraphy on geological timescales”. In: *Journal of Sedimentary Research* 72 (2), pp. 226–239. ISSN: 15271404. DOI: 10.1306/052501720226.

Tang, D. W.S. and S. E.A.T.M. Van Der Zee (Feb. 2022). “Macrodispersion and Recovery of Solutes and Heat in Heterogeneous Aquifers”. In: *Water Resources Research* 58 (2). ISSN: 19447973. DOI: 10.1029/2021WR030920.

TNO – Geological Survey of the Netherlands (2025). *Subsurface Models Map*. https://www.dinoloket.nl/ondergrondmodellen/kaart. Accessed: 2025-05-01.

TNO Geologische Dienst Nederland (2025). *DINOloket – Ondergrondgegevens*. https://www.dinoloket.nl/ondergrondgegevens. Accessed: 2025-05-01.

Tzoufka, Kalliopi et al. (Dec. 2024). “Physics-based numerical evaluation of High-Temperature Aquifer Thermal Energy Storage (HT-ATES) in the Upper Jurassic reservoir of the German Molasse Basin”. In: *Advances in Geosciences* 65, pp. 103–111. ISSN: 16807359. DOI: 10.5194/adgeo-65-103-2024.

Vardon, P. et al. (Nov. 2022). *Geothermal Project on TU Delft Campus - DAPGEO-02 Initial Borehole Dataset*. TU Delft - 4TU.ResearchData. Accessed via https://doi.org/10.4121/20299644. DOI: 10.4121/20299644.

Veen, Johan H. ten et al., eds. (2025). *Geology of the Netherlands: Second Edition*. Amsterdam: Amsterdam University Press. ISBN: 9789463728362. DOI: 10.1515/9789048554973. URL: https://www.degruyter.com/document/doi/10.1515/9789048554973/html.

Voskov, Denis et al. (2024). *A research and production geothermal project on the TU Delft campus: initial modeling and establishment of a digital twin*. Tech. rep. URL: https://bitbucket.org/.

Wang, Yang, Denis Voskov, Alexandros Daniilidis, et al. (Nov. 2023). “Uncertainty quantification in a heterogeneous fluvial sandstone reservoir using GPU-based Monte Carlo simulation”. In: *Geothermics* 114. ISSN: 03756505. DOI: 10.1016/j.geothermics.2023.102773.

Wang, Yang, Denis Voskov, Mark Khait, et al. (Apr. 2020). “An efficient numerical simulator for geothermal simulation: A benchmark study”. In: *Applied Energy* 264. ISSN: 03062619. DOI: 10.1016/j.apenergy.2020.114693.

Westerhoff, Wim (2009). “Stratigraphy and sedimentary evolution. The lower Rhine-Meuse system during the late Pliocene and Early Pleistocene”. In: DOI: 10.13140/RG.2.1.2038.2561. URL: https://www.researchgate.net/publication/280931343.

Winterleitner, G. et al. (July 2018). “The Impact of Reservoir Heterogeneities on High-Temperature Aquifer Thermal Energy Storage Systems. A Case Study from Northern Oman.” In: *Geothermics* 74, pp. 150–162. ISSN: 03756505. DOI: 10.1016/j.geothermics.2018.02.005.

Zhang, Yao and Radoslaw L. Michalowski (July 2015). “Thermal-Hydro-Mechanical Analysis of Frost Heave and Thaw Settlement”. In: *Journal of Geotechnical and Geoenvironmental Engineering* 141 (7). ISSN: 1090-0241. DOI: 10.1061/(asce)gt.1943-5606.0001305.

A

Well data overview

Name	X [m]	Y [m]	Top depth [m]	Bottom depth [m]	Tool	Figure	Source
B30G0935	82150	450480	0	431	GR	Figure B.1	TNO TNO Geologische Dienst Nederland, 2025
B30G0970	81213	452467	0	253	GR	Figure B.2	TNO TNO Geologische Dienst Nederland, 2025
B30G7773	80870	452950	0	257	GR	Figure B.3	TNO TNO Geologische Dienst Nederland, 2025
B30G7867	83064	453807	4	253	GR	Figure B.4	TNO TNO Geologische Dienst Nederland, 2025
B37E0481	83130	448250	3	200	GR	Figure B.5	TNO TNO Geologische Dienst Nederland, 2025
B37E0483	83100	448270	25	190	GR	Figure B.6	TNO TNO Geologische Dienst Nederland, 2025
B37E6785	85833	449052	10	205	GR	Figure B.7	TNO TNO Geologische Dienst Nederland, 2025
DAP-GEO2	85100	446163	0	500	GR	Figure B.8	TU-Delft P. Vardon et al., 2022
DEL-03	84248	446176	151	705	SP	Figure B.9	NLOG NLOG, 2025a
DEL-07	85076	446483	156	1000	GR	Figure B.10	NLOG NLOG, 2025a
DEL-08	85487	445771	22	1700	GR	Figure B.11	NLOG NLOG, 2025a
PNA-03	86902	449307	50	600	SP	Figure B.12	NLOG NLOG, 2025a
PNA-04S2	86111	449538	0	600	GR	Figure B.13	NLOG NLOG, 2025a
PNA-05	86789	449725	60	800	SP	Figure B.14	NLOG NLOG, 2025a
PNA-11	85913	450095	110	600	SP	Figure B.15	NLOG NLOG, 2025a
PNA-12	86703	449181	55	1900	GR	Figure B.16	NLOG NLOG, 2025a
PNA-GT01	88757	448527	60	1000	GR	Figure B.17	NLOG NLOG, 2025a
PNA-GT04	88619	447064	0	3000	GR	Figure B.18	NLOG NLOG, 2025a
PNA-GT05	88785	448492	130	930	GR	Figure B.19	NLOG NLOG, 2025a
PNA-GT06	88782	448498	130	900	GR	Figure B.20	NLOG NLOG, 2025a
RWK-01	81065	449085	0	190	GR	Figure B.21	NLOG NLOG, 2025a
RWK-04	80809	449715	36	510	SP	Figure B.22	NLOG NLOG, 2025a
RWK-16S1	81587	448766	31	449	GR	Figure B.23	NLOG NLOG, 2025a
RWK-18S1	80846	449092	0	1800	GR	Figure B.24	NLOG NLOG, 2025a

Table A.1: An overview of the well data used in this study. The columns contain: the name indicated by TNO-GDN or NLog, the position in the Dutch coordinate system, top and bottom depth of the well log, the data type that is used in the interpretation (GR or SP), the well log image, and the source where the well data can be found.

B

GR, SP and lithology logs

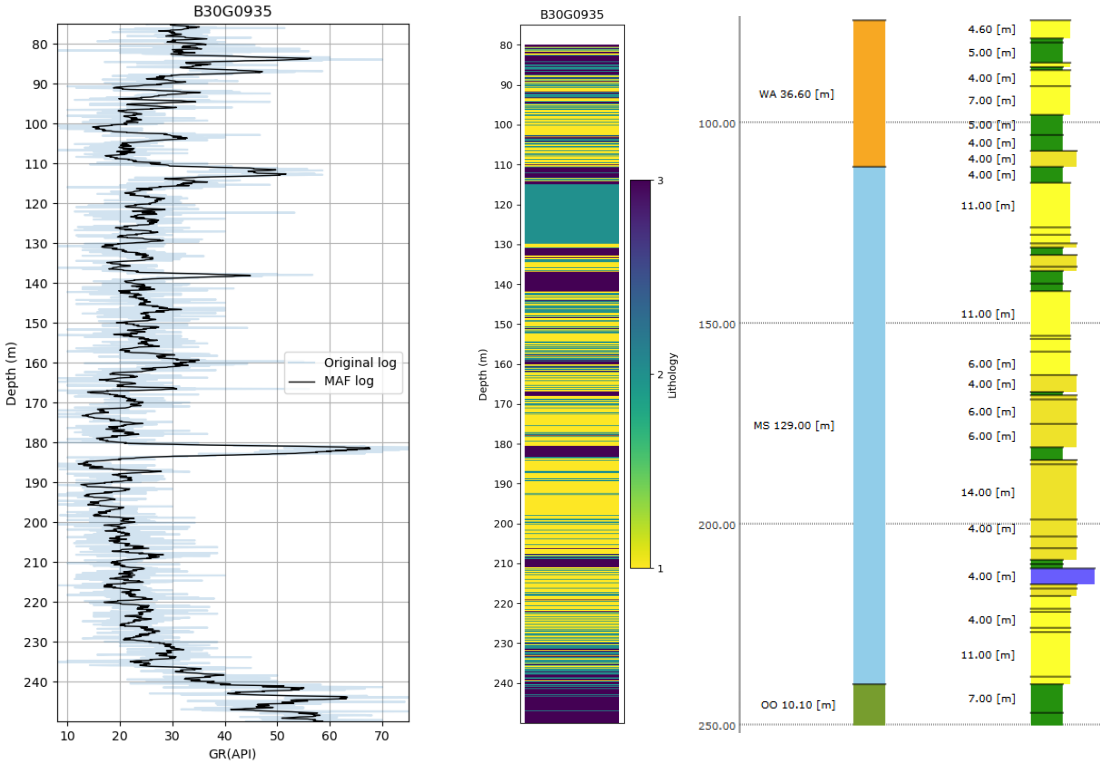

(a) The original GR-log in blue and the GR-log with a Moving Average Filter (MAF) applied in black.

(b) The lithology log, obtained from interpreting the GR-log.

(c) The lithology log, obtained from DINOLoket. Green indicates clay, bright yellow, fine to medium grained sand, orange coarse sand and blue shell bearing sand.

Figure B.1: The data and lithological interpretation for B30G0935.

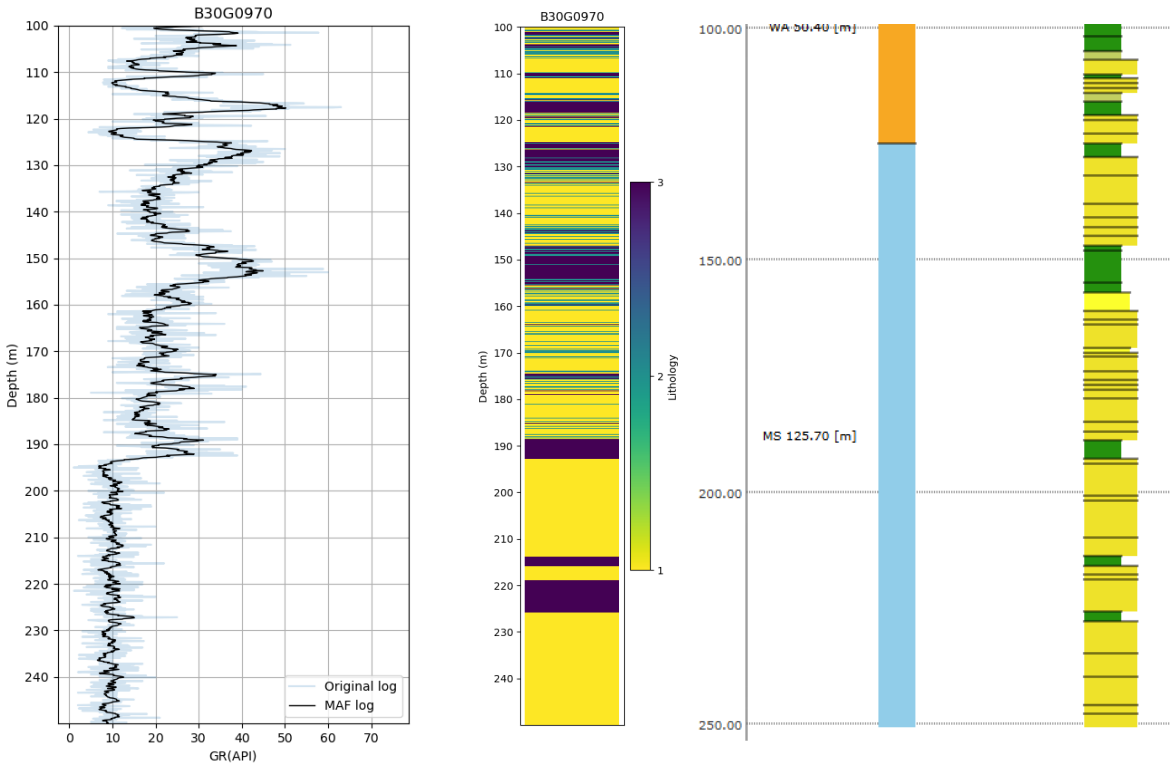

(a) The original GR-log in blue and the GR-log with a Moving Average Filter (MAF) applied in black.

(b) The lithology log, obtained from interpreting the GR-log.

(c) The lithology log, obtained from DINOLoket. Green indicates clay, bright yellow, fine to medium grained sand, orange coarse sand and blue shell bearing sand.

Figure B.2: The data and lithological interpretation for B30G0970.

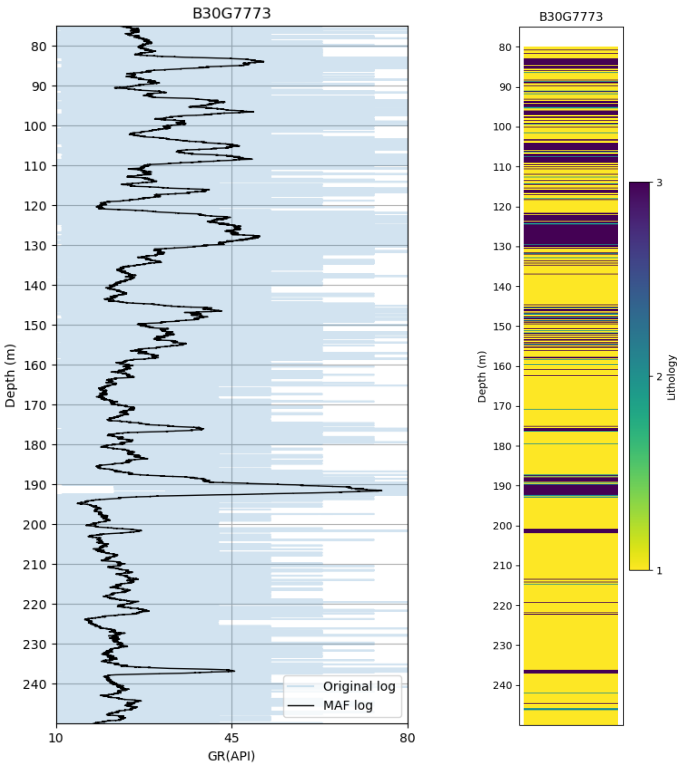

(a) The original GR-log in blue and the GR-log with a Moving Average Filter (MAF) applied in black.

(b) The lithology log, obtained from interpreting the GR-log.

Figure B.3: The data and lithological interpretation for B30G7773.

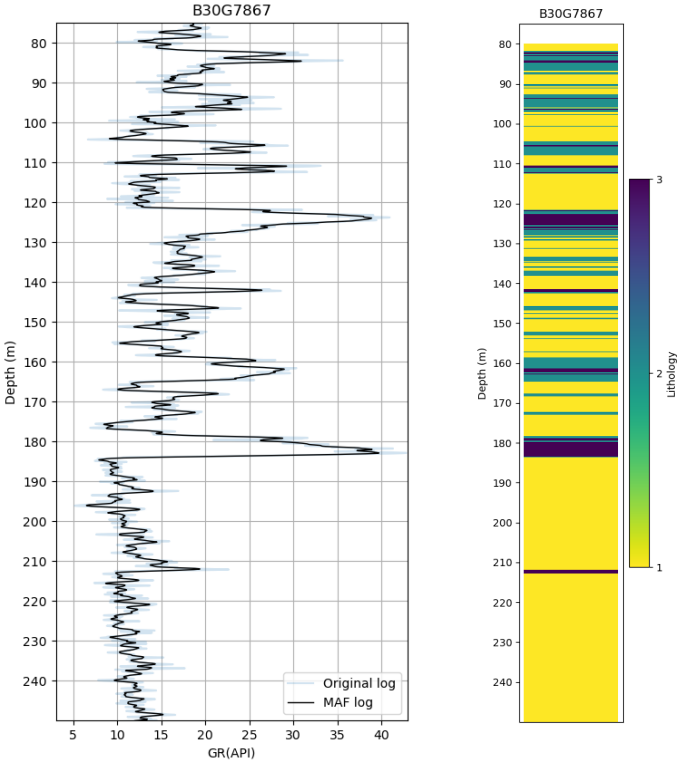

(a) The original GR-log in blue and the GR-log with a Moving Average Filter (MAF) applied in black.

(b) The lithology log, obtained from interpreting the GR-log.

Figure B.4: The data and lithological interpretation for B30G7867.

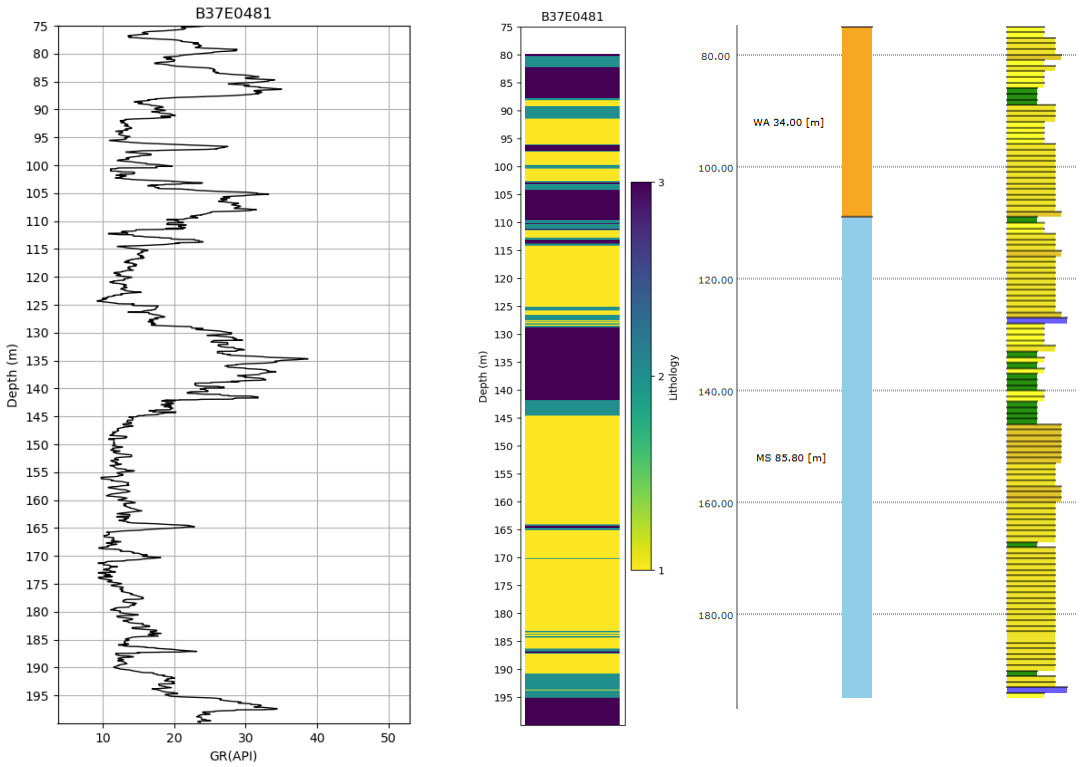

(a) The original GR-log in blue and the GR-log with a Moving Average Filter (MAF) applied in black.

(b) The lithology log, obtained from interpreting the GR-log.

(c) The lithology log, obtained from DINOLoket. Green indicates clay, bright yellow, fine to medium grained sand, orange coarse sand and blue shell bearing sand.

Figure B.5: The data and lithological interpretation for B37E0481.

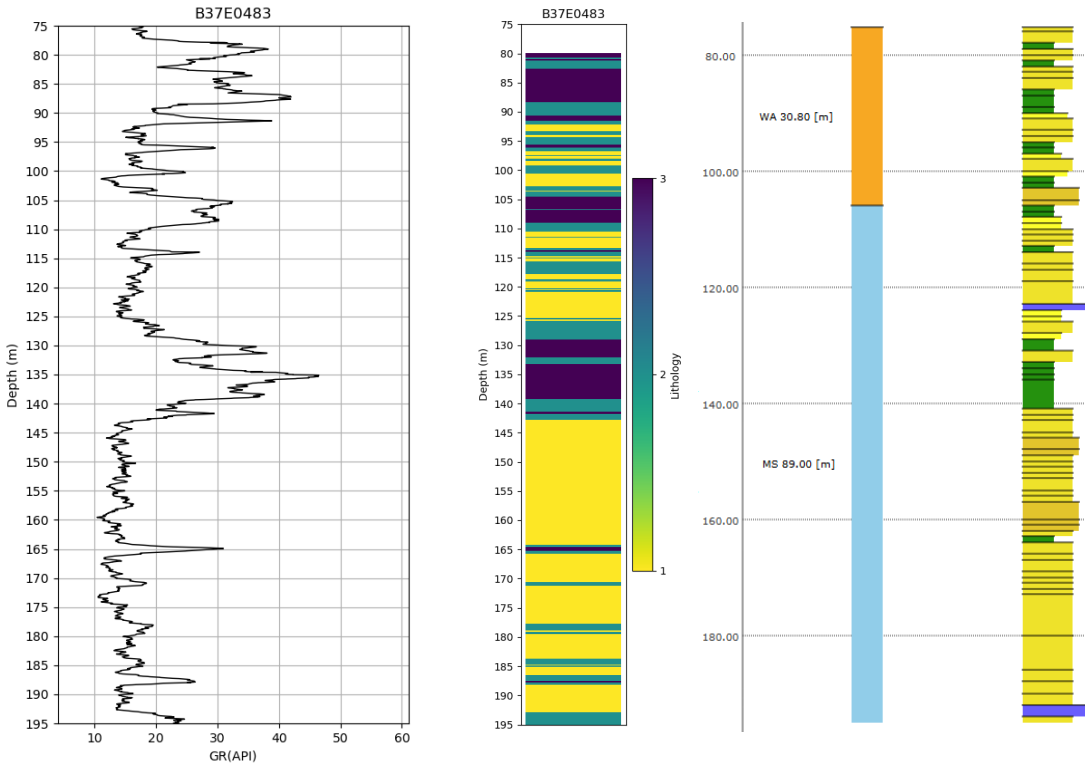

(a) The original GR-log in blue and the GR-log with a Moving Average Filter (MAF) applied in black.

(b) The lithology log, obtained from interpreting the GR-log.

(c) The lithology log, obtained from DINOLoket. Green indicates clay, bright yellow, fine to medium grained sand, orange coarse sand and blue shell bearing sand.

Figure B.6: The data and lithological interpretation for B37E0483.

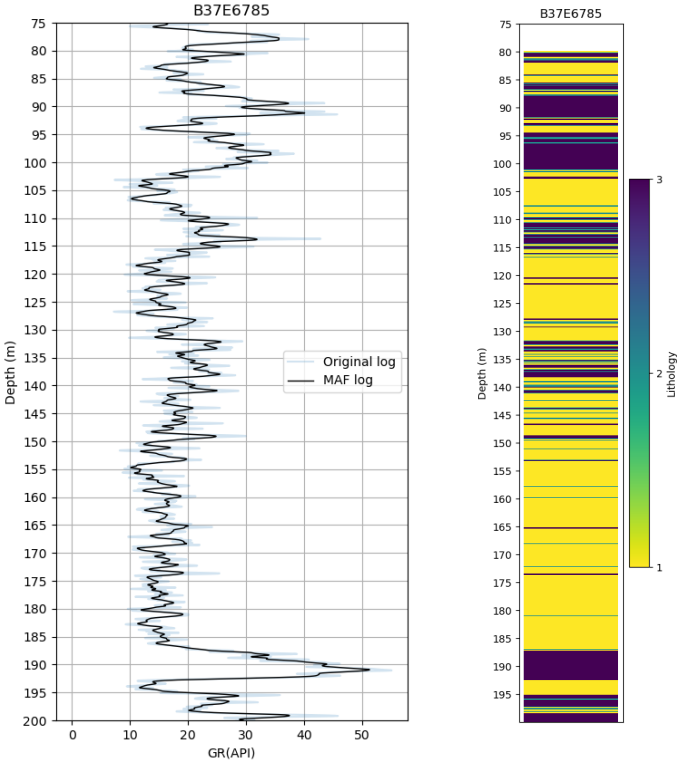

(a) The original GR-log in blue and the GR-log with a Moving Average Filter (MAF) applied in black.

(b) The lithology log, obtained from interpreting the GR-log.

Figure B.7: The data and lithological interpretation for B37E6785.

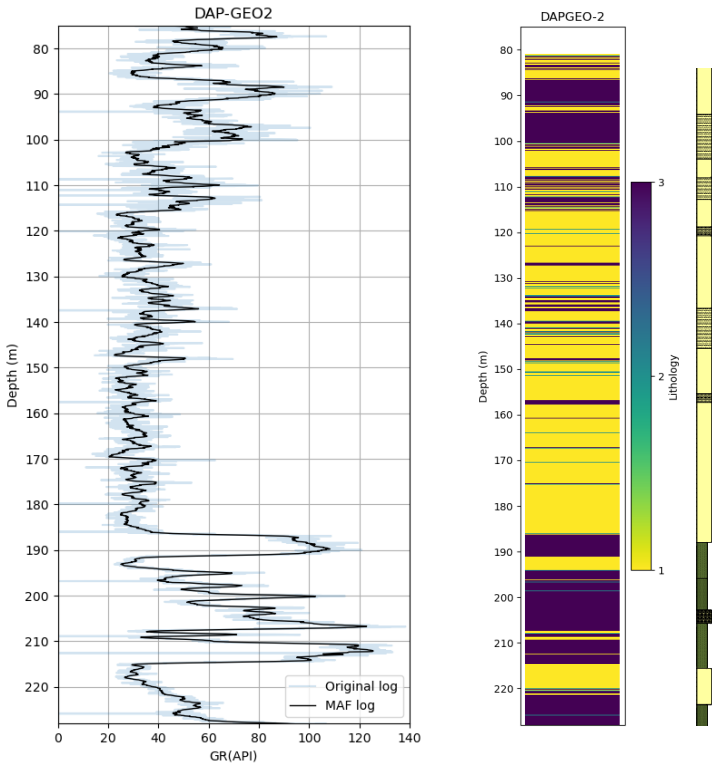

(a) The original GR-log in blue and the GR-log with a Moving Average Filter (MAF) applied in black.

(b) The lithology log, obtained from interpreting the GR-log.

(c) .

Figure B.8: The data and lithological interpretation for DAPGEO-2.

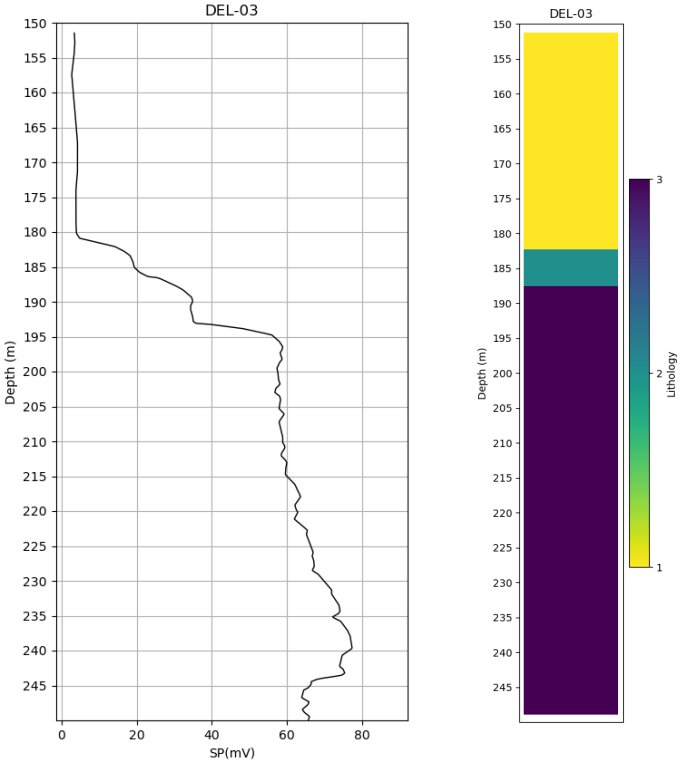

(a) The original GR-log in blue and the GR-log with a Moving Average Filter (MAF) applied in black.

(b) The lithology log, obtained from interpreting the GR-log.

Figure B.9: The data and lithological interpretation for DEL-03.

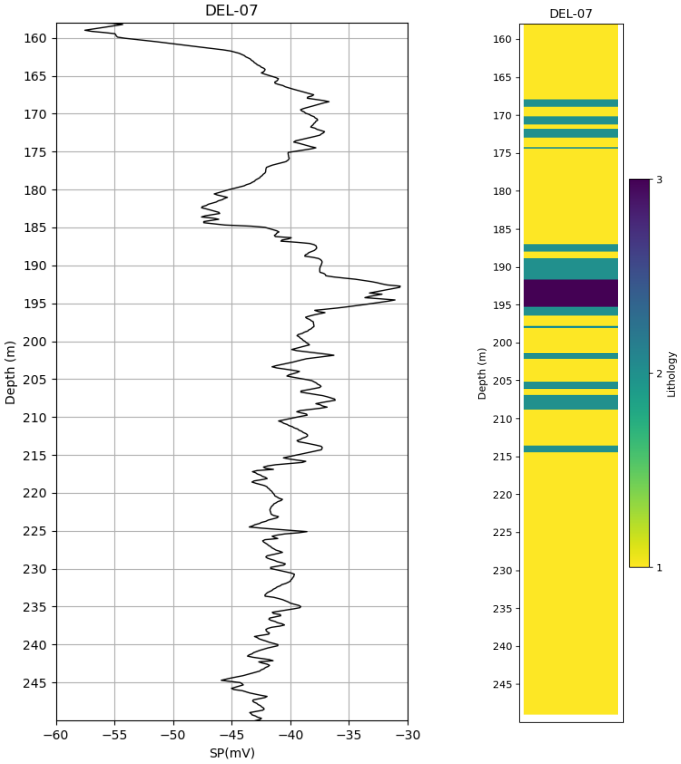

(a) The original GR-log in blue and the GR-log with a Moving Average Filter (MAF) applied in black.

(b) The lithology log, obtained from interpreting the GR-log.

Figure B.10: The data and lithological interpretation for DEL-07.

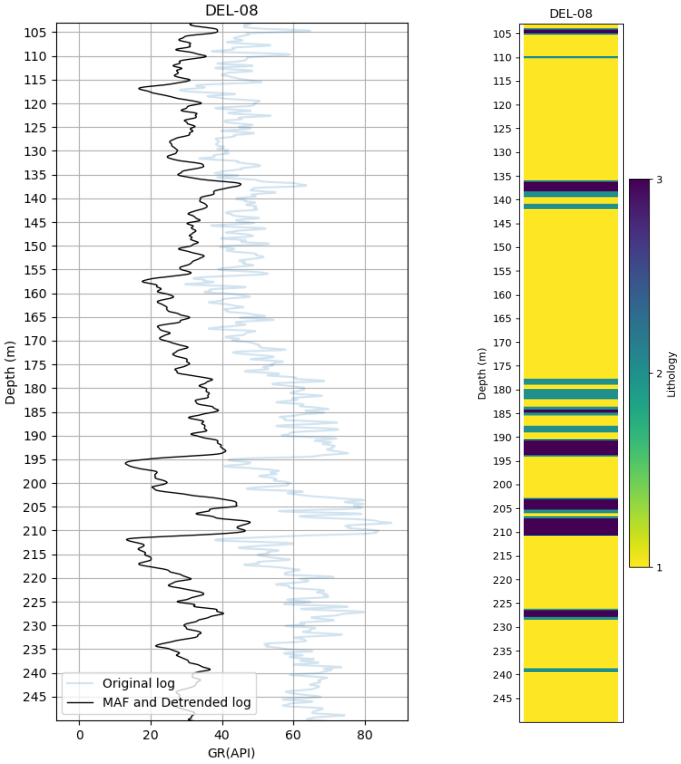

(a) The original GR-log in blue and the GR-log with a Moving Average Filter (MAF) applied in black.

(b) The lithology log, obtained from interpreting the GR-log.

Figure B.11: The data and lithological interpretation for DEL-08.

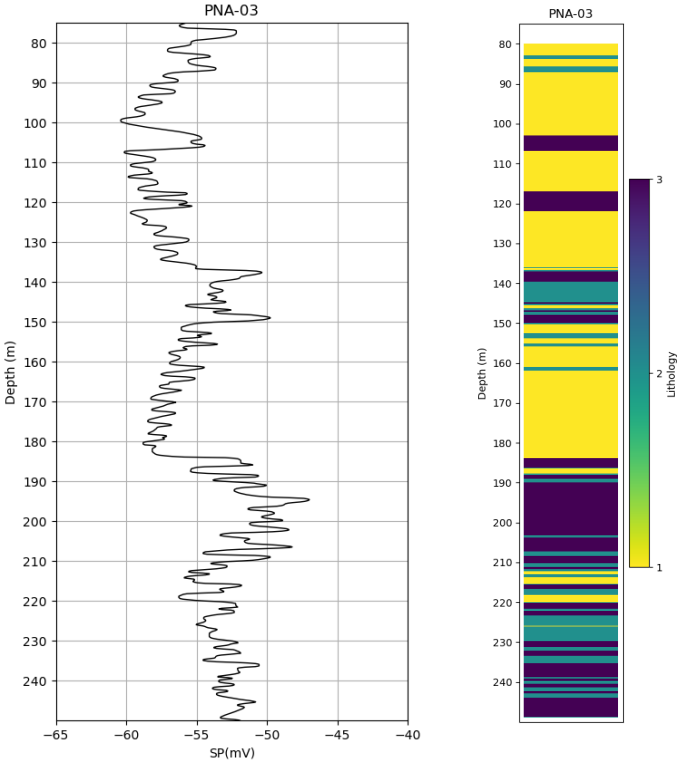

(a) The original GR-log in blue and the GR-log with a Moving Average Filter (MAF) applied in black.

(b) The lithology log, obtained from interpreting the GR-log.

Figure B.12: The data and lithological interpretation for PNA-03.

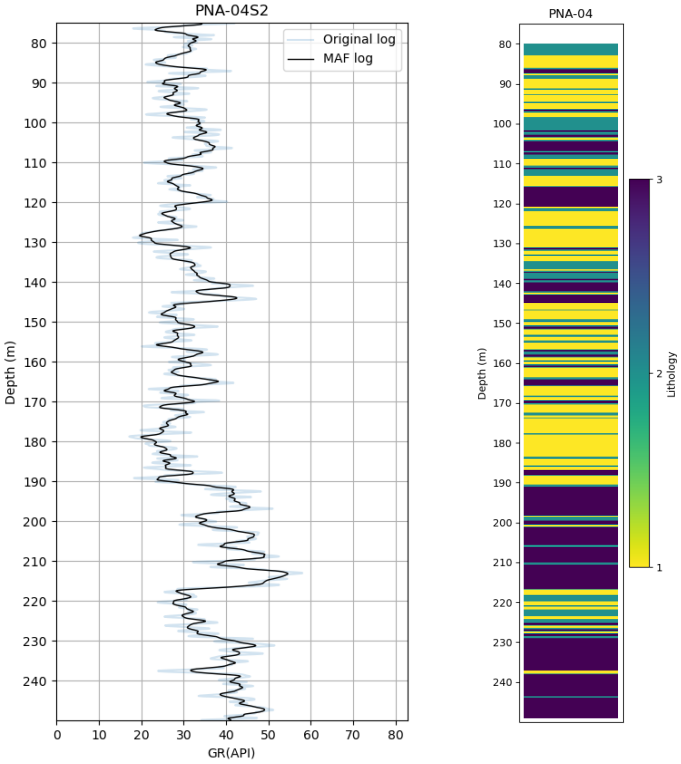

(a) The original GR-log in blue and the GR-log with a Moving Average Filter (MAF) applied in black.

(b) The lithology log, obtained from interpreting the GR-log.

Figure B.13: The data and lithological interpretation for PNA-04.

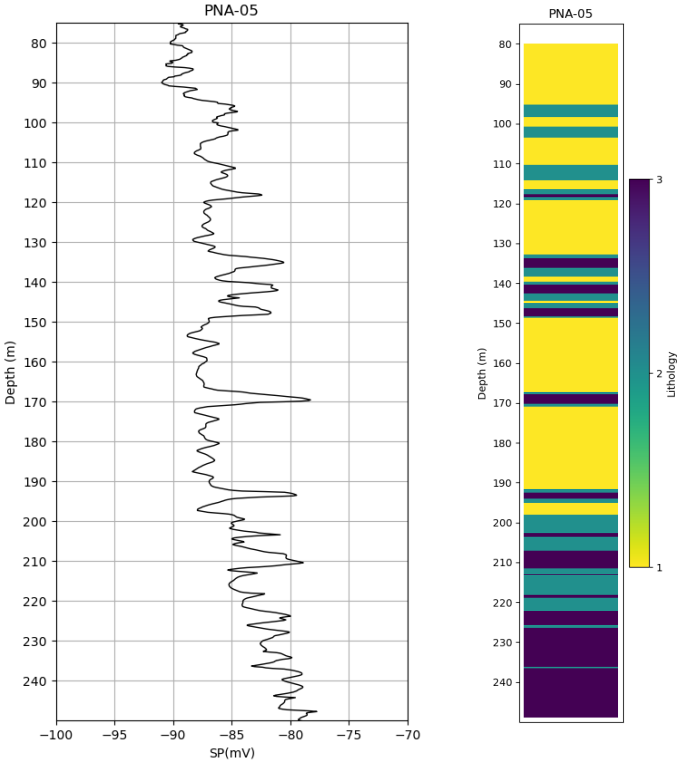

(a) The original GR-log in blue and the GR-log with a Moving Average Filter (MAF) applied in black.

(b) The lithology log, obtained from interpreting the GR-log.

Figure B.14: The data and lithological interpretation for PNA-05.

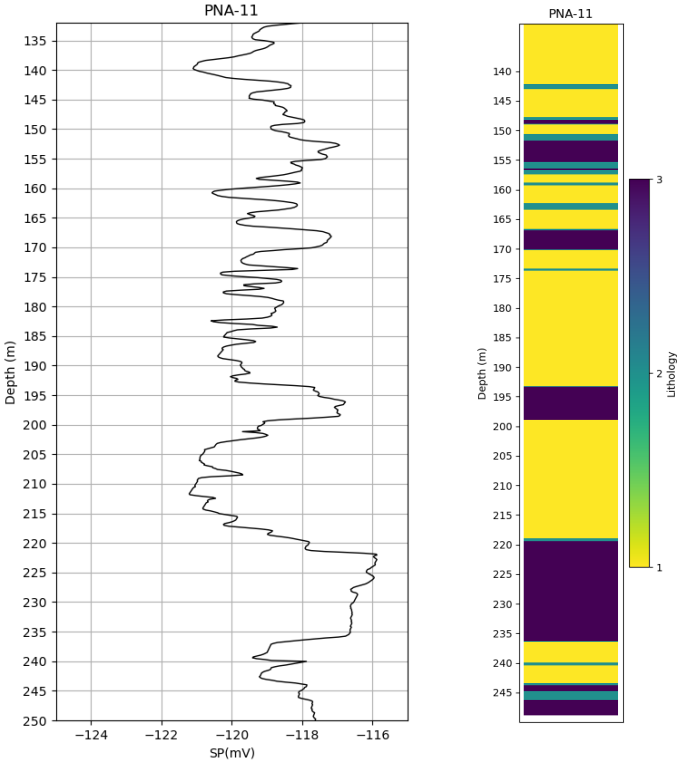

(a) The original GR-log in blue and the GR-log with a Moving Average Filter (MAF) applied in black.

(b) The lithology log, obtained from interpreting the GR-log.

Figure B.15: The data and lithological interpretation for PNA-11.

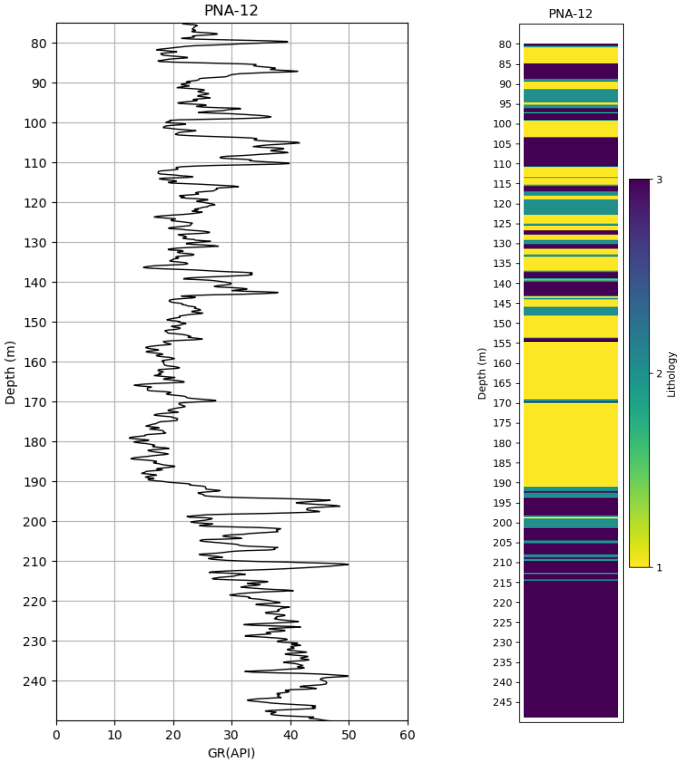

(a) The original GR-log in blue and the GR-log with a Moving Average Filter (MAF) applied in black.

(b) The lithology log, obtained from interpreting the GR-log.

Figure B.16: The data and lithological interpretation for PNA-12.

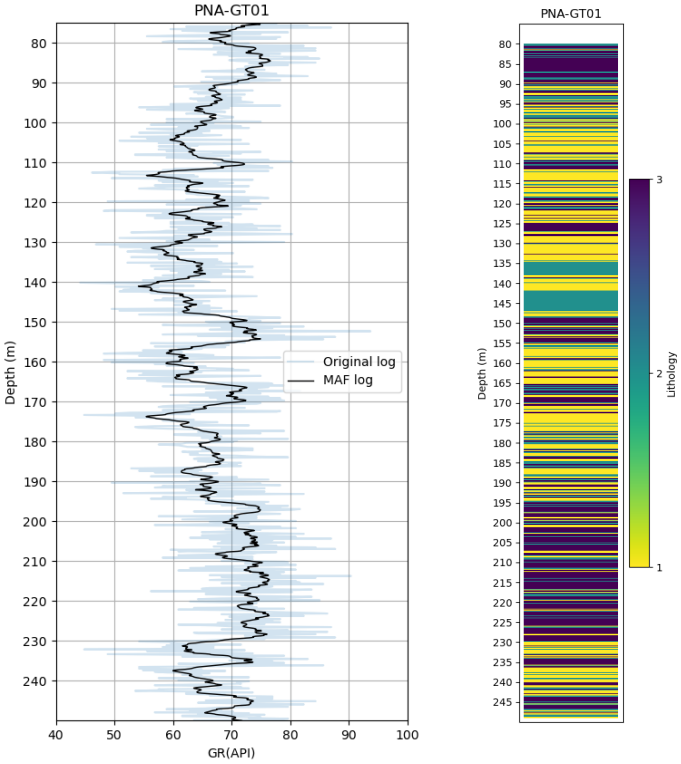

(a) The original GR-log in blue and the GR-log with a Moving Average Filter (MAF) applied in black.

(b) The lithology log, obtained from interpreting the GR-log.

Figure B.17: The data and lithological interpretation for PNA-GT01.

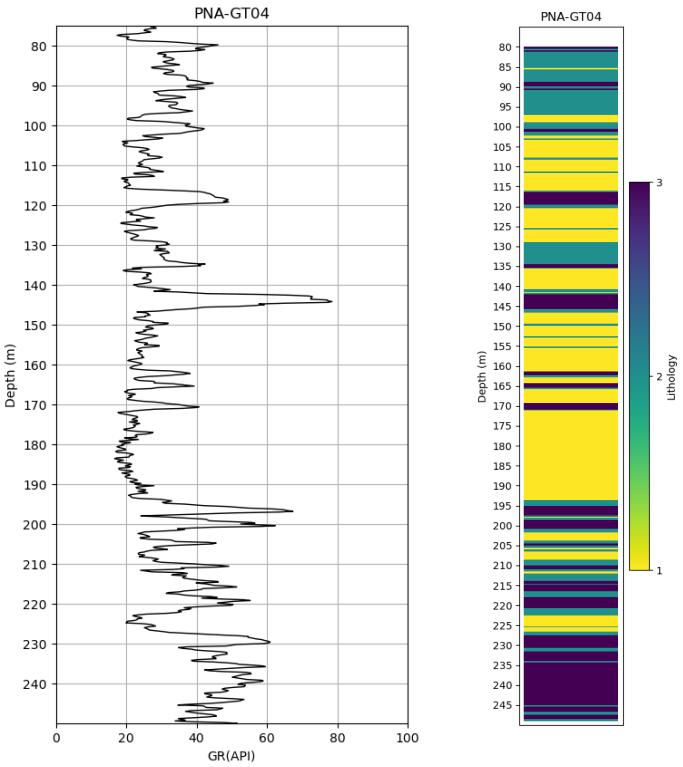

(a) The original GR-log in blue and the GR-log with a Moving Average Filter (MAF) applied in black.

(b) The lithology log, obtained from interpreting the GR-log.

Figure B.18: The data and lithological interpretation for PNA-GT04.

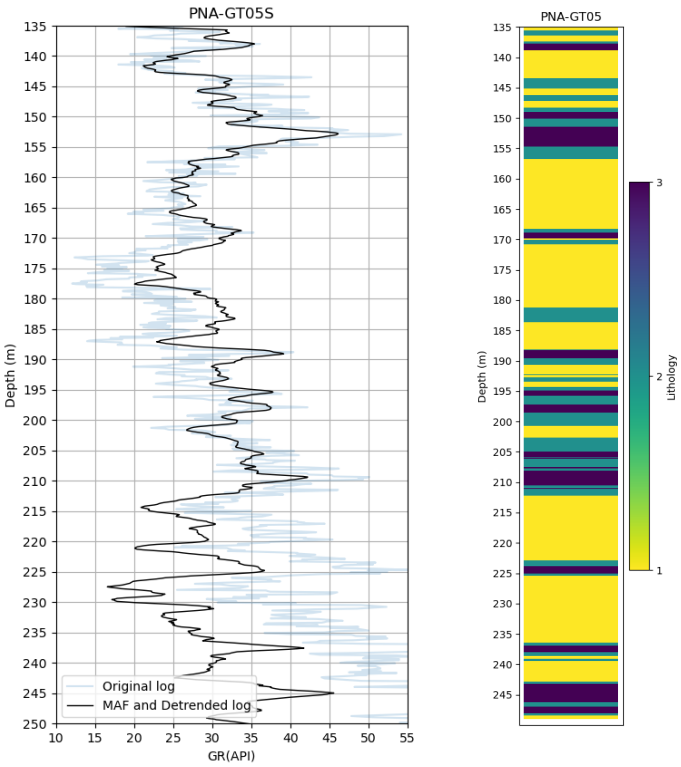

(a) The original GR-log in blue and the GR-log with a Moving Average Filter (MAF) applied in black.

(b) The lithology log, obtained from interpreting the GR-log.

Figure B.19: The data and lithological interpretation for PNA-GT05.

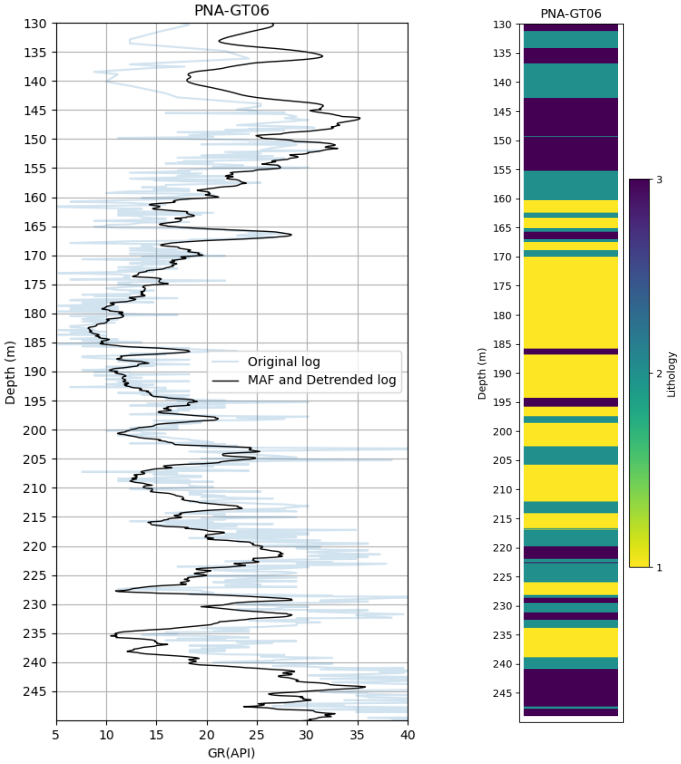

(a) The original GR-log in blue and the GR-log with a Moving Average Filter (MAF) applied in black.

(b) The lithology log, obtained from interpreting the GR-log.

Figure B.20: The data and lithological interpretation for PNA-GT06.

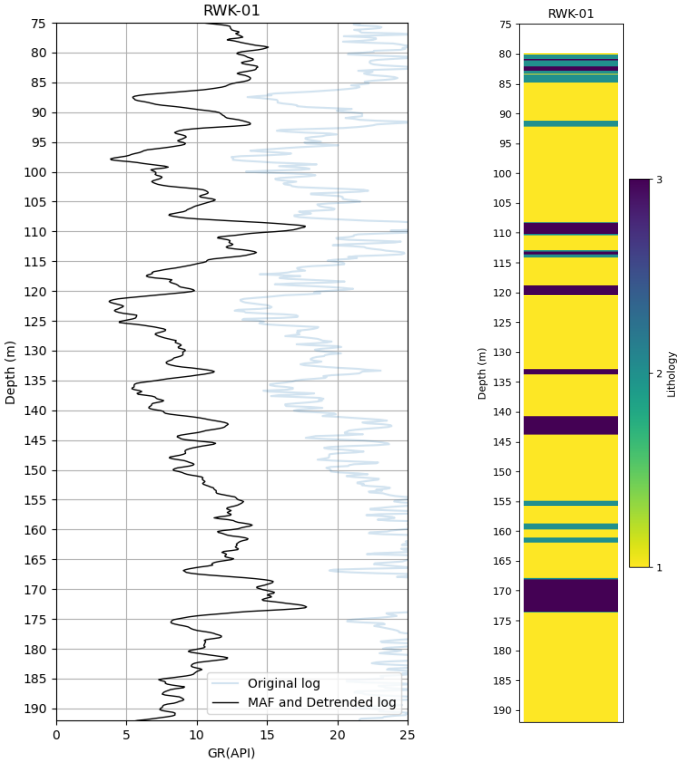

(a) The original GR-log in blue and the GR-log with a Moving Average Filter (MAF) applied in black.

(b) The lithology log, obtained from interpreting the GR-log.

Figure B.21: The data and lithological interpretation for RWK-01.

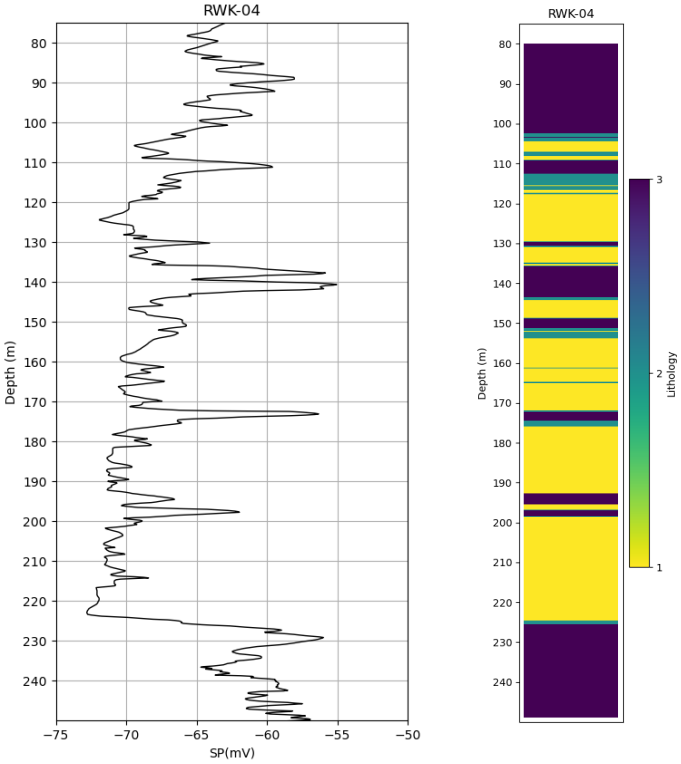

(a) The original GR-log in blue and the GR-log with a Moving Average Filter (MAF) applied in black.

(b) The lithology log, obtained from interpreting the GR-log.

Figure B.22: The data and lithological interpretation for RWK-04.

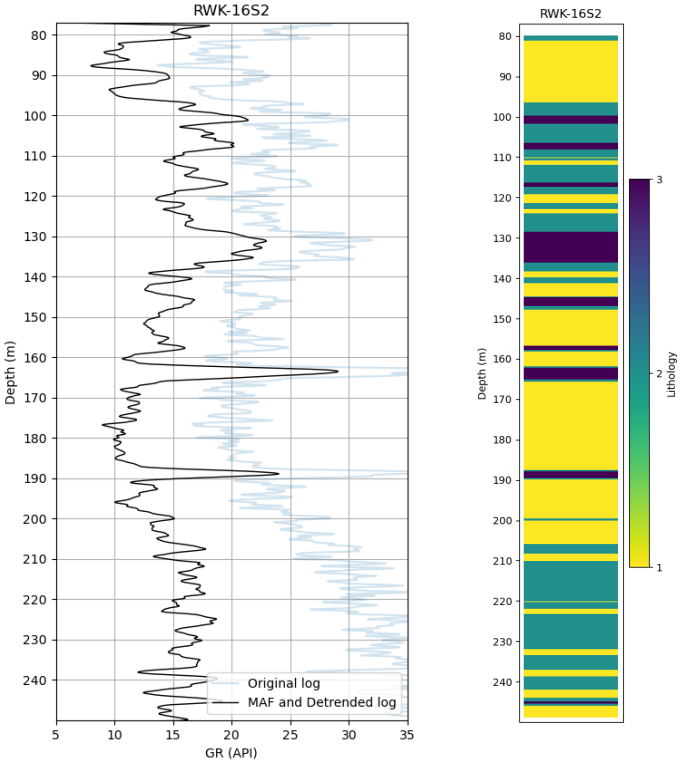

(a) The original GR-log in blue and the GR-log with a Moving Average Filter (MAF) applied in black.

(b) The lithology log, obtained from interpreting the GR-log.

Figure B.23: The data and lithological interpretation for RWK-16S2.

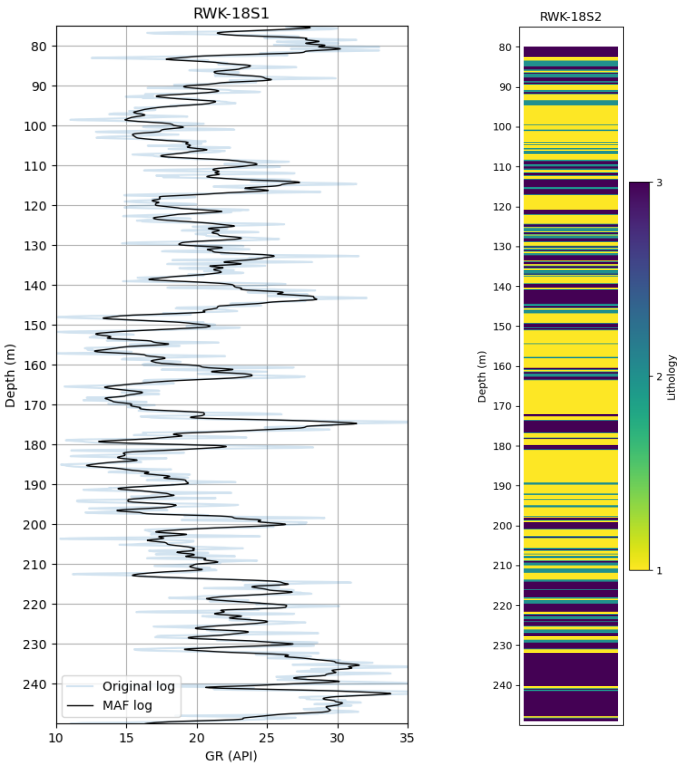

(a) The original GR-log in blue and the GR-log with a Moving Average Filter (MAF) applied in black.

(b) The lithology log, obtained from interpreting the GR-log.

Figure B.24: The data and lithological interpretation for RWK-18S2.

C

Variography

A brief introduction about the construction of semivariograms and the important equations of Deutsch and Journel, 1997 will be given here.

$$\gamma(\mathbf{h}) = \frac{1}{2N(\mathbf{h})} \sum_{i=1}^{N(\mathbf{h})} (x_i - y_i)^2 \tag{C.1}$$

$$\gamma(h) = \begin{cases} c \cdot (1.5 \cdot \frac{h}{a} - 0.5(\frac{h}{a})^3) & : \ h < a \\ c & : \ h \geq a \end{cases} \tag{C.2}$$

PNA

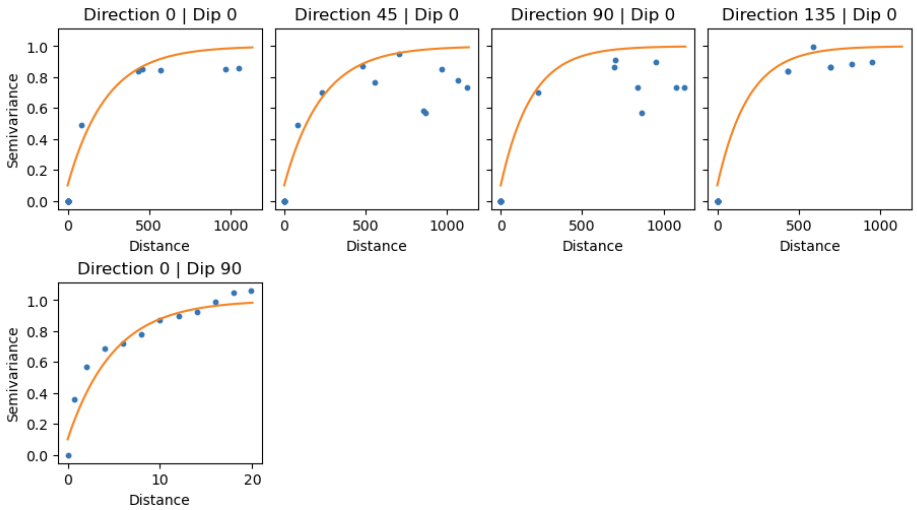

Figure C.1: The experimental semivarogram and the semivariogram model for lithology 1 of the PNA model.

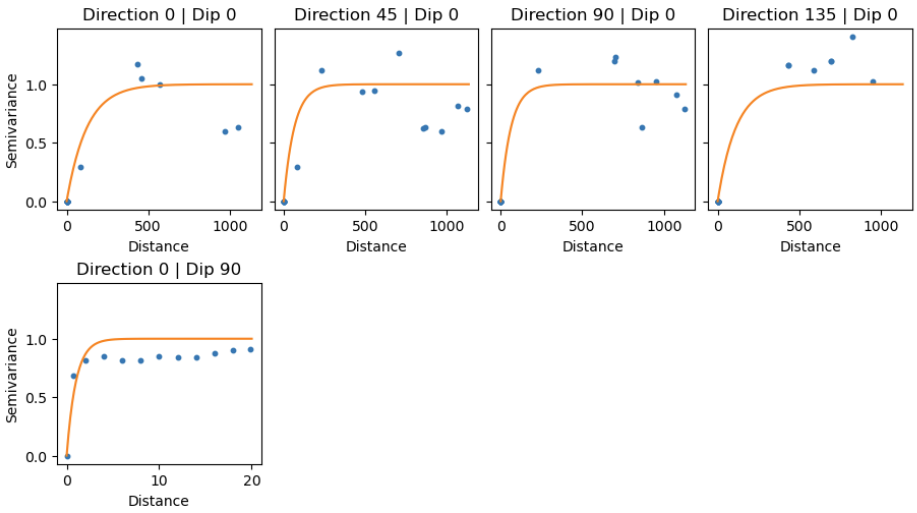

Figure C.2: The experimental semivarogram and the semivariogram model for lithology 2 of the PNA model.

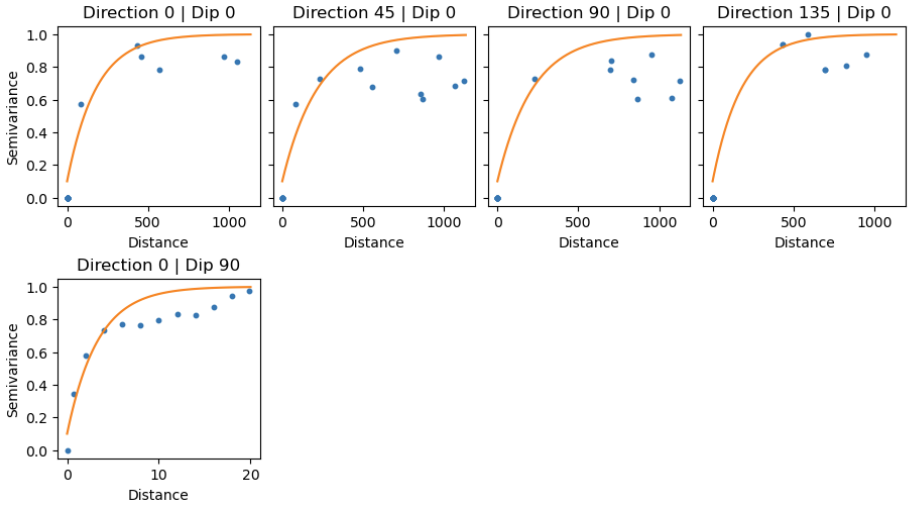

Figure C.3: The experimental semivarogram and the semivariogram model for lithology 3 of the PNA model.

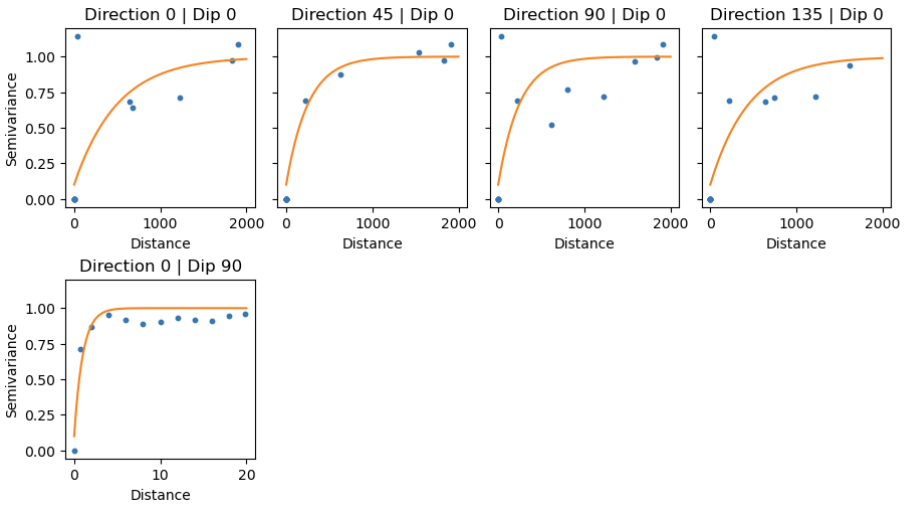

Figure C.5: The experimental semivarogram and the semivariogram model for lithology 2 of the RWK model.

RWK

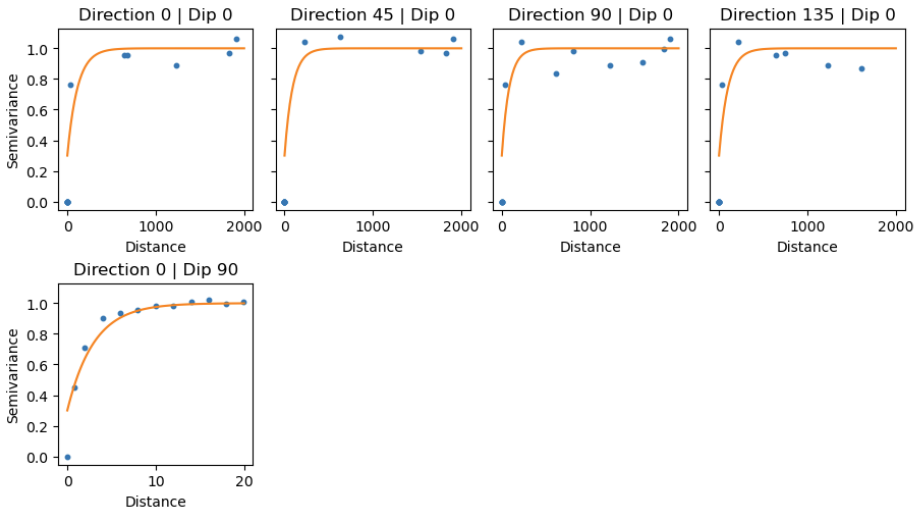

Figure C.4: The experimental semivarogram and the semivariogram model for lithology 1 of the RWK model.

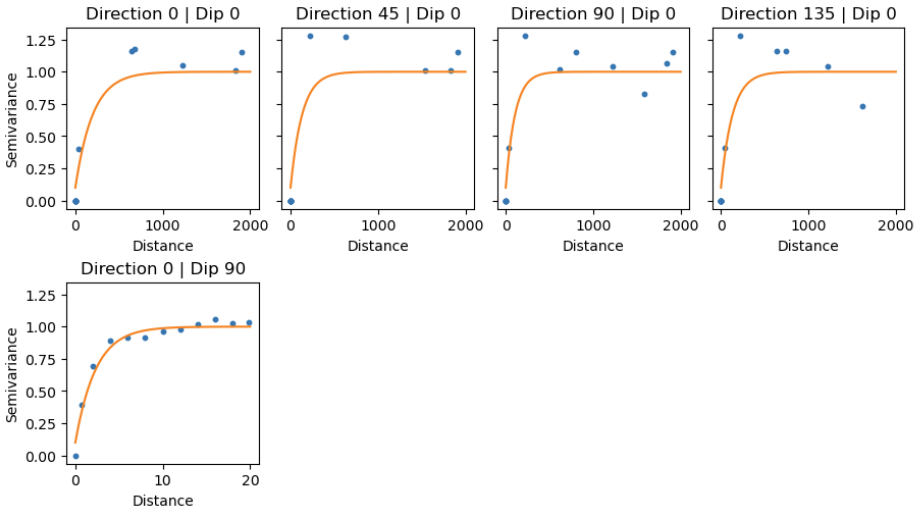

Figure C.6: The experimental semivarogram and the semivariogram model for lithology 3 of the RWK model.

D

Derivation of operator form of mass and energy conservation equations

Based on the works of Chen, D. Voskov, and Daniilidis (2025):

$$\frac{\partial}{\partial t}(\phi \sum_{p=1}^{n_p} x_{cp}\rho_p s_p) + div \sum_{p=1}^{n_p} x_{cp}\rho_p s_p \vec{u}_p + \sum_{p=1}^{n_p} x_{cp}\rho_p \tilde{q}_p = 0, c = 1, ..., n_c \tag{D.1}$$

Darcy's law for water velocity:

$$\vec{u}_p = -\mathbf{K}\frac{k_{rp}}{\mu_p}(\nabla p_p + \gamma_p \nabla D) \tag{D.2}$$

Rock compressibility for porosity changes due to pressure changes, Chen 2025

$$\phi = \phi_0(1 - c_r(p - p_{ref}) \tag{D.3}$$

In discretized form (with BE approximation):

$$V[(\phi \sum_{p=1}^{n_p} \rho_p s_p U_p)^{n+1} - (\phi \sum_{p=1}^{n_p} \rho_p s_p U_p)^n] - \Delta t \sum_l (\sum_{p=1}^{n_p} x_{cp}^l \rho_p^l \Gamma_p^l \psi_p^l) + \Delta t \sum_{p=1}^{n_p} x_{cp}\rho_p q_p = 0, c = 1, ..., n_c \tag{D.4}$$

Equation D.4 in residual form is presented below. This, together with the residual form of the energy conservation (ref to eq), are solved.

$$r(\xi, \omega, \mathbf{u}) = V(\xi)\phi_0(\xi)(\alpha(\omega)\alpha(\omega_n)) - \sum_l \beta^l(\omega_n)\Delta t \Gamma^l (p^b - p^a)^l + \theta(\xi, \omega, \mathbf{u}) = 0 \tag{D.5}$$

Energy conservation Chen2025

$$\frac{\partial}{\partial t}(\phi \sum_{p=1}^{n_p} \rho_p s_p U_p + (1 - \phi)U_r) + div \sum_{p=1}^{n_p} h_p \rho_p \vec{u}_p + div(\kappa \nabla T) + \sum_{p=1}^{n_p} h_p \rho_p \tilde{q}_p = 0 \tag{D.6}$$

With the internal energy of the fluid, given by:

$$U_p = \rho_p h_p - p \tag{D.7}$$

and a linear estimation of the internal rock energy, based on the heat capacity, Cr.

$$U_r = C_r(T - T_{ref}) \tag{D.8}$$

In discretized form (with BE approximation):

$$V[(\phi\sum_{p=1}^{n_p}\rho_p s_p U_p+(1\phi)U_r)^{n+1}(\phi\sum_{p=1}^{n_p}\rho_p s_p U_p+(1\phi)U_r)^{n}]-\Delta t\sum_{l}(\sum_{p=1}^{n_p^l}h_p^l\rho_p^l\Gamma_p^l\Delta\psi^l+\Gamma_c^l\Delta T^l)+\Delta t\sum_{p=1}^{n_p}h_p\rho_p\tilde{q}_p=0 \tag{D.9}$$

$$\Gamma_c^l = \Gamma_g^l[\phi\kappa_p + (1-\phi\kappa_r)] \tag{D.10}$$

Mass conservation in residual form:

$$r(\xi,\omega,\mathbf{u}) = V(\xi)\phi_0(\xi)(\alpha(\omega)-\alpha(\omega_n)) - \sum_l \beta^l(\omega)\Delta t\Gamma^l(p^b-p^a)^l + \theta(\xi,\omega,\mathbf{u}) = 0 \tag{D.11}$$

With α, β and θ for the mass conservation defined as:

$$\alpha(\omega) = (1+c_r(p-p_{ref}))\sum_{p=1}^{n} x_{cp}\rho_p s_p \tag{D.12}$$

$$\beta(\omega) = \sum_{p=1}^{n_p} x_{cp}\frac{k_{rp}}{\mu_p}\rho_p \tag{D.13}$$

$$\theta(\xi,\omega,\mathbf{u}) = \Delta t\sum_{p=1}^{n_p} x_{cp}\rho_p q_p(\xi,\omega,\mathbf{u}) \tag{D.14}$$

The energy conservation equation in residual form:

$$r_e(\xi,\omega,\mathbf{u}) = V(\xi)\big(\alpha_e(\omega)-\alpha_e(\omega_n)\big) - \sum_l \beta_e^l(\omega)\Delta t\,\Gamma^l\big(p^b-p^a\big)^l - \sum_l \gamma_e^l(\omega)\Delta t\,\Gamma^l\big(T^b-T^a\big)^l + \theta_e(\xi,\omega,\mathbf{u}) = 0 \tag{D.15}$$

The operators for the energy conservation equation:

$$\alpha_e(\omega) = \Phi\left(\sum_{p=1}^{n_p}\rho_p s_p U_p - U_r\right), \tag{D.16}$$

$$\beta_e(\omega) = \sum_{p=1}^{n_p} h_p\frac{\rho_p^l k_{rp}^l}{\mu_p}, \tag{D.17}$$

$$\gamma_e(\omega) = \Phi\left(\sum_{p=1}^{n_p} s_p\lambda_p - \kappa_r\right) + \kappa_r. \tag{D.18}$$

Newton-Raphson method is used to solve non-linear equations.

$$J(\omega^k)(\omega^k - \omega^{k+1}) - r(\omega^k) = 0 \tag{D.19}$$

E

Thermal plume density maps

E.1. Thermal plume maps for which T > 25 degrees Celsius

E.1.1. Stochastic geomodel plumes

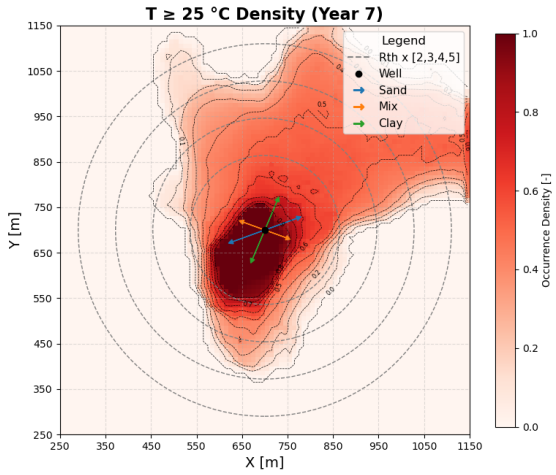

(a) The thermal density plot for PNA1, with an injection volume of 600,000 cubic meters per year in the seventh year.

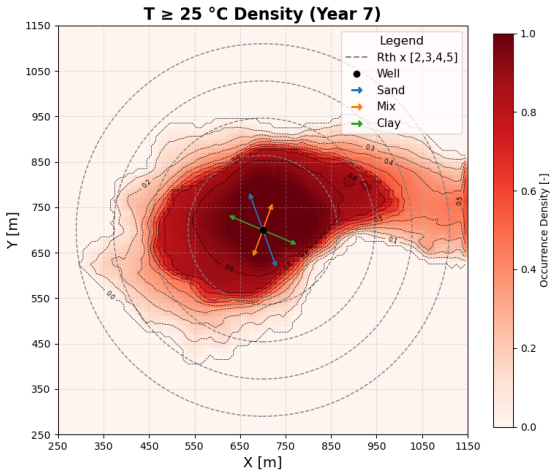

(b) The thermal density plot for PNA2, with an injection volume of 600,000 cubic meters per year in the seventh year.

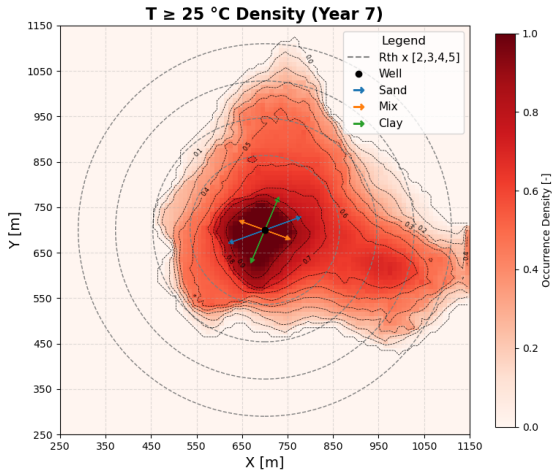

(c) The thermal density plot for PNA3, with an injection volume of 600,000 cubic meters per year in the seventh year.

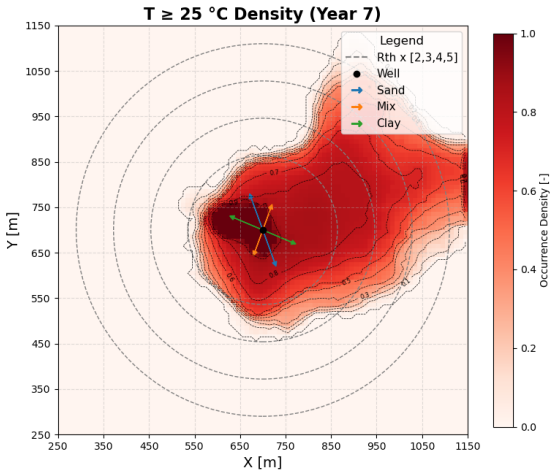

(d) The thermal density plot for PNA4, with an injection volume of 600,000 cubic meters per year in the seventh year.

Figure E.1: The density of the thermal plume spread of the PNA models.

E.1.2. RWK plumes

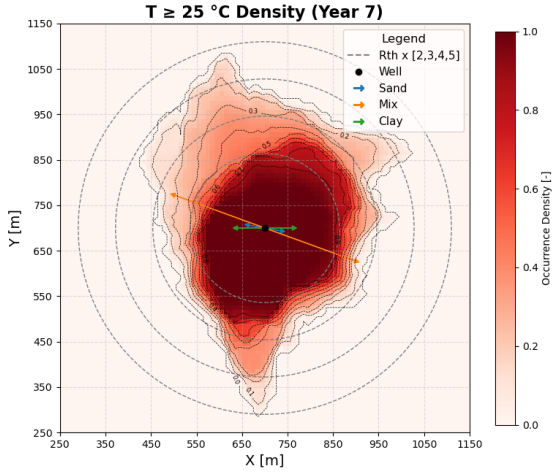

(a) The thermal density plot for RWK1, with an injection volume of 600,000 cubic meters per year in the seventh year.

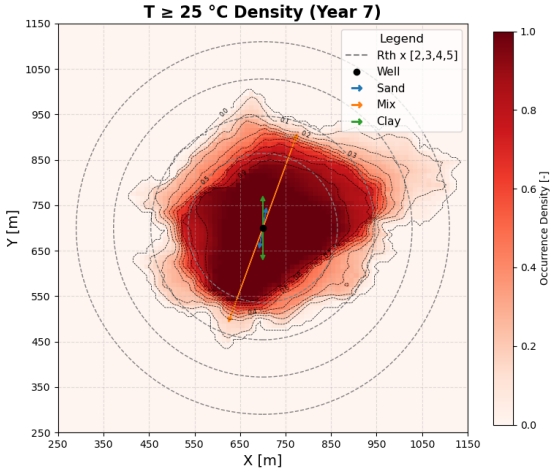

(b) The thermal density plot for RWK2, with an injection volume of 600,000 cubic meters per year in the seventh year.

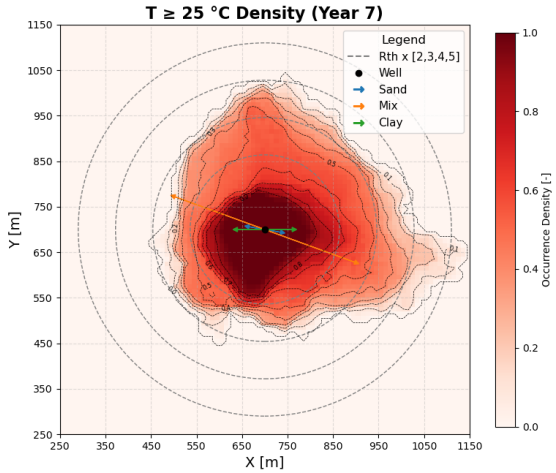

(c) The thermal density plot for RWK3, with an injection volume of 600,000 cubic meters per year in the seventh year.

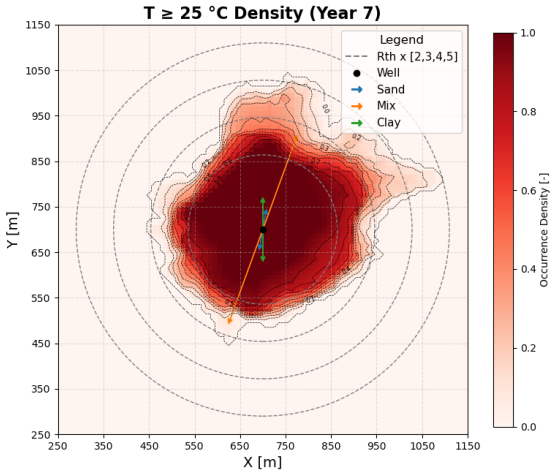

(d) The thermal density plot for RWK4, with an injection volume of 600,000 cubic meters per year in the seventh year.

Figure E.2: The density of the thermal plume spread of the RWK models.

E.1.3. PBS plumes

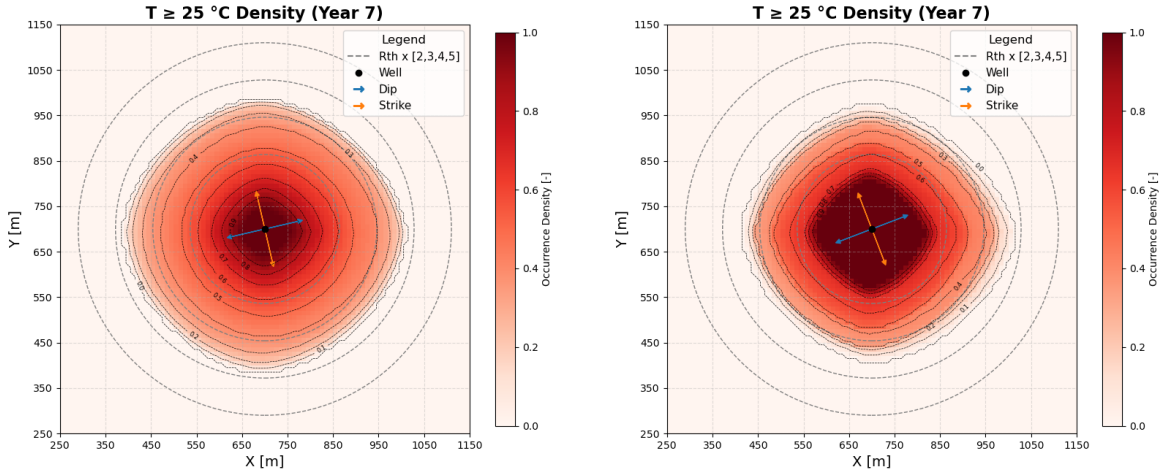

(a) The thermal density plot for PBS1, with an injection volume of 600,000 cubic meters per year in the seventh year.

(b) The thermal density plot for PBS2, with an injection volume of 600,000 cubic meters per year in the seventh year.

Figure E.3: The density of the thermal plume spread of the PBS1 and PBS2 models.

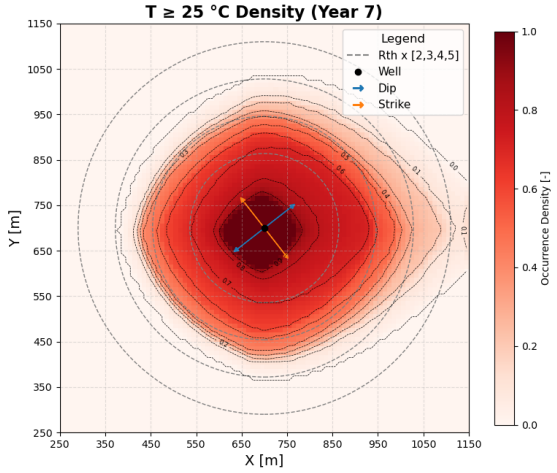

Figure E.4: The thermal density plot for PBS3, with an injection volume of 600,000 cubic meters per year in the seventh year.